

**AD A108505**

**AFOSR-TR- 81 - 0786**

**V6**

SEMI-ANNUAL TECHNICAL REPORT  
1 November 1980 - 30 April 1981

ARPA Order No.: 3291.40  
Program Code: 1A10  
Name of Contractor: California Institute of Technology  
Effective Date of Contract: 1 November 1980  
Contract Expiration Date: 31 October 1981  
Amount of Contract: \$169,942  
Contract Number: F49620-81-C-0008  
Principal Investigators: David G. Harkrider  
(213) 356-6910  
Donald V. Helmberger  
(213) 356-6911  
Program Manager and  
Telephone Number William J. Best  
(202) 767-5011  
Short Title of Work: Body and Surface Wave Modeling  
of Observed Seismic Events

The views and conclusions contained in this document are those of the authors and should not be interpreted as necessarily representing the official policies, either expressed or implied, of the Defense Advanced Research Projects Agency or the U.S. Government.

Sponsored by  
Advanced Research Projects Agency (DOD)  
ARPA Order No. 3291.40  
Monitored by AFOSR Under Contract No. F49620-81-C-0008

Seismological Laboratory  
Division of Geological and Planetary Sciences  
California Institute of Technology  
Pasadena, California 91125

Approved for public release;  
distribution unlimited.

**DTIC FILE COPY**



## UNCLASSIFIED

SECURITY CLASSIFICATION OF THIS PAGE (When Data Entered)

REPORT DOCUMENTATION PAGE		READ INSTRUCTIONS BEFORE COMPLETING FORM
1. REPORT NUMBER <b>AFOSR-TR- 81 -0786</b>	2. GOVT ACCESSION NO. <b>AD-A108505</b>	3. RECIPIENT'S CATALOG NUMBER
4. TITLE (and Subtitle) Body and Surface Wave Modeling Of Observed Seismic Events	5. TYPE OF REPORT & PERIOD COVERED 1 Nov. 1980 - 30 Apr. 1981 Semi-Annual Technical Report	
7. AUTHOR(s) David G. Harkrider Donald V. Helmberger	6. PERFORMING ORG. REPORT NUMBER F49620-81-C-0008	
9. PERFORMING ORGANIZATION NAME AND ADDRESS California Institute of Technology Seismological Laboratory, 252-21 Pasadena, California 91125	10. PROGRAM ELEMENT, PROJECT, TASK AREA & WORK UNIT NUMBERS ARPA Order No. 3291.40 <b>61102F, 2309/A1</b>	
11. CONTROLLING OFFICE NAME AND ADDRESS AFOSR/NP Building 410 Bolling AFB, D.C. 20332	12. REPORT DATE 1 Nov. 1980 - 30 Apr. 1981	
14. MONITORING AGENCY NAME & ADDRESS (if different from Controlling Office)	13. NUMBER OF PAGES 132 <i>(136)</i>	
15. SECURITY CLASS. (of this report) <b>91N/C CLASSIFIED</b>		
15a. DECLASSIFICATION/DOWNGRADING SCHEDULE		
16. DISTRIBUTION STATEMENT (of this Report) Approved for public release; distribution unlimited		
17. DISTRIBUTION STATEMENT (of the abstract entered in Block 20, if different from Report)		
18. SUPPLEMENTARY NOTES		
19. KEY WORDS (Continue on reverse side if necessary and identify by block number) Rayleigh wave excitation, higher mode Lg, Borrego Mountain earthquake, UC diagram technique, strong motion synthetics, laterally inhomogeneous source regions		
20. ABSTRACT (Continue on reverse side if necessary and identify by block number) <i>This research performed under the contract during the period 1 November 1980 through 30 April 1981 can be divided into three main topics, coupling of surface waves generated in laterally inhomogeneous source regions to teleseismic propagation paths, the use of long linear arrays to separate and interpret Lg waves in terms of higher mode surface waves, and the use of short and long period teleseismic body waves in determining the character of seismic sources.</i> (Continued)		

DD FORM 1 JAN 73 1473

UNCLASSIFIED

SECURITY CLASSIFICATION OF THIS PAGE (When Data Entered)

320050

30

(cont)

In Section II, a comparison is given between three approximate mixed-path Rayleigh wave techniques. Two of the techniques are commonly used and the third is a modification of a test of the representation theorem. All three give similar results for explosions in an NTS granitic source region coupled to a continental propagation model. The rigidity ratio of the source material to exterior crustal material is 0.612 and all three methods give amplitude ratios which are near this. For a source medium such as NTS Yucca Flat Tuff, all three techniques yield different amplitude ratios ranging from 0.264 to 1.17 with the rigidity ratio at 0.0932. Hopefully, when the correct answer is obtained using the finite element forcing functions, one of these inexpensive techniques will be validated. As of now, all we can say is that yield estimates from regional surface waves generated at Yucca Flat using these mixed path techniques may be in error by an order of magnitude.

In Section III, Lg data sets recorded in southern California and along the northwestern margin of the Sierra Nevada are analyzed in terms of higher mode Rayleigh waves using the UC diagram technique. It is found that for group velocities between 3.2 and 3.6 km/sec both regions can generally be interpreted in terms of higher mode surface waves. For group velocities smaller than 3.2 km/sec this interpretation is over-simplified in the case of southern California but is more appropriate for the Sierra block. The lack of coherence in the south is probably due to lateral heterogeneity effects.

In Section IV a short-period deconvolution analysis of the teleseismic P-waves generated from the Borrego Mountain earthquake of 1968 are used to model the strong motion SH recordings at El Centro. The teleseismic P-waves suggest a two source model, each of less than 2 second duration, the second occurring at 2.2 seconds after the first and both at a depth of 8 km.

Accession No.	
NTIS GRANT	
DTIC TAB	
Unclassified	
Classification	
By	
Distribution	
Availability Codes	
Dist	Avail and/or Special
A	

UNCLASSIFIED

## TABLE OF CONTENTS

	Page
I. Summary . . . . .	1
II. An application of the representation theorem to the evaluation of analytic techniques for calculating mixed-path Rayleigh waves . . . . .	3
III. Multimode analysis of Rayleigh-type Lg, II: Application to Southern California and the northwestern Sierra Nevada . . . . .	27
IV. P-wave complexity and fault asperities: The Borrego mountain, California, earthquake of 1968 . . . . .	72

AIR FORCE OFFICE OF SCIENTIFIC RESEARCH (AFSC)  
NOTICE OF TRANSMITTAL TO DTIC  
This technical report has been reviewed and is  
approved for public release IAN AFRL 100-12.  
Distribution is unlimited.  
**MATTHEW J. KERPER**  
Chief, Technical Information Division

## I. SUMMARY

The research performed under the contract during the period 1 November 1980 through 30 April 1981 can be divided into three main topics, coupling of surface waves generated in laterally inhomogeneous source regions to teleseismic propagation paths, the use of long linear arrays to separate and interpret Lg waves in terms of higher mode surface waves, and the use of short and long period teleseismic body waves in determining the character of seismic sources.

In Section II, a comparison is given between three approximate mixed-path Rayleigh wave techniques. Two of the techniques are commonly used and the third is a modification of a test of the representation theorem. All three give similar results for explosions in an NTS granitic source region coupled to a continental propagation model. The rigidity ratio of the source material to exterior crustal material is 0.612 and all three methods give amplitude ratios which are near this. For a source medium such as NTS Yucca Flat Tuff, all three techniques yield different amplitude ratios ranging from 0.264 to 1.17 with the rigidity ratio at 0.0932. Hopefully, when the correct answer is obtained using the finite element forcing functions, one of these inexpensive techniques will be validated. As of now, all we can say is that yield estimates from regional surface waves generated at Yucca Flat using these mixed path techniques may be in error by an order of magnitude.

In Section III, Lg data sets recorded in southern California

and along the northwestern margin of the Sierra Nevada are analyzed in terms of higher mode Rayleigh waves using the UC diagram technique. It is found that for group velocities between 3.2 and 3.6 km/sec both regions can generally be interpreted in terms of higher mode surface waves. For group velocities smaller than 3.2 km/sec this interpretation is over-simplified in the case of southern California but is more appropriate for the Sierra block. The lack of coherence in the south is probably due to lateral heterogeneity effects.

In Section IV a short-period deconvolution analysis of the teleseismic P-waves generated from the Borrego Mountain earthquake of 1968 are used to model the strong motion SH recordings at El Centro. The teleseismic P-waves suggest a two source model, each of less than 2 second duration, the second occurring at 2.2 seconds after the first and both at a depth of 8 kms.

AN APPLICATION OF THE REPRESENTATION THEOREM TO THE EVALUATION OF  
ANALYTIC TECHNIQUES FOR CALCULATING MIXED-PATH RAYLEIGH WAVES

Peter Glover and David G. Harkrider  
Seismological Laboratory, 252-21  
California Institute of Technology  
Pasadena, California 91125

INTRODUCTION

In order to better understand the  $M_s$ -yield relationship for underground nuclear explosions, we need to be able to predict quantitatively the effects of lateral variations in source region geology on surface waves recorded at regional or teleseismic distances. Rayleigh waves from events in close proximity, but in different source materials, have been modeled by a variety of techniques. Basically, these techniques fall into two groups; numerical and analytical. Numerical techniques, such as finite-element or finite-difference methods, are usually employed to model complex non-linear source/structure interactions. Their principal disadvantage is that while they permit detailed investigation of the source region, this detail cannot be calculated at sufficiently large distances to determine a precise  $M_s$ . In earlier technical reports, and in Harkrider et al. (1979), Harkrider (1980), we have shown how this difficulty may be overcome through the use of the Knopoff-deHoop elastodynamic representation theorem. Here we summarize our progress on a project designed to assess the analytical techniques currently in use.

### REPRESENTATION THEOREM FORMULATION

In our previous work with the Representation Theorem (RT) we considered the case where the Source Enclosure Surface  $\Sigma_{SES}$  was an open cylinder located on the z-axis with its side intersecting the free-surface. In this case both the forcing functions and the Green's functions were obtained from half-space solutions. Here we show that if we allow  $\Sigma_{SES}$  to totally surround the source, we can use one-dimensional, spherically symmetric or whole-space forcing functions in conjunction with the half-space Green's functions, previously obtained, to calculate far-field Rayleigh waves from explosions.

Consider a point explosion at  $h_s$  (Figure 1) which generates an azimuthally symmetric distribution of stress and displacement on  $\Sigma_{SES}$ . Using cylindrical coordinates, we can write the vertical spectral displacement for the Rayleigh wave at a receiver on the free-surface as

$$\{\bar{w}_0\}_R = I_{Bottom} + I_{Side} + I_{Top}$$

with

$$I_{Bottom} = + \int_0^a \left( \dot{\bar{u}}_r \left\{ \bar{T}_{zr}^o \right\} + \dot{\bar{u}}_z \left\{ \bar{T}_{zz}^o \right\} - \dot{\bar{\sigma}}_{rz} \left\{ \bar{G}_r^o \right\} - \dot{\bar{\sigma}}_{zz} \left\{ \bar{G}_z^o \right\} \right) r_o dr_o \Big|_{z_o = h_1}$$

and

$$I_{Side} = + \int_{h_1}^{h_2} \left( \dot{\bar{u}}_r \left\{ \bar{T}_{zr}^o \right\} + \dot{\bar{u}}_z \left\{ \bar{T}_{zz}^o \right\} - \dot{\bar{\sigma}}_{rz} \left\{ \bar{G}_z^o \right\} - \dot{\bar{\sigma}}_{rr} \left\{ \bar{G}_r^o \right\} \right) r_o dz_o \Big|_{r_o = a}$$

$$I_{Top} = - \int_0^a \left( \frac{\dot{u}_r}{u_r} \left\{ T_{rz}^o \right\} + \frac{\dot{u}_z}{u_z} \left\{ \bar{T}_{zz}^o \right\} - \frac{\dot{\sigma}_{rz}}{\sigma_{rz}} \left\{ \bar{G}_r^o \right\} - \frac{\dot{\sigma}_{zz}}{\sigma_{zz}} \left\{ \bar{G}_z^o \right\} \right) r_o dr_o \Big|_{z_o = h_2}$$

where  $h_1, h_2$  are the depths of the top, bottom of the cannister respectively, and  $a$  is the radius of the cannister.

In eq. (2),  $\{T_{ij}^o\}$  and  $\{\bar{G}_i^o\}$  are the ring Green's functions given by Harkrider (1980), and  $\dot{u}_i$  and  $\dot{\sigma}_{ij}$  are the forcing functions derived from Haskell's model for an explosion in granite (Haskell, 1967). The time derivatives of stress and displacement are used to avoid problems arising from the zero frequency offset in displacement produced by the explosion. The spectral values  $\{\bar{w}_o\}_R$  are then divided by  $-iw$  prior to transforming into the time domain. Because the products in the integrands of eq. (2) are smoothly varying functions of  $r_o$  and  $z_o$ , we can divide  $\Sigma_{SES}$  into a series of annular regions, evaluate the products at the midpoint, (hereafter referred to as a node), and replace the integral by a weighted sum. The criteria for selecting the node spacing are discussed below.

The geometry of the 33 node mesh used for the initial verification of the RT method is shown in Figure 1. A ring width of 0.2km was used. The source was placed on the z-axis at a depth of 1.1km, equidistant from the top and bottom of the cannister. The oversized yield of 50mt was chosen deliberately in order to emphasise the low frequency components of the synthetic seismograms. The latter contain spectral values in the range 0-2.5hz for the homogeneous half-space runs.

Figure 2 shows the contribution of each product in the three integrals given by eq.(2) at an epicentral distance of 300.1km. Each product is identified by its forcing function component. Clearly the largest contributions come from the normal stress acting on the top and bottom of the cannister. However, careful examination of Figure 2b will show that the contributions from the displacements on the top and side have a subtle effect on both the amplitude and pulse width of the final solution.

In Figure 3 we compare the RT method seismogram with one computed directly from the analytic formulation for the Rayleigh wave from a point explosion given by Harkrider (1964,1970). The amplitudes of the two signals agree to within 3%. The arrival times of the peaks, troughs, and zero-crossings are identical. This is because the non-causal arrivals present in the total contributions from the top, bottom, and side (lowest traces Figure 2) cancel each other out exactly when the final summation of the three integrals in eq.(1) is performed.

Figure 3 also shows what happened when we allowed the explosion point to approach the top of the cannister while keeping the node spacing fixed. At a source depth of 0.9km , the two signals agree to within 4% in amplitude and the waveforms are identical. As we further decreased the shot depth, the RT method seismogram increased in amplitude with respect to the direct solution. At 0.3km, that is 0.2km from the top surface, the RT solution is both a factor of 3 too large and non-causal. Figure 4 shows the reason why. The normal stress component on the top of the cannister completely dominates the final

solution. This because the node spacing on the top surface is too great. For a source at 0.2km our choice of mesh implies that the stresses and displacements along the top surface are constant over a takeoff angle of  $45^\circ$ . Clearly, this is incorrect. By progressively decreasing the internode spacing of those nodes closest to the z-axis (see Figure 5) we found that 8 nodes with a spacing of 0.025km in the range 0-0.2km, with a subsequent doubling and redoubling in ring width along the remainder of the top surface, enabled us to match the direct solution to within 1%.

This empirical rule of 8 nodes per  $45^\circ$  of take-off angle also worked when the source was placed at 1.9km depth. In the latter case, the disagreement in amplitude between the RT method using the 33 node mesh and the direct solution was significantly smaller than for the shallow source with the same number of nodes. The non-causality was much more severe, however, indicating the coarse mesh was biasing the low frequencies in this case. When the RT method results were recomputed using the same nodal distribution along the bottom as was used for the top in the previous 47 node mesh, they agreed with the direct solution. Thus, provided that we take into account the conditions necessary to replace the integrals in eq.(2) with a weighted sum, we are not restricted to choosing a source enclosure surface such that the source is equidistant from the top and bottom. The latter case does allow us to reduce the number of nodes per  $45^\circ$  take-off angle from 8 to 5 for the 2km high cannister.

As a final verification of the RT method, we computed synthetic

seismograms for explosions with yields of 50mt, 5mt, and 1mt recorded at an epicentral distance of 1200km in the layered model CIT109 (Table 1). The synthetics are the vertical component for a surface receiver and contain spectral values in the range 0-0.5hz. We used the 33 node mesh for the RT method, and put the source at a depth of 1.1km. Figure 6 shows the results. For the 50mt explosion the peak amplitudes of the RT method and the direct result agree to within 0.6%. More importantly, with the exception of the small blip on the first downswing of the direct result (which we believe to be an artifact of the phase smoothing algorithm), the arrival times of the peaks, troughs and zero-crossings of the wavetrains agree to within the sampling interval (1sec). For the smaller yields, the peak amplitude agreement is not so good. At 5mt, the peak amplitudes differ by 7%; at 1mt the mismatch is 11%. Note however, that for the smaller yields the signals are dominated by the arrival corresponding to the Nyquist frequency, and that the lower frequency portions of the wavetrain are well matched in terms of arrival time and amplitude. Figure 7 demsonstrates our point, for when the RT method and the direct signals are convolved with the response of a long-period LRSM instrument, the wavetrains from the two methods are overlays at all three yields. Note that we did not account for inelastic attenuation in either the direct or RT method synthetics shown in this figure.

#### COMPARISON OF SYNTHETIC SEISMOGRAMS FOR LATERALLY HETEROGENEOUS MEDIA

So far we have considered only laterally homogenous media for which

the RT method is exact. However, since the forcing functions, used to test the RT method, are calculated using Haskell's one-dimensional RDP formulation for modeling the P-waves generated by an underground nuclear explosion (Haskell, 1967), the method is both fast and inexpensive. Therefore we were tempted to change the material within  $\Sigma_{SES}$  and compare the results obtained by driving the CIT109 Green's functions with these new forcing functions to the results obtained using existing analytic approximations for laterally heterogenous media given in the literature. We have dubbed this modified approach the Approximate Representation Theorem (ART) method.

The first analytical technique that we consider is a first order approximation to matching the boundary conditions across a vertical plane separating two plane-layered earth models, one representing the source region and the other the remainder of the propagation path. If we ignore mode conversion or reflection and assume normal incidence, then the total horizontal energy flux across the interface must remain constant for each mode and the amplitude of the transmitted wave is determined. For short, we will refer to this as the Conservation of Lateral Energy Flux (CLEF) method. Using the notation of Harkrider (1964) we can write

$$\left\{ \bar{w}_0 \right\}_R = - 14\pi \mu_s k_s \Psi_s(\omega) K_s(h_s) \left[ \frac{A_s A_r}{s-r} \right]^{1/2} \left( \frac{C_r}{C_s} \right)^{1/2} H_o^{(2)}(k_s \Delta_s + k_r \Delta_r)$$

where  $\{\bar{w}_0\}_R$  is defined as in eq.(1),  $\Psi_s(\omega)$  is RDP for the explosion,  $\Delta$  the epicentral distance, and the subscripts s and r denote quantities

calculated in the source medium and the propagation medium respectively. This approach was used by Bache et al (1978) to study surface waves from NTS recorded at Tuscon, Arizona and Albuquerque, New Mexico.

The second approach is to use the source-excitation/source-depth dependent quantities appropriate for the source region and combine them with the phase and medium response (surface source and surface receiver) for the propagation path. We shall refer to this second method as the Unit Transmision Coefficient (UTC) method. Again, using Harkrider's notation we can write

$$\left\{ \frac{\bar{w}_0}{w_0} \right\}_R = - i 4 \pi \mu_s k_s \bar{\psi}_s(\omega) K_s(h_s) A_s H_o^{(2)} (k_s \Delta_s + k_r \Delta_r)$$

In both (3) and (4) the source-depth excitation term is given by

$$K_s(h_s) = \left[ \frac{\dot{u}_s(h_s)}{\dot{w}_o} \right] - \frac{1}{2 \mu_s} \left[ \frac{\sigma_s^*(h_s)}{\dot{w}_o/c} \right]$$

This method was used by Alexander et al. (1975) to study the surface waves from events in the Oroville, California region, recorded at the SRO station at Albuquerque.

We computed synthetic seismograms for two source region models represenatitve of NTS. These are the Yucca Flat Tuff model and the Climax Stock Granite model given in Table 2. The source was placed at 1.1km depth. For the analytic approximations we computed synthetics for the exact analogue of the 33 node mesh geometry, labelled buried cannister in Figures 8 & 9. We also computed synthetics for the case

where the low velocity layer extended to the free surface, labelled surface cannister. All the synthetics are for a vertical component LRSM long-period instrument located on the free surface at an epicentral distance of 1200km. The source region has a radius of 2.1km, and all traces are plotted to a common scale. Table 3 gives the maximum peak-to-peak amplitude ratios of the mixed path synthetics to the corresponding amplitude of the direct solution for the laterally homogeneous model CIT109.

Figure 8 and Table 3 both show that for the Climax Stock model, where the source region rigidity is less than that for path by approximately 40%, all three methods give essentially the same result. The waveforms are nearly identical, as are the peak-to-peak amplitudes. For Yucca Flat where the rigidity contrast is large, Figure 9 shows that the waveforms from the three methods are quite different. The ART method result is a scaled version of the Climax Stock waveform. However, the scaling factor is not that predicted from the rigidity ratios. The CLEF method gives a quite different waveform. The prominent 14 second period arrival which dominates the previous results is considerably reduced in amplitude relative to the shorter periods. Table 3 shows that the amplitude ratio for the CLEF result is half that of the ART result for the buried cannister. The synthetics generated by the UTC method are completely dominated by the the shorter periods, which are further amplified in the surface cannister case. The amplitude ratio for the buried cannister is approximately a factor of two larger than the ART results.

## DISCUSSION

From a theoretical point of view, the validation of the Representation Theorem method contained in this report is quite gratifying. From a practical point of view, it is clear that we have demonstrated the inconsistency of these three approaches to correcting surface wave Green's functions for localised lateral variations in source media. The large discrepancy that we found for the Yucca Flat model indicates that we must perform a more rigorous analysis of this problem than presented here in order to find the appropriate correction. We therefore are currently undertaking a finite-element analysis of an explosion in a laterally heterogeneous half-space model which is designed to generate forcing functions on a  $\Sigma_{SES}$  placed exterior to the geologic boundary.

## REFERENCES

Alexander, S.S., R.W. Tiffet, and P. Glover, Comparison of earthquake source mechanisms for foreshock, mainshock, and aftershock sequences using Seismic Research Observatory (SRO) data, EOS, 57(12), p. 954, 1976.

Bache, T.C., W.L. Rodi, and B.F. Mason, Source amplitudes of NTS explosions inferred from Rayleigh waves at Albuquerque and Tuscon, Systems, Science and Software Topical Report SSS-R-78-3690, 1978.

Harkrider, D.G., Surface waves in multilayered media I. Rayleigh and Love waves from buried sources in a multilayered elastic half-space, Bull. Seismol. Soc. Am., 54, pp. 627-679, 1964.

Harkrider, D.G., Surface waves in multilayered media II. Higher mode spectra and spectral ratios from point sources in plane-layered earth models, Bull. Seismol. Soc. Am., 60, pp. 1937-1987, 1970.

Harkrider, D.G., P. Glover, G.A. Frazier, R.J. Apsel, and G. Fried, A method for propagating surface waves from complex seismic source regions to teleseismic distances, Earthquake Notes, 50(4), p. 29, 1979.

Harkrider, D.G., Coupling near source phenomena into surface wave generation, Proceedings of NATO Advanced Study Institute on Identification of Seismic Sources, held in Oslo, Norway, September 1980, D. Reidel Pub. Co., Dordrecht, The Netherlands (in press).

Haskell, N.A., Analytic approximation for the elastic radiation from a contained underground nuclear explosion, J. Geophys. Res., 72(10), pp. 2583-2587, 1967.

Table 1. Layer parameters for the CIT109 model

<u><math>h</math></u> (km)	<u><math>\alpha</math></u> (km/sec)	<u><math>\beta</math></u> (km/sec)	<u><math>\rho</math></u> (gm/cm <sup>-3</sup> )
14.0	6.2	3.511	2.736
0.1	6.6	3.737	2.849
20.9	6.7	3.777	2.883
0.1	8.048	4.534	3.245
4.9	8.045	4.529	3.246
10.0	8.035	4.496	3.530

Table 2  
Layer parameters for the Climax Stock and Yucca Flat models

	$\alpha$	$\beta$	$\rho$	$\mu$
<b>Yucca Flat Tuff</b>	2.35	1.3	1.86	3.14
<b>Climax Stock Granite</b>	5.33	2.78	2.67	20.63
<b>CIT109 (Upper 14 km)</b>	6.2	3.511	2.736	33.73

**Table 3**  
**(P-P) Rayleigh wave amplitude ratios**  
**(Approximation/Laterally Homogeneous) taken from the seismograms**  
**in Figures 8 & 9 compared to the rigidity ratios**

	<u>Climax Stock</u>	<u>Yucca Flat</u>
$\mu_s / \mu_r$	.612	.0932
A	.784	.511
Buried (C)	.759	.264
Buried (U)	.752	.822
Surface (C)	.777	.331
Surface (U)	.773	1.17
<b>C - CLEF method</b>		
<b>U - UTC method</b>		
<b>A - ART method</b>		

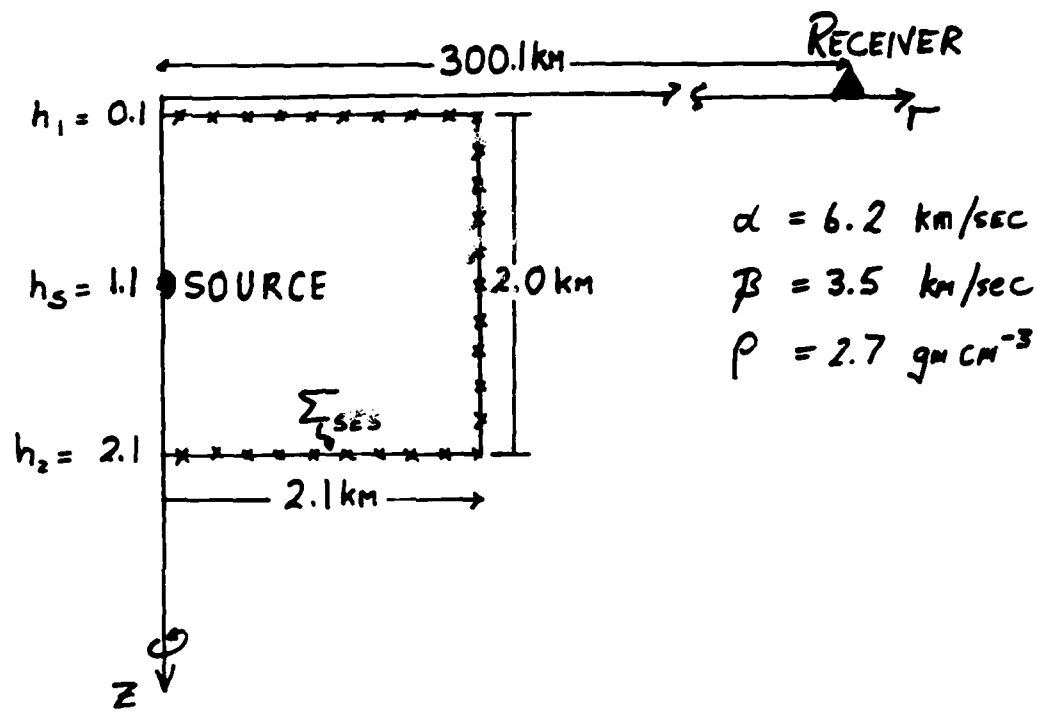


Figure 1. Geometry for the 33 node mesh calculations.

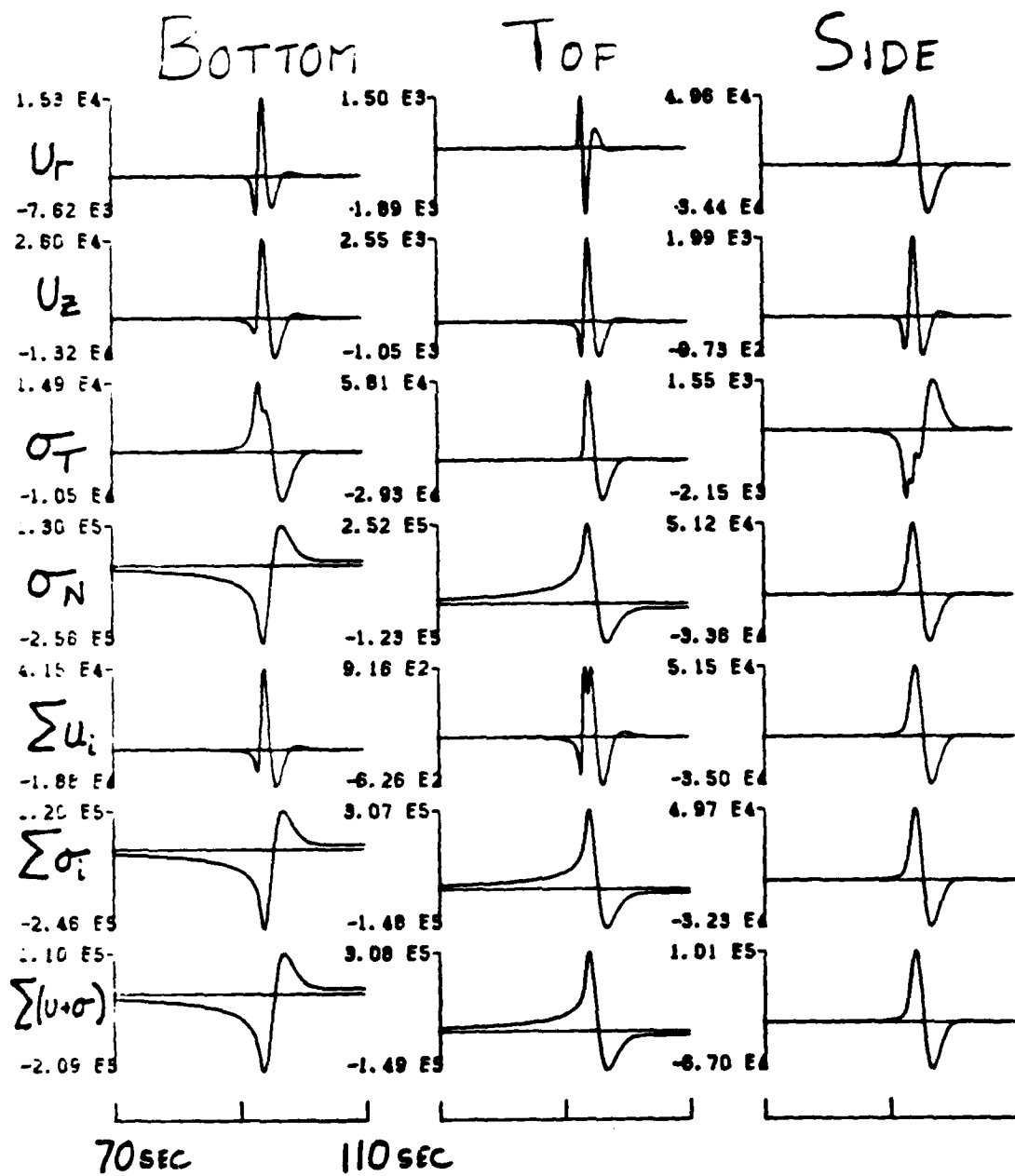


Figure 2a. Synthetic seismograms for a surface receiver at a distance of 300.1 km, displayed by forcing function component, for the bottom, side and top of the cannister. All amplitudes are in microns.

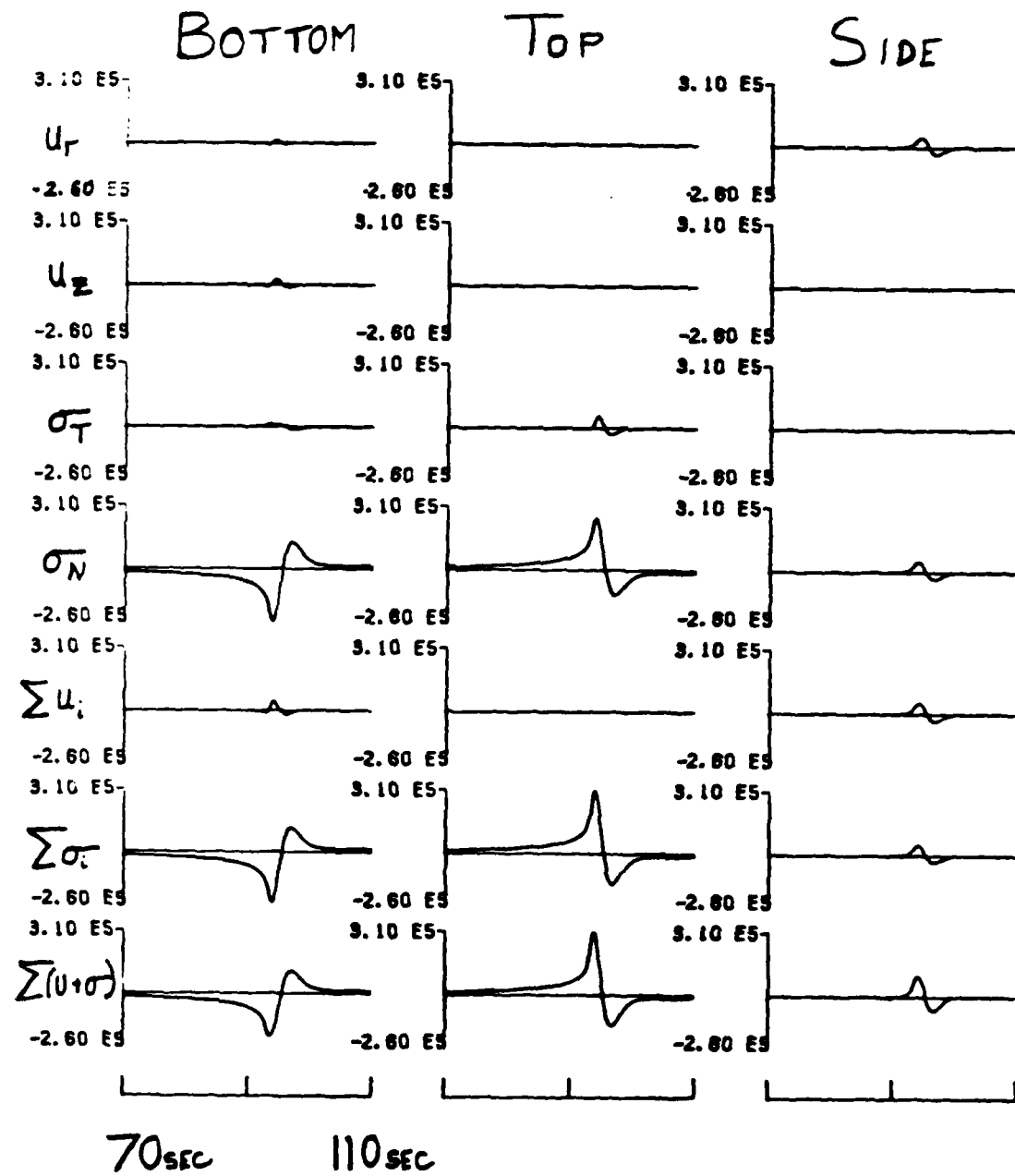


Figure 2b. The synthetic seismograms of Figure 2a plotted on a common scale.

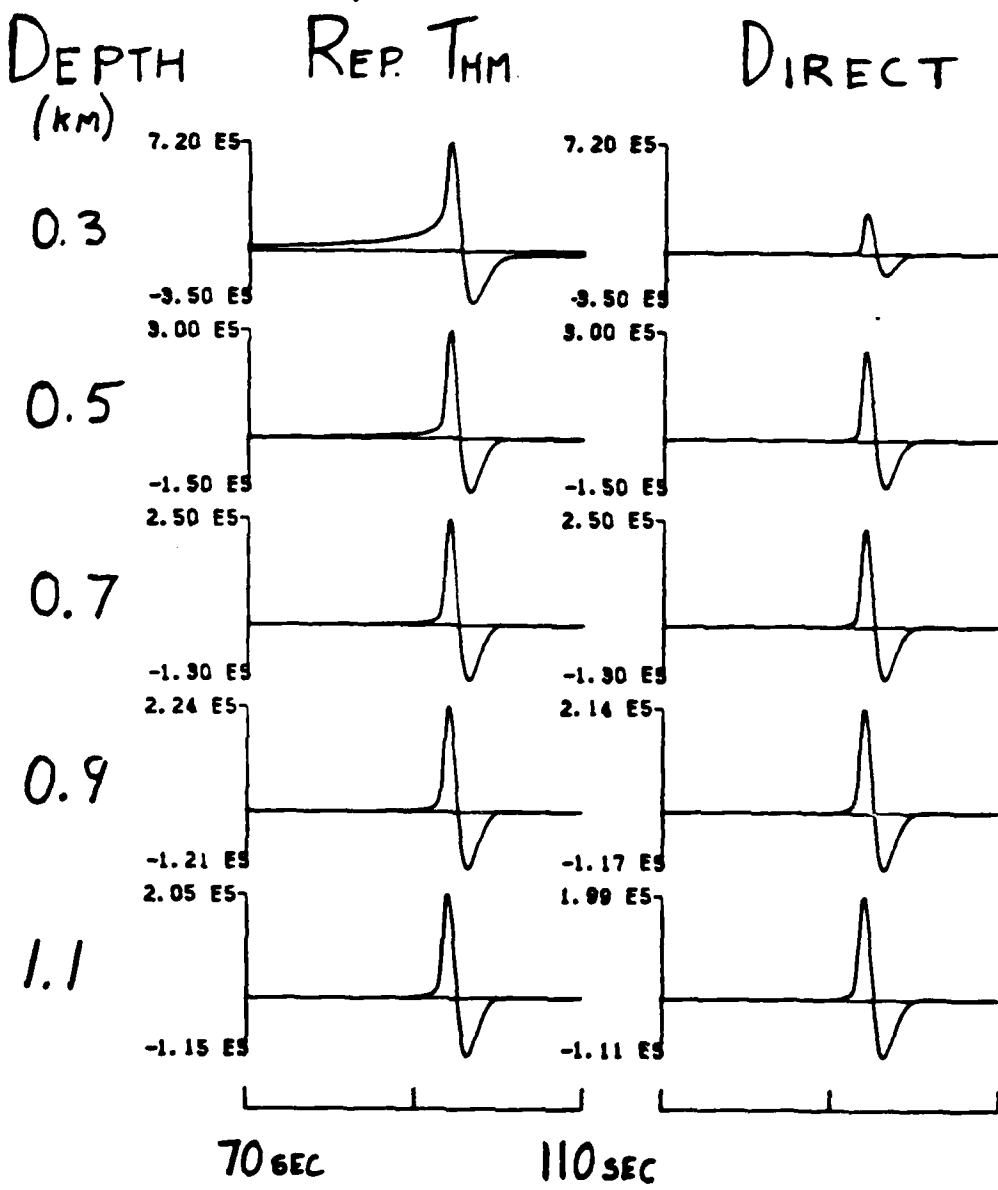


Figure 3. Comparison of the RT method synthetics with the direct solution for decreasing source depth, 33 node mesh.

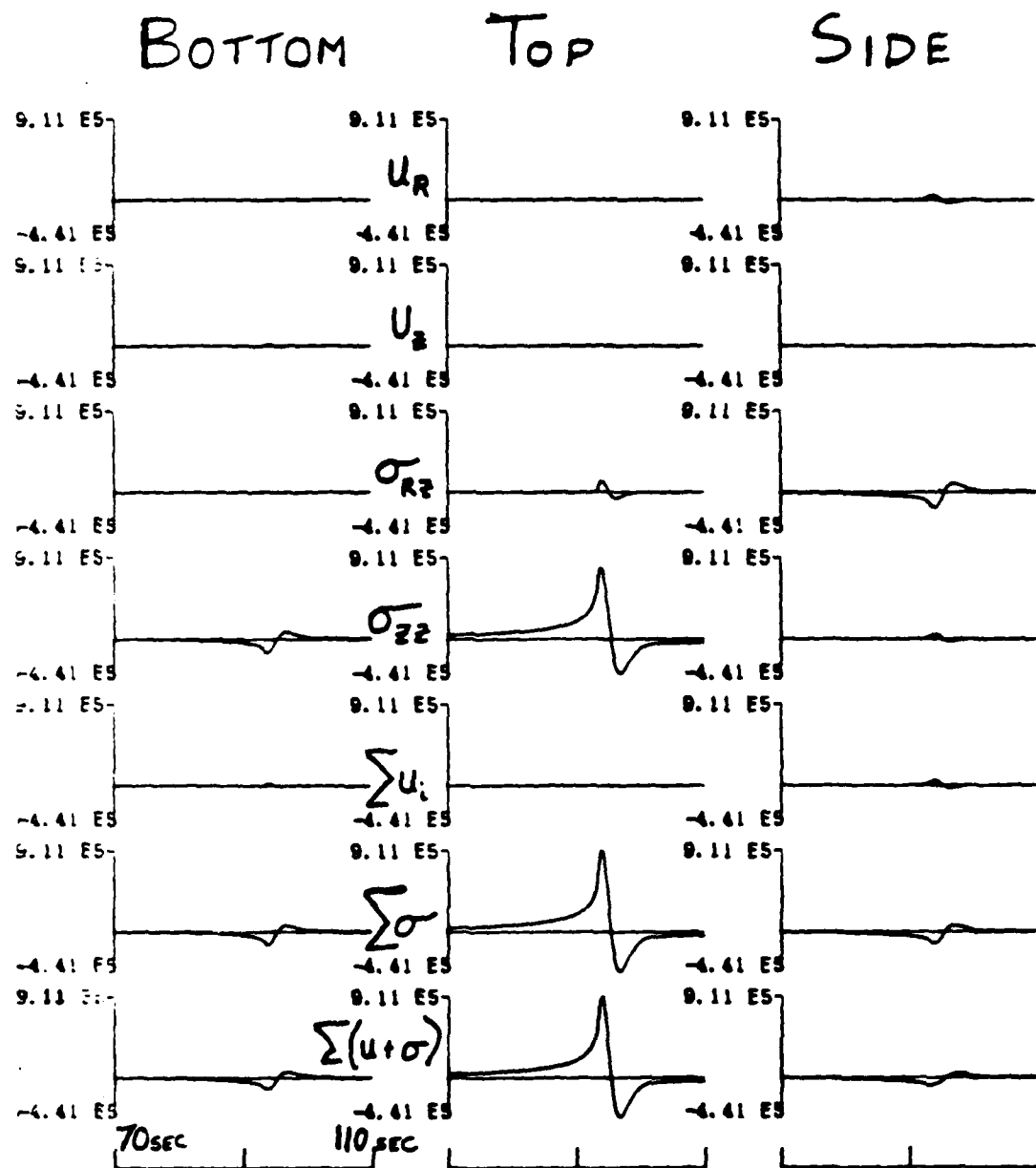


Figure 4. Relative contributions of bottom, side, and top for 0.3 km source depth, labelling as in Figure 2a.

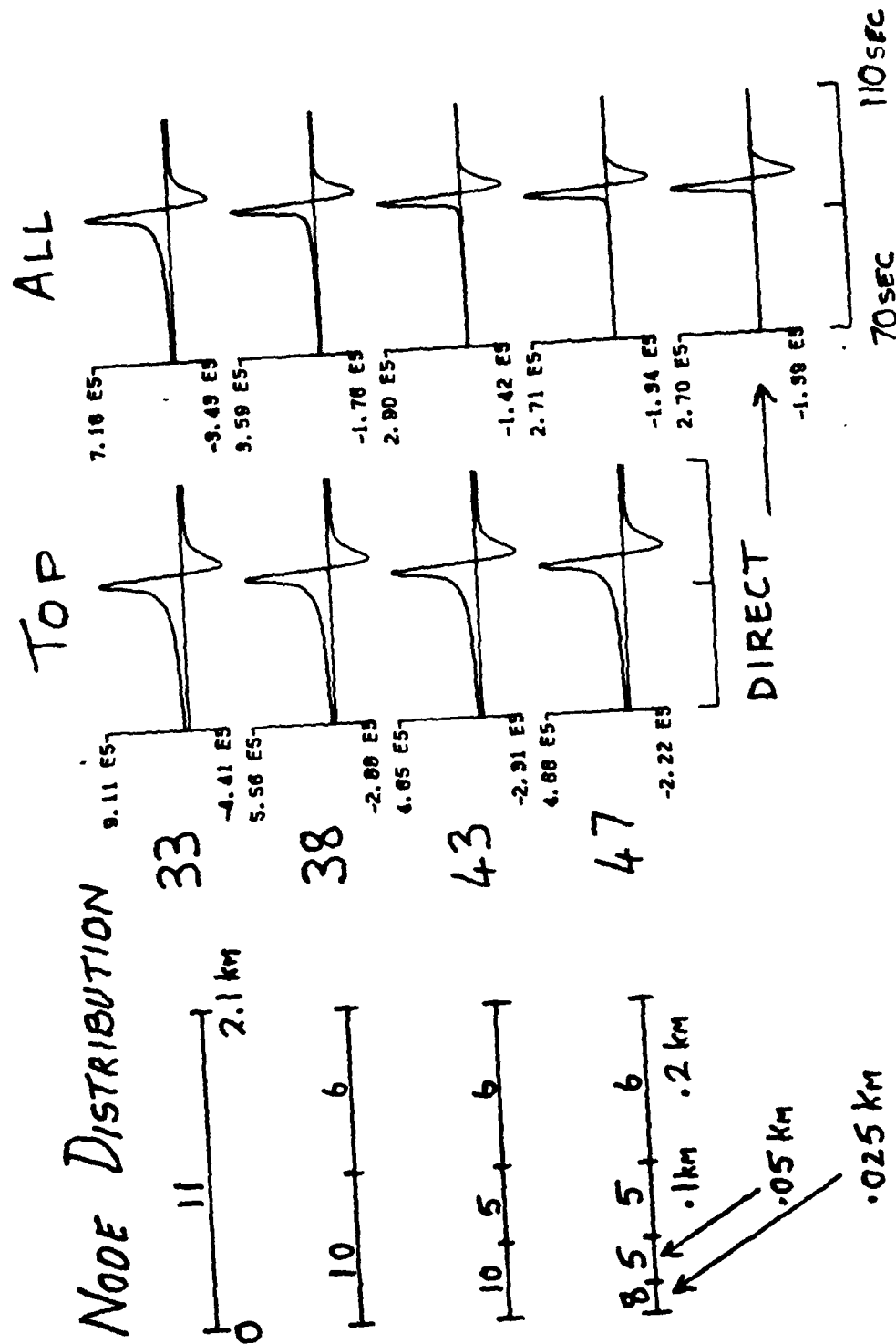


Figure 5. Effect of decreasing the node spacing on the RT method synthetic for an explosion at 0.3 km depth. Left hand cartoon shows node distribution and ring width along top surface as number of nodes in mesh increases from 33 to 47.

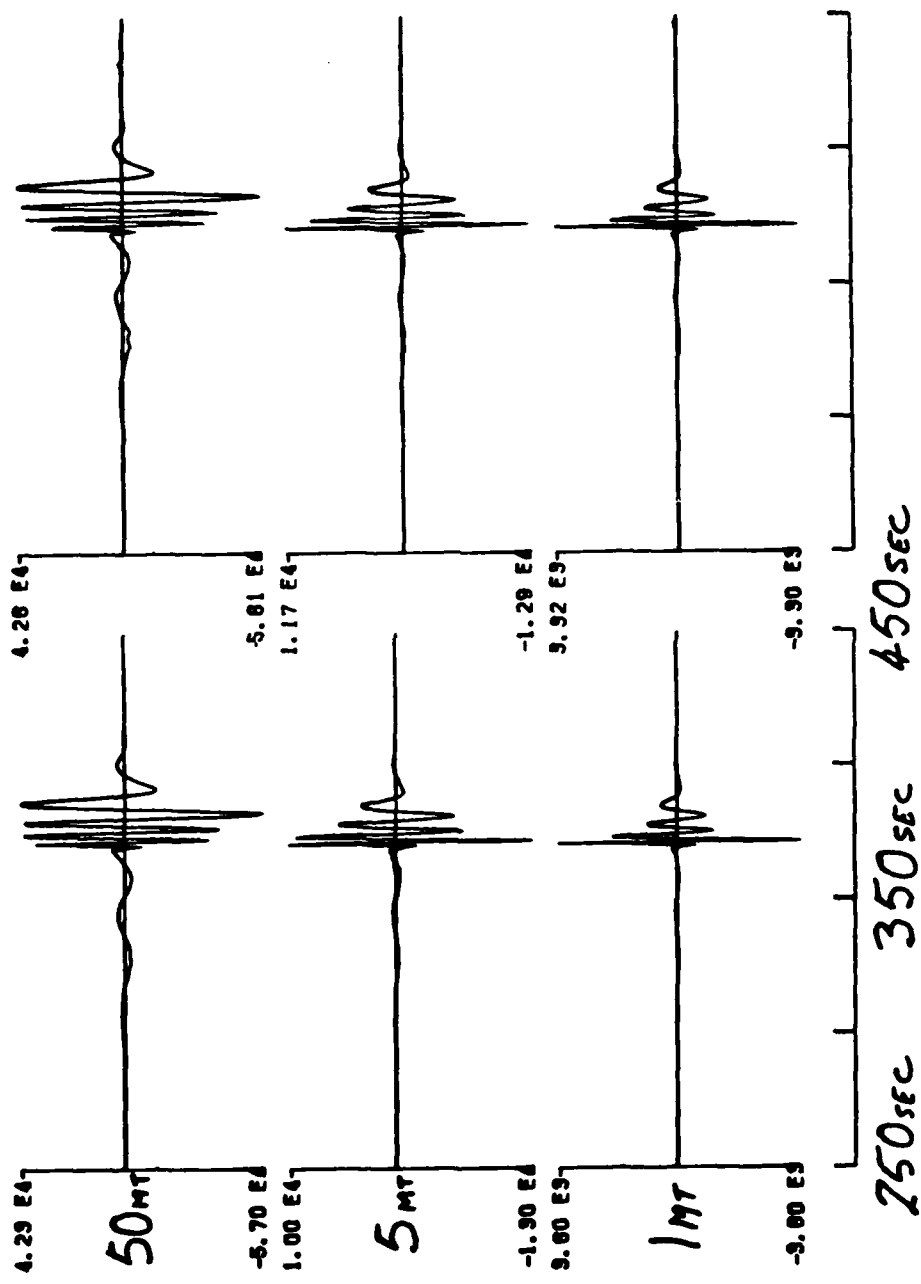


Figure 6. Synthetic seismograms for explosions of 3 yields at 1.1 km depth in model CIT109 for a vertical receiver at 1200 km distance. Amplitudes are in microns. RT method on left, direct solution on right.

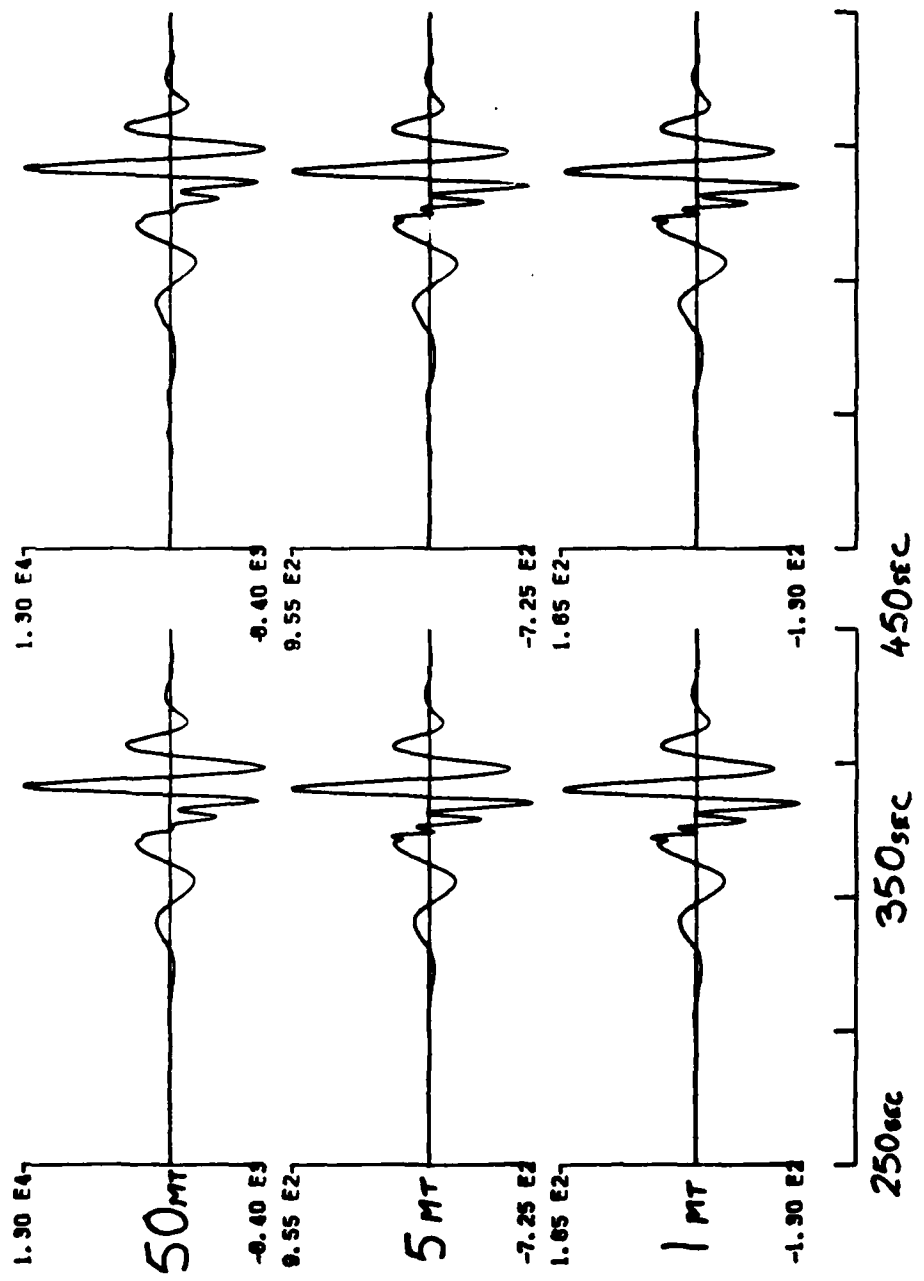


Figure 7. Same synthetics as in Figure 6 convolved with response of a LRSM long-period seismograph. Amplitudes are ground displacement in microns.

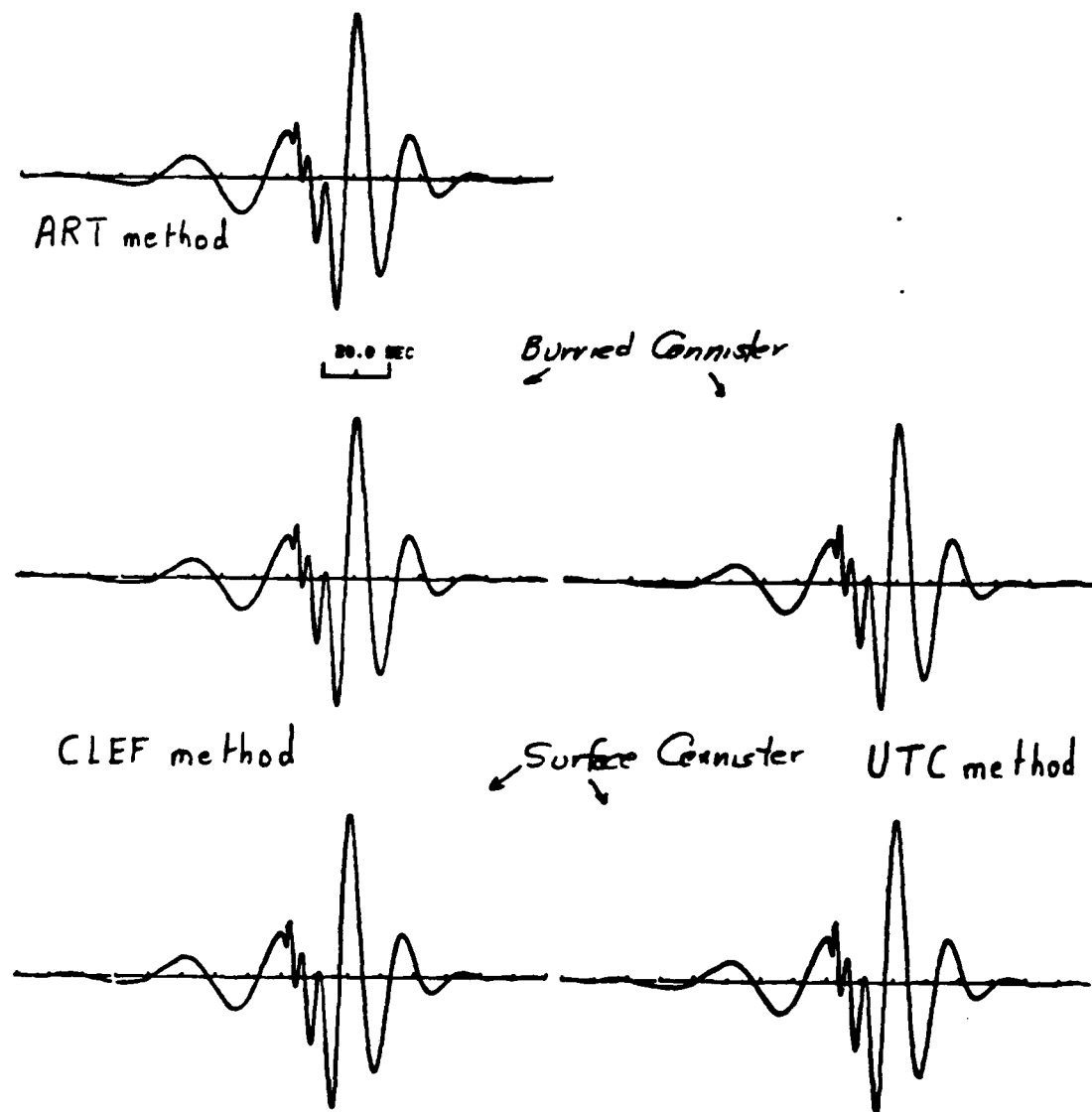


Figure 8. Comparison of synthetic seismograms for the Climax Stock model computed using the 3 approximations, LRSM long-period instrument, vertical component, at 1200 km. Source is a lmt explosion at 1.1 km depth.

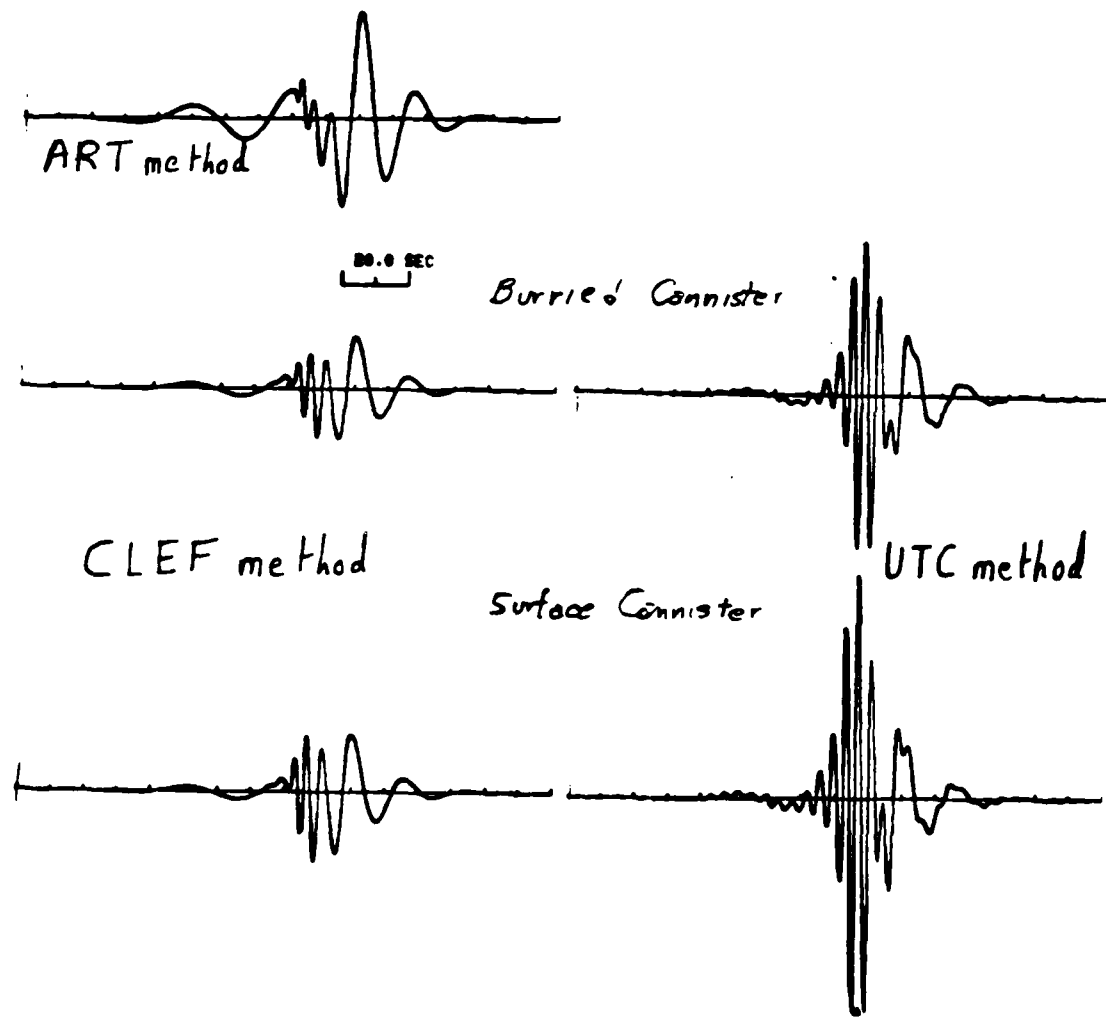


Figure 9. Comparison of synthetic seismograms for the Yucca Flat model. Details as in Figure 8.

MULTIMODE ANALYSIS OF RAYLEIGH-TYPE Lg, II:  
APPLICATION TO SOUTHERN CALIFORNIA AND THE  
NORTHWESTERN SIERRA NEVADA

by

Michel Cara\*

J. Bernard Minster\*\*

Ronan Le Bras

Seismological Laboratory  
California Institute of Technology  
Pasadena, California 91125

December 10, 1981

revised February 27, 1981

\* Now at: Institut de Physique du Globe, 5 rue Descartes, 67084 Strasbourg Cedex, FRANCE.

\*\* Now at: Systems, Science and Software, Inc., P.O. Box 1620, La Jolla, California 92038.

Abstract

The UC diagram technique described in the companion paper, (Part I) is applied to nine sets of Lg phases recorded through the CEDAR system in southern California, and two sets of Lg phases recorded along the northwestern margin of the Sierra Nevada. A clear image of the signal is obtained in time-frequency-wavenumber space, and we discuss in particular observations at 2.5 sec period, for events 200-300 km outside the profiles. From the gross features of UC diagrams we conclude that a representation of Lg as a single coherent multimode wavetrain is oversimplified in the case of southern California but is more appropriate for the Sierra block. In southern California, peaks observed at group velocities smaller than 3.2 km/sec are not predicted by realistic crustal models of the area, and are probably due to lateral heterogeneities effects such as mode conversion and multipathing. On the other hand, for group velocities between 3.2 and 3.6 km/sec, peaks observed in either area can generally be interpreted in terms of overtones excited at the source and propagating through spatially averaged structures, although care must be taken to monitor the stability of the algorithm on actual short period records.

## I. Introduction

We have shown in a companion paper (Cara and Minster, 1981; Part I) that analysis of short period vertical seismograms of Lg along a 300 km linear array of about ten stations should allow us to isolate Rayleigh wave overtones in the period range 2 to 5 seconds. At epicentral distances of a few hundred kilometers, Lg merges with its high frequency counterpart, usually called Sg. We shall, however, use the notation Lg for the relatively long-period signal under study here, even at a few hundred kilometers from the source. As we shall see, this signal is generally observed at rather low group velocities ( $\sim 3.3$  km/sec) and corresponds to the  $Lg_2$  phase defined by Bath (1956).

Observations of Lg have long been reported in central and southern California (Gutenberg, 1955; Press, 1956). Press (1956) found a velocity of 3.54 km/sec for the first Lg arrivals observed in central and southern California, at distances 315 to 870 km. The SCARLET array and the CEDAR digital recording system provide a good opportunity to apply the method described in Part I to Lg data in southern California (Figure 2b).

For comparison, we shall also analyze Lg phases recorded along the northwestern margin of the Sierra Nevada at CALNET stations. In this case, the path lies mainly along the Sierra batholith and is potentially less complicated (Figure 13).

As discussed in Part I, one of the most stringent implicit assumptions of the method is that the crust is laterally homogeneous. Even in the case of azimuthal homogeneity about the source, crustal changes along the profile can lead to difficulties (e.g., mode conversion, local

changes in phase velocity...). The main question dealt with in this paper is whether lateral variations are small enough, relative to the analytical resolution power of the array, that each overtone appears as an isolated peak on the UC diagram. As we have shown in Part I, too strong lateral variations broaden the peaks and can even split them into several peaks.

Before turning to a description of our experimental results, we first proceed with an analysis of noise and instrumental limitations on the method for SCARLET. Experimental results which make use of this network are described in sections III and IV, and further results which make use of CALNET stations are presented in section V.

### II. Instrumental and Noise Constraints for CEDAR Data

The SCARLET network comprises over 150 short period vertical seismic stations in southern California (e.g., Hutton et al., 1979). This network is monitored through the CEDAR digital recording system (Johnson, 1979). Both network and recording system are designed for optimal detection, recording and routine processing of small local earthquakes. Thus, despite the obvious advantages of processing digital data through a stacking algorithm, we are faced with serious limitations when looking at late arrivals such as Lg, for sources outside the network.

Due to these constraints, usable Lg phases from routinely archived data are generally limited to events at epicentral distances 200 km to 700 km and with local magnitudes  $M_L \sim 4.0$  to 4.4. Signals from larger events are often clipped on too many stations at these distances, and routine recordings of farther events are usually too short to include Lg at all but the nearest stations. We report here on observations for these

distance and magnitude ranges. Most sources used in this study are earthquakes located in the Sierra Nevada-Owens Valley seismic area near Bishop, California (e.g., Hileman et al., 1973; Hutton et al., 1979).

Figure 1 shows a typical magnification curve for the complete seismographic system (Station + telemetry + recording system). Although the equipment varies somewhat from station to station, the magnification curve remains much the same in the period range of interest. The effective dynamic range of the system is limited in practice to about 45 db by the telephonic FM transmission between field site and the Seismological Laboratory; this is much less than the dynamic range of either the seismometer-amplifier (~ 65 db) or of the 12 bit digital recording system. However, as seen from Figure 1, this permits retrieval of information to a period of at least 5 sec if the 0.5-1.0 sec component is just on scale and saturation does not occur at other frequencies.

To correct for instrumental differences between stations, a frequency domain deconvolution was performed through 1) phase correction in the entire frequency range, followed by 2) amplitude deconvolution down to the -45 db level, constant amplitude correction between -45 db and -65 db (~ periods 5-10 sec), and low-cut filtering beyond that point. We used the theoretical transfer functions reported by Kanamori et al. (1979) and Archambeau (1979). In view of remaining large uncertainties in the actual gains, the deconvolved ground displacement records were normalized to the same amplitude in the group velocity window 3.1-3.6 km/sec.

Seismic noise is particularly important in the period range 2-5 sec, and thus constitutes an obvious source of complications when applying the UC diagram technique described in Part I to CEDAR data at these

periods. In order to assess the stability of the algorithm in the presence of noise, we have performed a numerical experiment with a synthetic signal superimposed on natural seismic noise. The experiment simulates Lg propagation along profile 1 (Figure 2b) for a fictitious source with the same location as event 1 (Table 1), and the crustal structure derived from the refraction model of Kanamori and Hadley (1975). Details on the crustal structure and on the composition of synthetic Lg are found in Part I (see, in particular, Figure 2, which corresponds to profile 1).

Seismic noise recorded in January, 1980 during a false alarm trigger of the CEDAR system is then added to the synthetic Lg phases, with different "signal-to-noise" (S/N) ratio, and the result processed through the full algorithm. We define here S/N in the time domain as the ratio of synthetic Lg amplitude to noise amplitude after deconvolution (maximum peak to trough amplitude in the velocity window 3.1-3.6 km/sec).

For pure seismic noise (S/N = 0), the 2.5 sec period UC diagram is shown in Figure 3. As could be expected, several peaks appear with rather random locations. These peaks could generate artifacts in the analysis of actual data. It is unfortunately impossible to identify them as noise rather than signal if no a priori knowledge of overtone peaks is available from independent geophysical information.

Figure 4 shows the profile of synthetic Lg plus natural noise, for S/N = 2. The corresponding UC diagram at 2.5 sec is given on Figure 5. It is very encouraging that the observed peaks remain so close to their theoretical positions, thus indicating a good stability of the algorithm in the presence of moderate seismic noise. Even with S/N = 0.5, overtone

peaks are still recognizable (Figure 6) but are either strongly attenuated (mode 3) or perturbed (mode 2).

Thus, although a high noise level is a clear source of difficulties, we may conclude that the method is applicable at low to moderate noise levels. A practical criterion is that the noise amplitude be low at earlier times (i.e., greater group velocities) than Lg arrivals for the period considered. For example, it is less than 20% on the UC diagram shown on Figure 5, and nearly 50% on Figure 6.

### III. Experimental Results: Southern California

Proposed models of crustal structure show a surprising degree of lateral homogeneity over wide areas of southern California. From refraction data, Kanamori and Hadley (1975) found no significant difference between the upper crust of the western Mojave desert, the central and eastern Transverse Ranges, and the northern Peninsular Ranges (Figure 2a). The deeper crust is not so well-constrained in their study, but Moho reflections and an estimate of the  $P_n$  critical distance led the authors to fix Moho depth between 30 and 35 km. In a further study, Hadley and Kanamori (1979) concluded that the model is consistent with fundamental Rayleigh mode data if Poisson's ratio is about 0.25 in the crust. Moreover, the latter study has also shown that a similar S-velocity structure can account for Rayleigh wave dispersion in the Peninsular Ranges, Poisson's ratio being somewhat larger ( $\sim 0.28$ ) in that case.

Direct calculation of Rayleigh wave overtone phase velocity in the period range 2-5 sec yields essentially the same results for the two models proposed by Hadley and Kanamori (1979). Thus, although strong E-W

lateral variations exist in the Peninsular Ranges (Hadley and Kanamori, 1979), it seems that no drastic change in overtone dispersion is expected a priori along N-S profiles running through western Mojave desert, the central Transverse Ranges, and the Peninsular Ranges. For this reason, we chose profiles similar to those displayed on Figure 2b for an initial experimental study. A typical section for event 1 (Table 1) recorded along profile 2 (Figure 2b) is displayed on Figure 7, and after deconvolution, on Figure 8. Since the traces have been normalized to have the same amplitude in the group velocity window 3.1-3.6 km/sec, noise levels are quite enhanced at the farthest stations on Figure 8. Figure 9 shows the corresponding UC diagram at 2.5 sec. This period was chosen for purposes of illustration as a compromise between 1) instrumental constraints which restrict us to periods shorter than 5 sec as discussed earlier, and 2) theoretical results showing that, at periods shorter than 2 sec, the spacing and position of phase velocity curves are very sensitive to the details of crustal structure. The same event, recorded along profile 1 (Figure 2b) yields the UC diagram shown in Figure 10.

Figures 9 and 10 exhibit significant differences, particularly in the details of energy distribution in the UC plane, but also some fundamental similarities. Compared with the synthetic Lg mixed with moderate to strong natural noise shown on Figures 5 and 6, the present UC diagrams display a significantly different pattern. For both synthetic and actual data contour levels are low for group velocities greater than 3.5 km/sec, but high energy levels persist for group velocities smaller than 3.2 km/sec in the case of actual data whereas little late energy is observed on the synthetics. We have found this pattern on all UC diagrams calculated at

this period from SCARLET/CEDAR data. This includes an aftershock of the August 6, 1979 central California Coyote Lake earthquake, recorded along a NW-SE profile across the network, and a Baja-California event (south of the network) recorded along a profile similar to profiles 1 and 2 (Figure 2b). In the latter case, while clear Lg arrivals were found on all records (at distances from 660 km to 1050 km), a particularly complicated pattern emerged on UC diagrams for  $U \leq 3.5$  km/sec, but a very low contours level ( $\leq 10\%$ ) is observed at higher group velocities.

The general character of observed diagrams shows that 1) the "noise" level is suitably low before Lg arrivals for the  $M_L \sim 4.0-4.4$  events we have examined on SCARLET, and 2) late arrivals are systematically observed, which cannot be explained in terms of overtones excited at the source and propagating along direct paths. Spurious peaks observed for example in Figure 9 and 10 are thus probably not due to random noise, but to Lg-type signals propagating through a laterally varying crust. In particular, peaks observed at  $U \leq 3.2$  km/sec could be overtones excited by secondary sources, either along the direct path (e.g., mode conversions from Rg to overtones at shorter distances), or laterally by reflection off accidents in the crust. Lateral arrivals might play a major role in the case of the Baja California event mentioned above, due to strong lateral variations in the vicinity of the direct path (e.g., Thatcher and Brune, 1973).

In view of this tentative interpretation, we first focus our attention on the peaks observed between 3.2 and 3.5 km/sec on Figures 9 and 10. Notice that they lie close to the theoretical UC coordinates calculated for the crustal structure used earlier in Section II. Peaks tentatively identified as modes 1 and 3 on Figure 9, as indicated by the

arrows, remain at nearly the same place on Figure 10, although mode 1 is weak in the latter case. On the other hand, poorer stability is observed near the theoretical position for mode 2, and a strong peak emerges on Figure 9 between modes 2 and 3, which requires an explanation. But the first order of business is to follow the peaks tentatively identified on Figures 9 and 10 as functions of period, and thus retrieve experimental dispersion curves for these modes.

We have devised for this purpose an automatic algorithm which retrieves piecewise linear dispersion curves in UCT space from a set of UC diagrams computed at several periods T. (In the present case we have  $1.8 \leq T \leq 5$  sec). The curves are initially labelled as they pass through peaks identified as overtones at a reference period (e.g., modes 2 and 3 at 2.5 sec on Figure 10.) Three criteria are used to follow continuously the peaks from a given period T to a neighboring period  $T + \Delta T$ , in the form of upper limits allowable on 1) the relative peak amplitude variation  $\Delta A/A$ , 2) the change in group velocity  $\Delta U$ , and 3) the departure  $\Delta C$  from the predicted phase velocity  $C_p$  at  $T + \Delta T$  from observed phase and group velocities at T. More specifically the third criterion assumes that:

$$C_p^{-1}(T + \Delta T) = C_p^{-1}(T) + (\Delta T/T) [C_p^{-1}(T) - U^{-1}(T)].$$

The search for a continuous curve stops when one or more of these criteria is not met.

Figure 11 depicts phase velocity curves derived from profiles 1 and 2, with  $\Delta A/A \leq 0.3$ ,  $\Delta U \leq 0.1$  km/sec  $\Delta C \leq 0.1$  km/sec; the period spacing varied from 0.2 to 0.5 sec between 1.8 and 5 sec. Also shown on

this figure are theoretical curves calculated from the Rayleigh wave model of Hadley and Kanamori (1979) for the western Mojave and the central and eastern Transverse Ranges. This model was chosen in this study because it explains the Rayleigh waves at longer periods, it is slightly different from the one used previously, in that it includes a mid-crustal low velocity zone near 15 km depth. This is the cause of the proximity of modes 1 and 2 near 1.5 sec. (Differences between dispersion curves for the two models affect mainly periods shorter than 2 sec.

The closeness of these experimental overtone phase velocity curves to the theoretical curves for crustal models derived from independent geophysical data -- including fundamental Rayleigh mode observations -- gives us some confidence that the method is capable of retrieving spatially averaged phase velocity curves from Lg records. On the other hand, it should not be forgotten that only a few observed peaks are associated with these curves, even when only the "first Lg arrivals," with the highest group velocities, are considered. Thus, the significance of phase velocity curves such as those shown on Figure 11 must be assessed carefully before they are used to constrain crustal models.

#### IV. Stability of Observations in Southern California

In addition to profiles 1 and 2 for event 1, events 2, 3 and 4 (Table I) have been processed along profiles similar to profile 1 (Figure 2b). This gives us an opportunity to check the stability of phase velocity estimates such as those shown on Figure 11. Events 5, 6 and 7 have been processed along profiles running from CLC, toward the vicinity of Yuma, S.E. of the Salton Trough (Figure 2a). All profiles avoid the Salton Trough, where crustal thinning and anomalous mantle structure is expected (e.g., Savino et al.,

1977; Fuis et al., 1980). But the latter profiles are different enough to allow us to look for possible lateral variations. Phase velocities at 2.5 sec from these 9 profiles are shown in Figure 12, where only the first three highest peaks are shown, except for profile 2 (event 1) for which the fourth highest peak is also shown. Furthermore, peaks with a group velocity smaller than 3.2 km/sec are assumed to represent secondary arrivals and are not shown. Phase velocities tentatively assigned to the same mode are linked by dashed lines on Figure 12 (peak closest to theoretical mode coordinates in the UC plane), and the highest peak is singled out in each case.

At 2.5 sec period, the highest peak can thus be generally associated with the second overtone, and observed values scattered over less than 0.2 km/sec for this mode. Although this is very comparable to the scatter for fundamental Rayleigh wave phase velocities found by Hadley and Kanamori (1979) between 15 and 25 sec, the present situation is actually very different, because of the mode identification procedure we have used (the observed maximum scatter being in fact of the same order of magnitude as the theoretical phase velocity spacing between overtones). This stability test has been extended to other periods by continuously following the peaks as indicated in Section III. The standard deviations of observed phase velocities are generally greater for overtones 1 to 3, in the period range 2-4 sec, than the differences with theoretical values predicted by the model derived from Kanamori and Hadley (1975), (Table 2), so that interpretation of those measurements in terms of details in the crustal structure would constitute a rather hazardous extension of this work, probably unwarranted at this point.

The stability test we have just described shows that lateral inhomogeneities probably play a major role, not only where late arrivals are concerned, but also in the interpretation of early peaks as overtones. Based on the results of Section II, an explanation of the observed instabilities in terms of seismic noise can be rejected. On the other hand, because station distribution varies from profile to profile -- even within each of the two groups "East" and "West" shown in Figure 12 -- reproducibility of propagation characteristics of Lg observed along these different sets of stations is not guaranteed. Further complications can arise from different source excitation of the modes for the seven events used (Table 1).

Lateral heterogeneities in the first portion of the paths, together with different amplitude and phase radiation patterns at the source can result in apparently incoherent phase propagation along profiles with non-zero azimuthal aperture, such as those on Figure 2b. Intra array structural variations of any kind can also contribute to the scatter on Figure 12, because the profiles sample the area in different ways. Irrespective of their actual cause, phase perturbations might be construed as resulting from a combination of the two extreme types (random and coherent) used in Part I for a numerical experiment. Random phase perturbations (statistically independent from station to station) could be due for example to small scale intra array lateral inhomogeneities with a scale length of 10 km or less, as in the case of LASA (Aki, 1973; Capon, 1974). Coherent phase velocity variations over a portion of the profile, or azimuthal variations between source and closest station could result in a coherent perturbation over a subgroup of stations.

In the light of the phase perturbation experiment conducted in Part I, instabilities in the measurements noted on Figure 12 could clearly be accounted for in this fashion. However, the fact that rather consistent results are nevertheless obtained from SCARLET data shows that we are operating close to or within the conditions of applicability of the method (i.e., 1 to 2 sec random fluctuations and 5% phase velocity variations along significant portions of the profiles). Thus better results and greater success can be expected from similar arrays located on a homogeneous crust.

V. Further Experimental Results: The Northwestern Margin of the Sierra Nevada

In contrast to the southern California profiles (Figure 2b), two longitudinal profiles along the Sierra Nevada (Figure 13) lie entirely within the same geological province. We might, therefore, anticipate that fewer difficulties linked to lateral variations should be encountered in the latter case, especially if the source is also within the Sierra block (e.g., S1 on Figure 13).

The crustal structure of the Sierra Nevada has been studied by seismic refraction. Using chemical explosions near San Francisco, California and Eureka, Nevada, Eaton (1963) found evidence of crustal thickening, from 20 km under the Coast Ranges and the Great Valley to about 50 km under the High Sierra. Crustal thickness drops again to about 30 km in the Basin and Range (Bateman and Eaton, 1967), indicating that the crustal

root is centered approximately beneath the Sierra Crest. Based on an unreversed profile between the Nevada Test Site and San Francisco Bay, Carder et al. (1970) proposed a model with no crustal thickening under most of the western Sierra, and a maximum crustal thickness of about 40 km beneath Owens Valley and the White Mountains, East of the Sierra front. Upon reanalysis of the San Francisco-Eureka profile, together with other profiles in the southwestern United States, Prodehl (1970) suggested a maximum Moho depth of 42 km beneath the Sierra crest and Owens Valley. Crustal thinning is progressive to the west, to a thickness of about 28 km near the eastern margin of the Great Valley. Note that gravity data also tend to support an offset of the crustal root to the east of the Sierra block, with a minimum Bouguer anomaly of -250 mgal in the northern part of Owens Valley (Prodehl, 1970).

The main point of interest to us is that structural inhomogeneities seem to be fairly mild along the western margin of the Sierra, where we chose our profile (Figure 13), as most structural variations appear to lie to the east of this profile. It seems therefore justifiable to apply the UC diagram analysis in this case.

We analyzed Lg records from two events, labelled S1 and S2 on Figure 13 and Table 3. The profile for event S1 is shown on Figure 14 (after deconvolution) and the corresponding UC diagram at 2.5 sec period is displayed on Figure 15. This diagram exhibits the same fundamental characteristics which were found for southern California profiles. Contour levels are low for group velocities larger than 3.5 km/sec, and some late energy remains for group velocities slower than 3.2 km/sec, although much less than in the case of southern California profiles. We tentatively

identify the clear peaks labelled A and B on Figure 15 with the second and third overtones, and the third strong peak (C) with the first overtone, in spite of its low group velocity. Much the same patterns were found for event S2, although the S/N ratio was not quite as favorable, and peaks were consequently not so clear (note also that the path for S2 crosses the Garlock fault, and includes a portion of the Mojave block in addition to the Sierra block, and is therefore not as simple as the path for S1).

By following these peaks as functions of period using the criteria described earlier, we find the experimental dispersion curves shown on Figure 16. The results from sources S1 and S2 are reasonably consistent with each other, and quite different from the experimental results obtained earlier for southern California (Figure 16). Thus, should our interpretation be correct, the overtone dispersion data confirm the large differences between the crustal model of Hadley and Kanamori (1979) for southern California (Figure 11) and a model for the Sierra Nevada derived from the P wave model of Carder et al. (1970) using 1.78 for the ratio of P on S velocity. The latter model provides a fairly good fit to the observed dispersion of overtones 2 and 3, but the predicted phase velocity for the first overtone is too high at the shorter periods. This can be remedied in part by introducing a low velocity superficial layer, as shown on the Figure. Such a layer might be found indeed along our profile in the form of metavolcanic rocks, although our scanty data set hardly constitutes definitive evidence in favor of such an interpretation. Nevertheless, we regard the internal consistency of our observations, as well as the clear differences between two geographical regions known to have different

crustal structures as encouraging indications that the method yields physically meaningful measurements, and deserves more extensive and systematic applications.

#### VI. Conclusions

Application of the UC diagram technique to Lg phases recorded on the SCARLET network in southern California and the CALNET network along the northwestern margin of the Sierra block yields in both cases a clear image of the time-frequency-wavenumber content of the signal, with a spatial resolution of several hundred kilometers.

Gross features of observed UC diagrams show that a representation of Lg as a coherent single multimode wavetrain propagating across southern California is an oversimplified view even at rather low frequencies. For example, realistic crustal models for the area do not predict the peaks observed at group velocities smaller than 3.2 km/sec at 2.5 sec period. Such peaks can be due either to secondary overtone excitation along the direct path or to lateral reflections and refractions. On the other hand, strong peaks found at group velocities between 3.2 and 3.5 km/sec can generally be interpreted as direct arrivals of overtones excited at the epicenter and propagating through a structure which is a spatial average for the area. Instabilities of phase velocity estimates for several events and profiles with a priori similar structures show however that lateral heterogeneities also play probably a major role for the peaks identified with overtones on UC diagrams in southern California.

A somewhat simpler pattern emerges on UC diagrams for Lg phases propagating along the Sierra batholith. Specifically, at 2.5 sec periods, no strong peak is observed for group velocities slower than 3.2 km/sec. Peaks found between 3.2 and 3.5 km/sec can be tentatively identified with overtones, but only two sets of records have been processed and it is difficult to place confidence limits on these observations.

Perhaps the most important observation is that, in spite of slight instabilities, UC diagrams from either SCARLET/CEDAR data or CALNET data exhibit rather consistent patterns in the group velocity window 3.2-3.5 km/sec. We concluded in Part I that the method is stable against random phase fluctuations not exceeding half a cycle, or coherent phase velocity variations below the resolution threshold of the array. The results of the present paper strongly suggest that these conditions are nearly, if not clearly, satisfied for the Lg records processed in this study. This opens the possibility of using this technique for structural studies by inversion of overtone dispersion curves, particularly in regions with at most weak lateral variations.

#### Acknowledgements

We thank the staff of the Seismological Laboratory, and C. Johnson for considerable help in manipulating CEDAR data. D.G. Harkrider kindly provided computer programs to compute synthetics. G. Eaton and G. Poupinet were very helpful in selecting and digitizing CALNET data. This research was supported by the U.S. Geological Survey under Contract No. 14-08-0001-18331 and the Advanced Research Project Agency of the Department of Defense,

and was monitored by the Air Force Office of Scientific Research under Contract No. F49620-77-C-0022. M. Cara was supported by a CNRS-NSF fellowship (French-U.S. convention).

References

Aki, K. (1973). Scattering of P waves under the Montana Lasa, J. Geophys. Res. 78, 1334-1346.

Allen, C.R., P. St. Amand, C.F. Richter and J.M. Nordquist (1965). Relationship between seismicity and geological structure in the southern California region, Bull. Seismol. Soc. Am. 65, 753-797.

Archambeau, C. (1979). Earthquakes hazards determinations based on tectonic stress measurements, Technical Report #3, USGS Contract No. 14-08-0001-16773.

Bateman, P.C. and J.P. Eaton (1967). Sierra Nevada batholith, Science 158, 1407-1417.

Bath, M. (1956). A continental channel wave, guided by the intermediate layer in the crust, Geofis. Pura Appl. 38, 19-31.

Capon, J. (1974). Characterization of crust and upper mantle structure under LASA as a random medium, Bull. Seismol. Soc. Am. 64, 235-266.

Cara, M., and J. B. Minster, (1981), Multimode analysis of Rayleigh-type Lg, I: Theory and applicability of the method.

Carder, D.S., A. Qamar, T.V. McEvilly (1970). Trans-California seismic profile - Pahute Mesa to San Francisco Bay, Bull. Seismol. Soc. Am. 60, 1829-1846.

Eaton, J.P. (1963). Crustal structure from San Francisco, California, to Eureka, Nevada, from seismic refraction measurements, J. Geophys. Res. 68, 5789-5806.

Fuis, G.S., W.D. Mooney, J.H. Healy, G.A. McMechan, and W.J. Lutter (1980). Crustal structure of the Imperial Valley region, in press.

Gutenberg, B. (1955). Channel waves in the Earth's crust, Geophys. 20, 283-294.

Hadley, D. and H. Kanamori (1979). Regional S-wave structure for southern California from the analysis of teleseismic Rayleigh waves, Geophys. J. 58, 655-666.

Hileman, J.A., C.R. Allen and J.M. Nordquist (1973). Seismicity of the southern California region, 1 January 1932 to 31 December 1972, Seismological Laboratory, California Institute of Technology, Pasadena, California.

Hutton, K.L., C.R. Allen, A.C. Blanchard, S.A. Fisher, P.T. German, D.D. Given, C.E. Johnson, V.D. Lamanuzzi, B.A. Reed, K.J. Richter and J.H. Whitcomb (1979). Southern California array for research on local earthquakes and teleseisms (SCARLET), Caltech-USGS monthly preliminary epicenters, Seismological Laboratory, California Institute of Technology, Pasadena, California.

Johnson, C.D. (1979). CEDAR: An approach to the computer automation of short-period local seismic networks, Ph.D. thesis, Seismological Laboratory, California Institute of Technology, Pasadena, California.

Kanamori, H. and D. Hadley (1975). Crustal structure and temporal velocity change in southern California, Pageoph. 113, 257-280.

Kanamori, H., J.B. Minster and K. McNally (1979). Seismological research related to earthquake prediction and hazard reduction, final report, USGS Contract No. 14-08-0001-17631.

Press, F. (1956). Velocity of Lg waves in California, Trans. Am. Geophys. Un. 37, 615-618.

Prodehl, C. (1970). Seismic refraction study of crustal structure in the Western United States, Geol. Soc. America Bull. 81, 2629-2645.

Savino, J.M., W.L. Rodi, R.C. Goff, T.H. Jordan, J.H. Alexander, and D.G. Lambert (1977). Inversion of combined geophysical data for determination of structure beneath the Imperial Valley geothermal region, Systems, Science and Software, Inc. Report SSS-R-78-3412.

Thatcher, W. and J. Brune. (1973). Surface waves and crustal structure in the Gulf of California region, Bull. Seismol. Soc. Am. 64, 235-266.

Table 1.

List of events near Bishop, California used in this study. Source parameters are from Caltech-USGS Monthly Preliminary Epicenters catalog.

Event	Date	H <sub>o</sub>	Lat (N)	Long (W)	h(km)	M
1	Nov. 9-1979	17h47mn0.3s	37°32.81	118°59.14	6.0	4.0
2	Nov. 9-1979	17h54mn16.0s	37°36.14	118°57.16	6.0	4.4
3	Jan. 24-1979	21h14mn27.0s	37°31.77	118°36.22	5.2	4.4
4	Oct. 4-1978	17h46mn47.5s	37°32.20	118°36.60	7.5	4.3
5	Sept. 7-1979	9h43mn48.4s	37°38.16	118°54.95	3.5	4.4
6	Sept. 24-1979	13h5mn4.8s	37°38.12	118°55.03	5.0	4.3
7	Sept. 24-1979	14h26mn20.6s	37°41.02	118°47.40	5.0	4.0

Table 2.

Average velocities  $\bar{c} = \sum_{i=1}^n c_i / n$  (km/s) obtained at different periods T (sec.) from the algorithm described in Section III. The same mode identification as in Figure 12 is assumed, with the exception of the dot marked (?) in this figure which is here assumed to belong to mode 3. All the data used in this table at 2.5 sec. period belong thus to the first three highest peaks of UC diagrams.  $c_t$  are the theoretical values for the model derived in Part I from Kanamori and Hadley (1975).

Mode	T	n	$\bar{c}$	$c_t$	$\bar{c} - c_t$	$(\sum_{i=1}^n (c_i - \bar{c})^2 / (n-1))^{1/2}$
1	1.80	3	3.513	3.617	-0.104	0.063
	2.00	4	3.535	3.626	-0.091	0.064
	2.25	4	3.560	3.638	-0.078	0.084
	2.50	4	3.597	3.650	-0.053	0.090
	2.75	4	3.635	3.665	-0.030	0.101
	3.00	4	3.677	3.681	-0.004	0.097
	3.50	4	3.742	3.721	0.021	0.113
	4.00	2	3.845	3.770	0.075	0.007
2	1.80	7	3.630	3.683	-0.053	0.036
	2.00	6	3.673	3.713	-0.040	0.045
	2.25	9	3.731	3.754	-0.023	0.055
	2.50	9	3.761	3.802	-0.041	0.059
	2.75	9	3.849	3.857	-0.008	0.070
	3.00	8	3.915	3.917	-0.002	0.072
	3.50	6	4.048	4.049	-0.001	0.104
	4.00	5	4.188	4.180	0.008	0.128
3	1.80	4	3.820	3.810	0.010	0.107
	2.00	5	3.886	3.869	0.017	0.134
	2.25	5	3.966	3.953	0.013	0.153
	2.50	5	4.062	4.045	0.017	0.166
	2.75	3	4.093	4.143	-0.050	0.147
	3.00	2	4.090	4.238	-0.148	0.042
	~ 50	2	4.275	4.449	-0.174	0.035
4	1.80	2	3.990	3.987	0.030	0.014
	2.00	2	4.070	4.080	-0.010	0.014
	2.25	2	4.190	4.207	-0.017	0.000
	2.50	2	4.340	4.333	0.007	0.014

Table 3

Events S1 and S2 used in Section V of this study. Source parameters are from Jerry Eaton (personal communication).

Event	Date	$H_o$	Lat (N)	Long (W)	h (km)	M
S1	June 14, 1979	7 <sup>h</sup> 39mn27.85s	35°44.80	118°00.30	7.4	4.5
S2	March 15, 1979	23 <sup>h</sup> 07mn58.11s	34°19.69	116°26.33	3.3	4.8

Figure Captions

Figure 1 Magnification curve of a typical SCARLET/CEDAR seismographic system (station + telemetry + recording system). Period range of interest in this study is shown by dashed lines (1.5 to 5 sec).

Figure 2 Southern California tectonic regions (a) (after Allen et al., 1965) and locations of two profiles of SCARLET/CEDAR stations used as example in this study (b), for event 1 (Table 1). Arrows indicate the maximum range in azimuth of profile 1 and 2.

Figure 3 UC diagram (see Part I) at 2.5 sec period of pure seismic noise records. Solid dots show the location of theoretical UC coordinates predicted by the model derived in Part I from Kanamori and Hadley (1975). (Also see Table 2). Contour spacing = 10% of the maximum amplitude.

Figure 4 Synthetic Lg plus noise records ( $S/N = 2$ ) after deconvolution.

Figure 5 UC diagrams obtained by stacking the records shown in Figure 4. See caption for Figure 3.

Figure 6 UC diagram as in Figure 5 but for  $S/N = 0.5$ .

Figure 7 Example of vertical component records, including Lg, on profile 2 from SCARLET/CEDAR system after low-pass filtering (flat response for frequencies smaller than 0.5Hz, and linear decrease to zero between 0.5 and 2 Hz).

Figure 8 Lg records shown in Figure 7, after deconvolution.

Figure 9 UC diagram obtained by stacking the records of Figure 8 (profile 2, event 1). See caption for Figure 3. Arrows indicate the peak which is closest to theoretical UC coordinates.

Figure 10 Same as Figure 9 but for profile 1.

Figure 11 Phase velocities obtained through the algorithm described in the text for event 1 and profiles 1 and 2. The solid lines are theoretical values computed for the Rayleigh wave model of Hadley and Kanamori (1979).

Figure 12 Phase velocities of the first three highest peaks on 2.5 sec period UC diagrams ( $U > 3.2$  km/sec) for 9 profiles running east and west of the Salton Trough (profiles 1 and 2 are indicated by arrows). Dotted lines join the points assumed to belong to the same mode. For profile 2, the fourth peak is also shown because the third peak (marked "?") is not identified as a mode on Figure 9. Horizontal lines are theoretical values given in Table 2.

Figure 13 Simplified geological map showing Sierra Nevada profiles. Stations used in connection with source S1 (S2) are shown by solid (open) circles. (Map after Bateman and Eaton, 1967).

Figure 14 Lg profiles for source S1, after deconvolution.

Figure 15 UC diagram at 2.5 sec period obtained from profile shown on  
Figure 14. Same conventions as Figure 3. A, B and C represent  
highest peaks on diagram.

Figure 16 Experimental dispersion curves for Sierra Nevada profiles.  
Also shown are theoretical dispersion curves for the crustal  
models shown in insert. Solid lines derived from Carder et al.  
(1970), dashed lines from Hadley and Kanamori (1979), dotted  
lines indicate effect of low velocity surface layer.

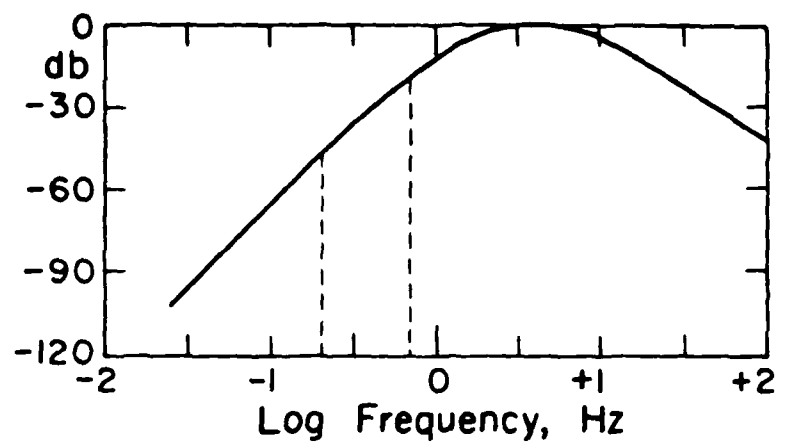


Fig. 1

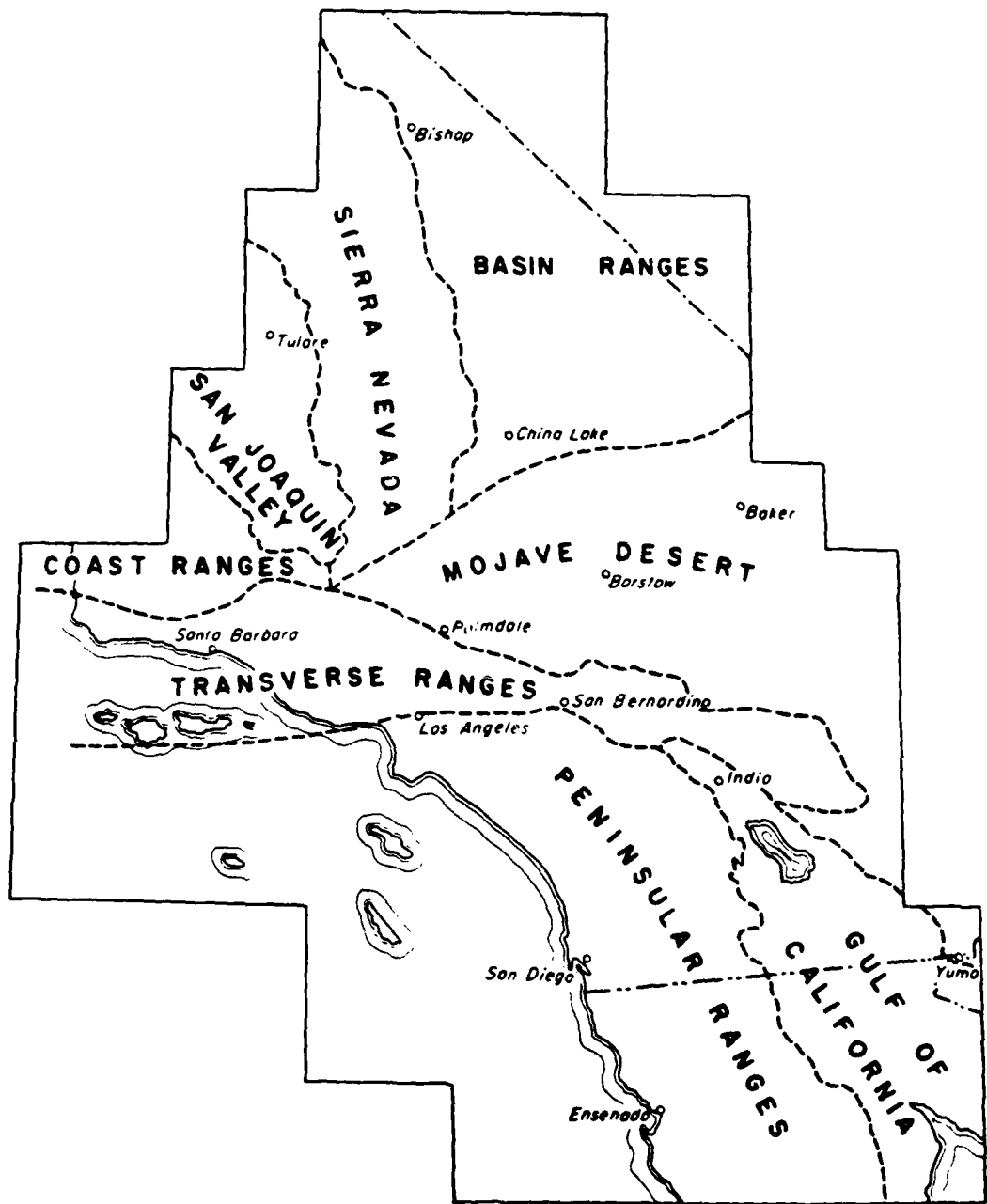


Fig. 2a

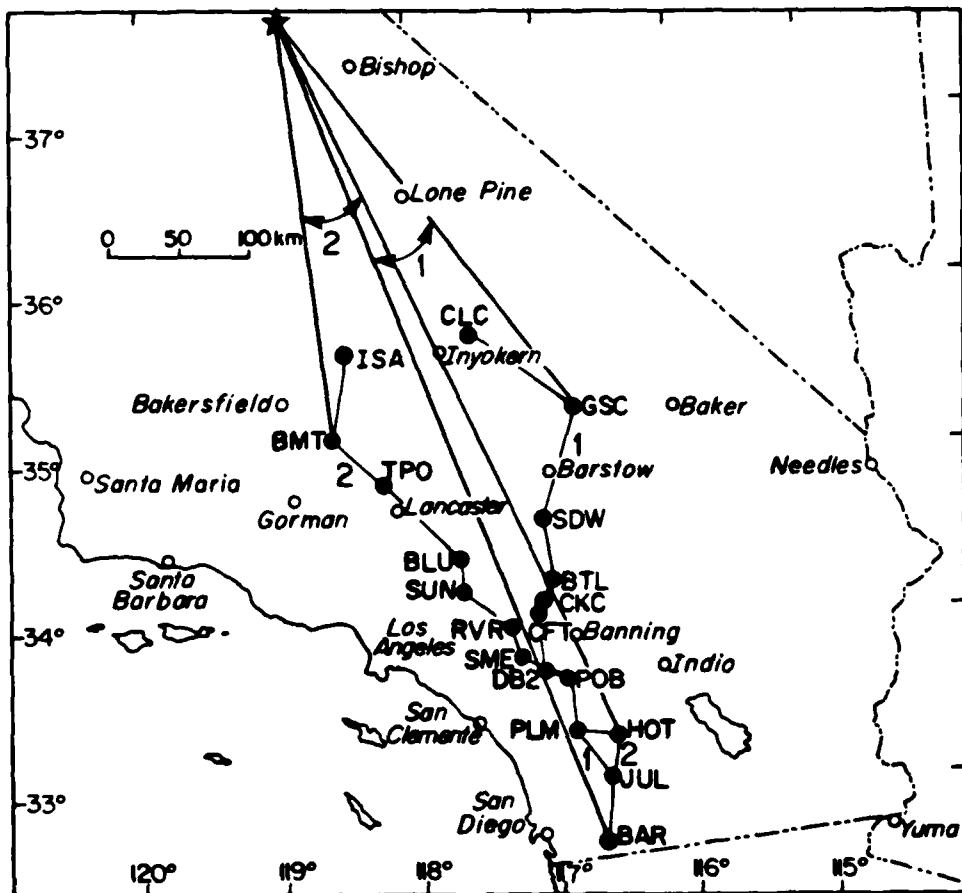


Fig. 2b

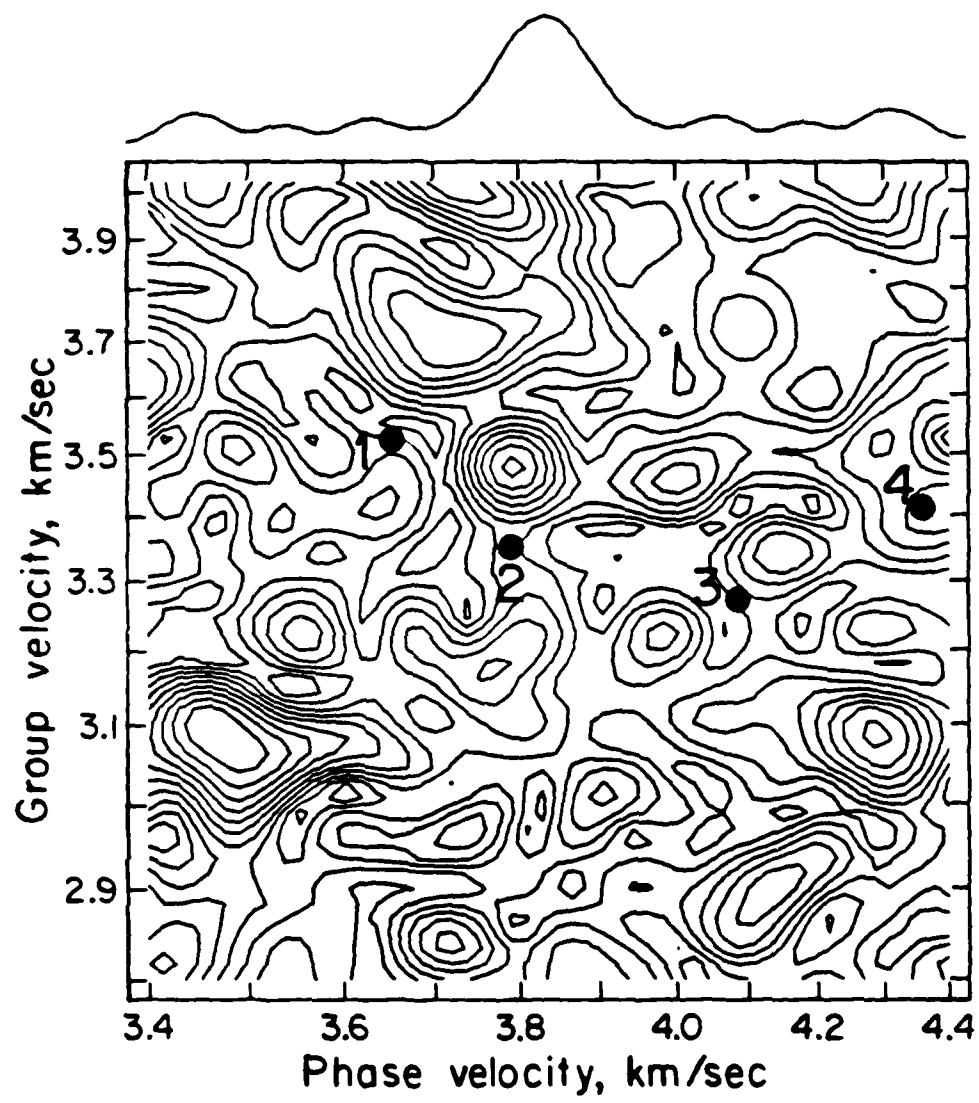


Fig. 3

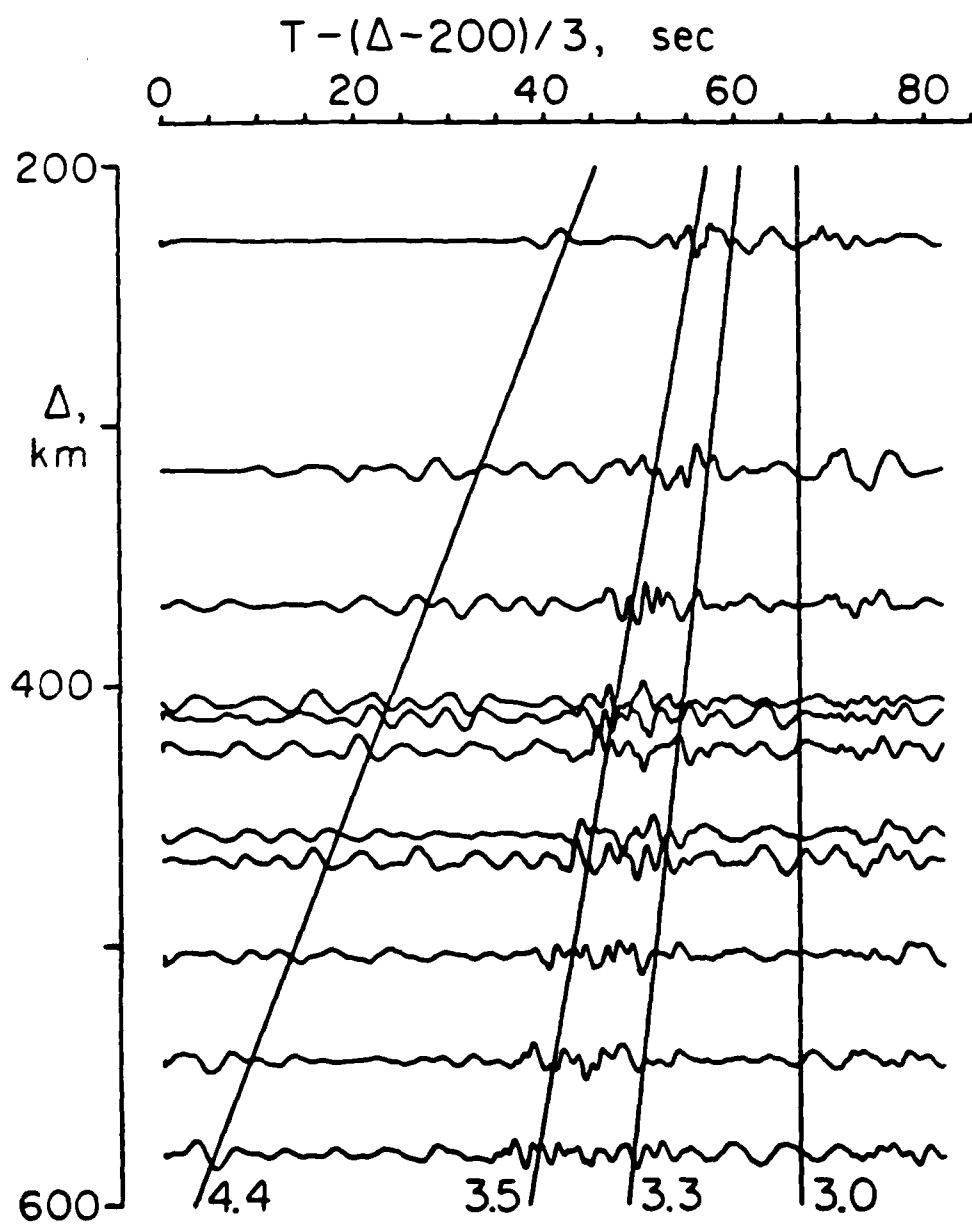


Fig. 4

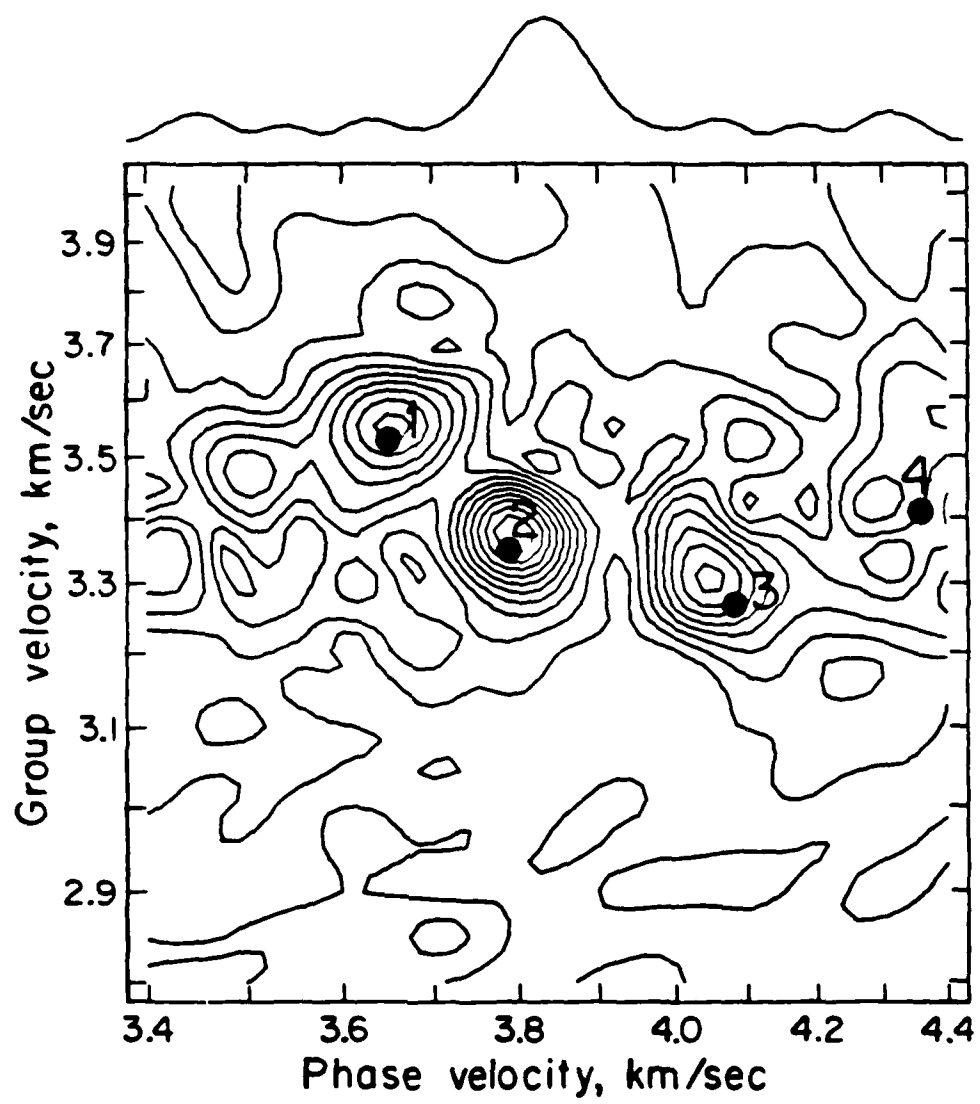


Fig. 5

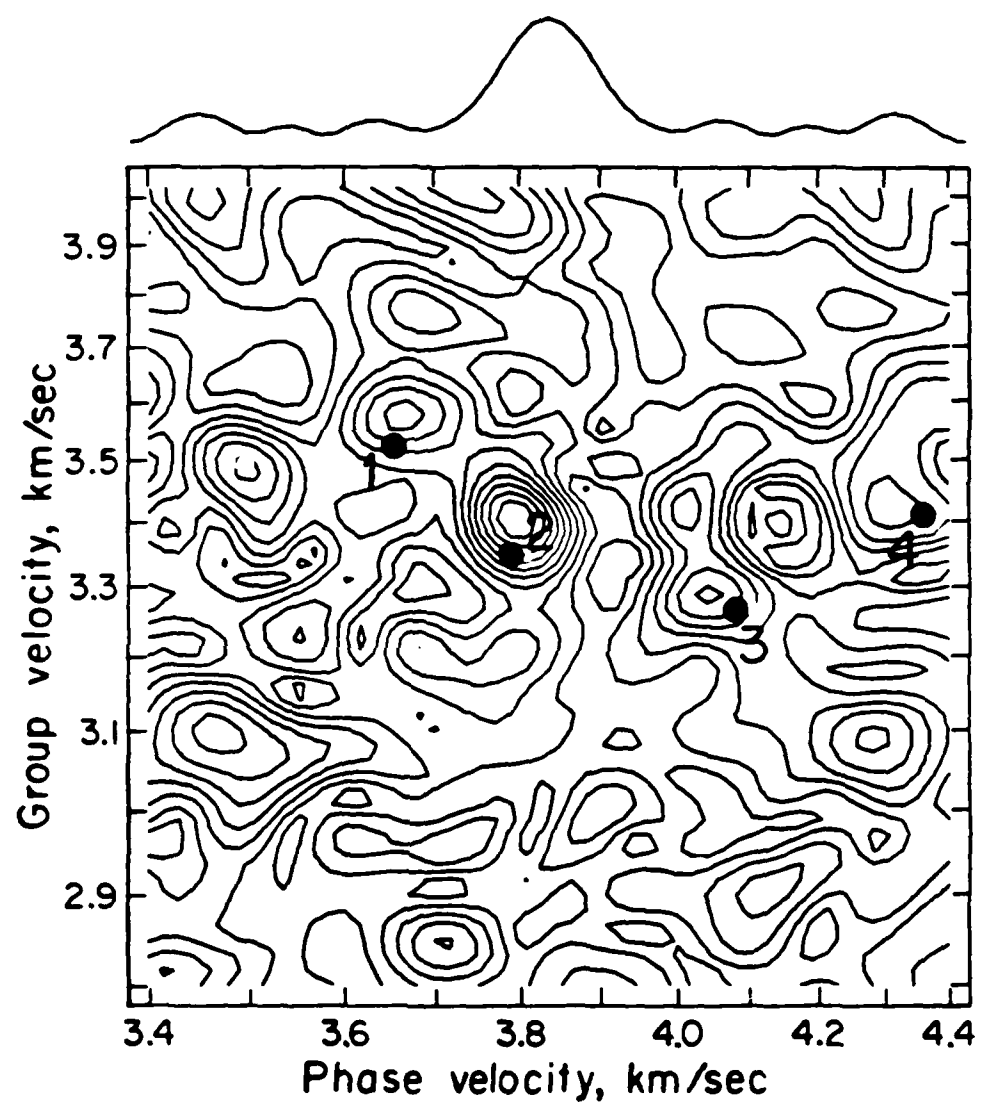


Fig. 6

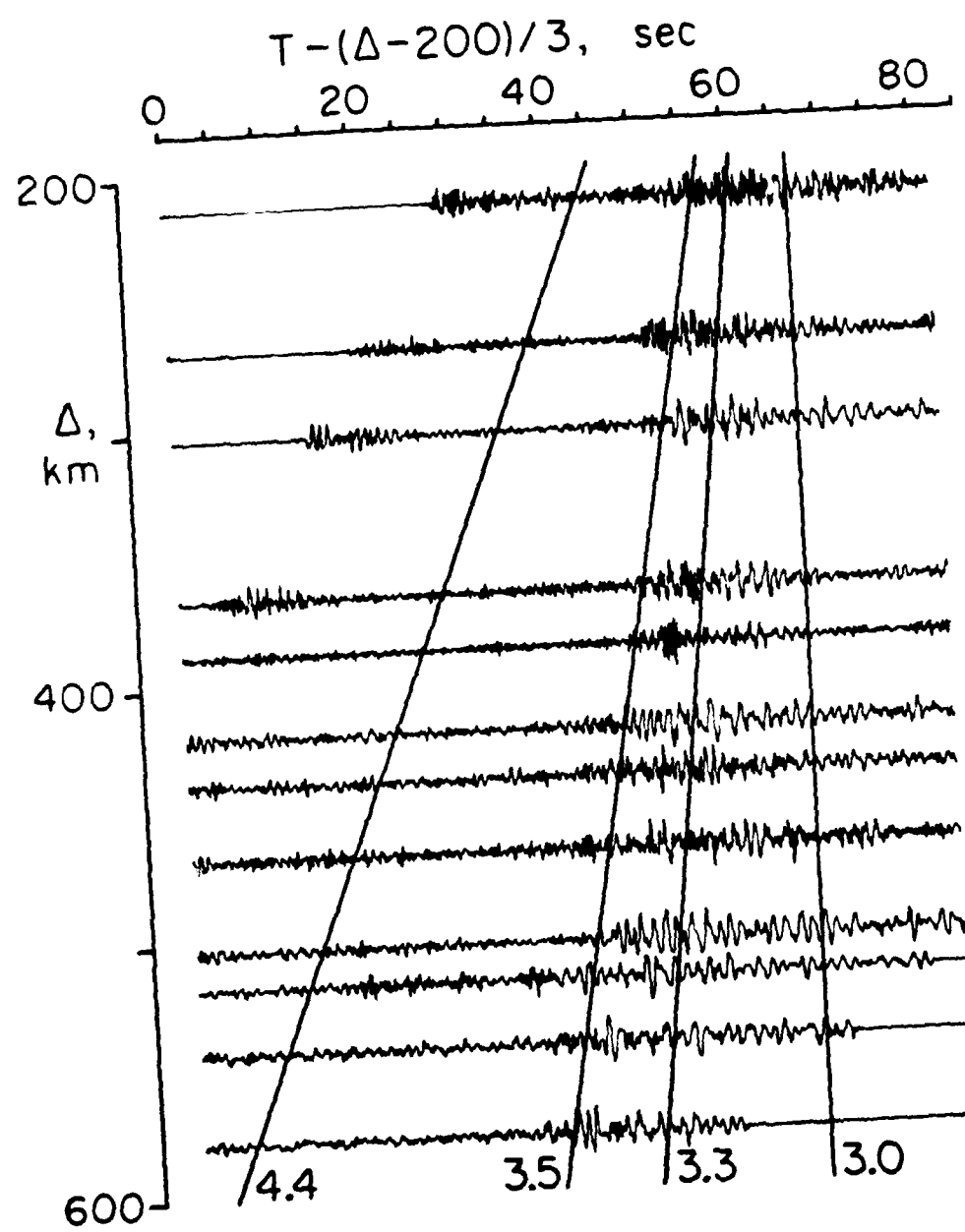


Fig. 7

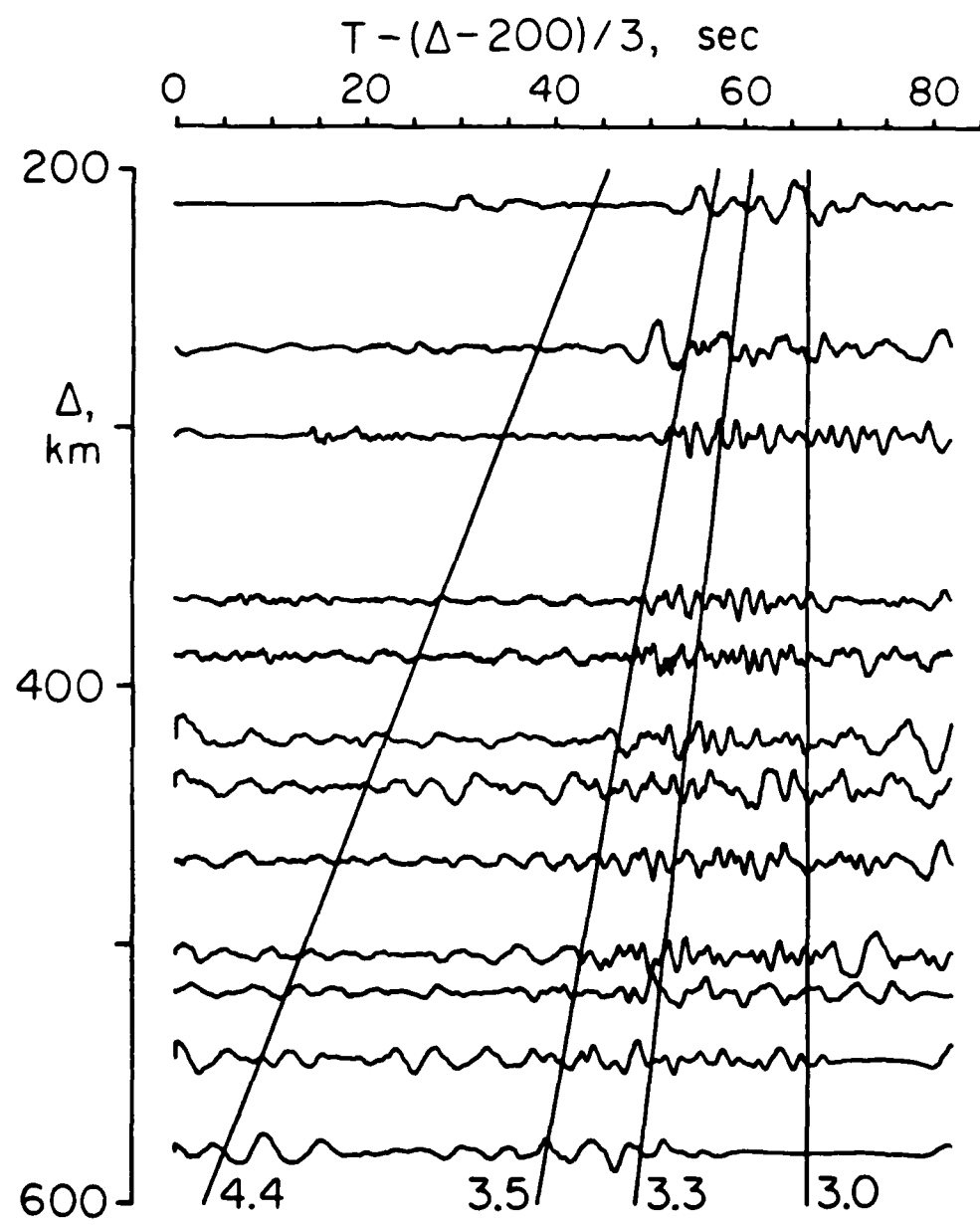


Fig. 8

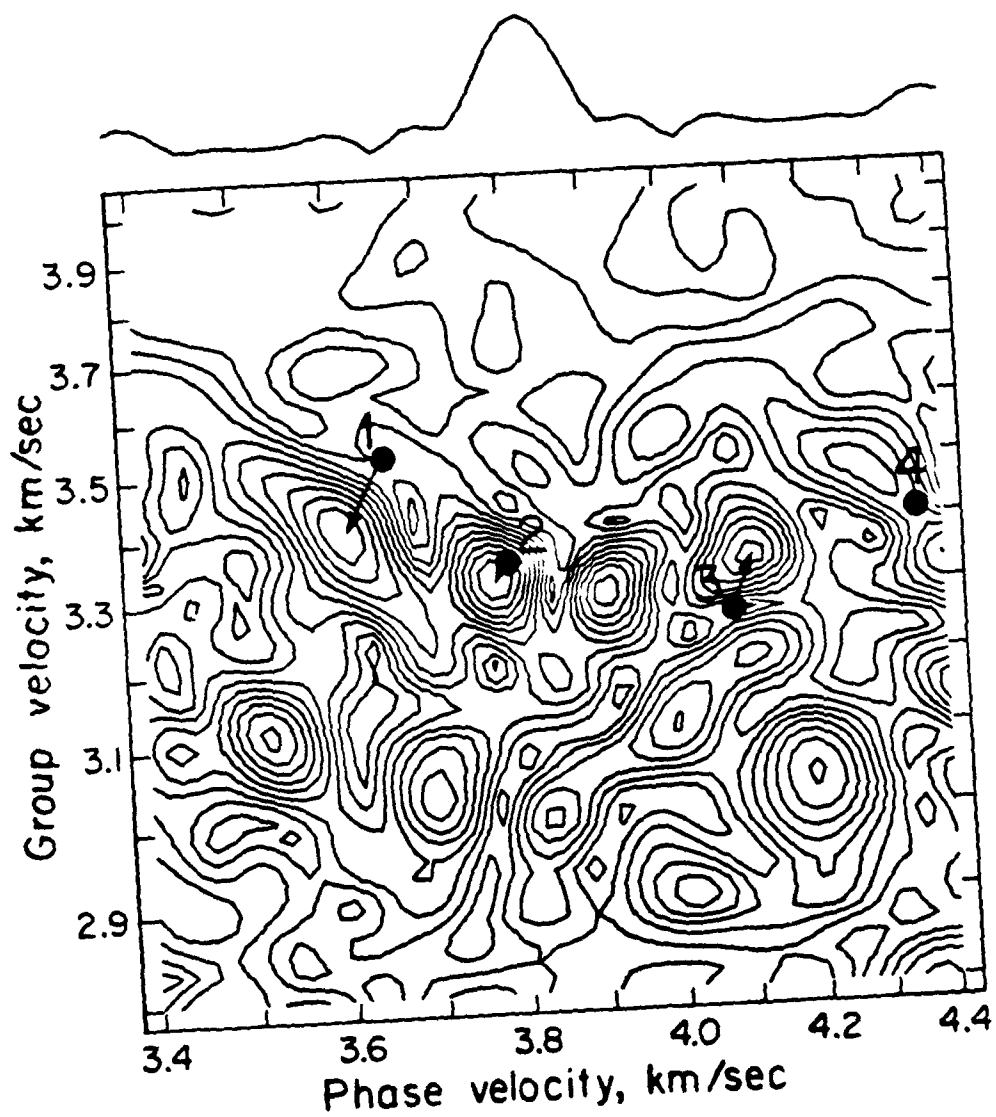


Fig. 9

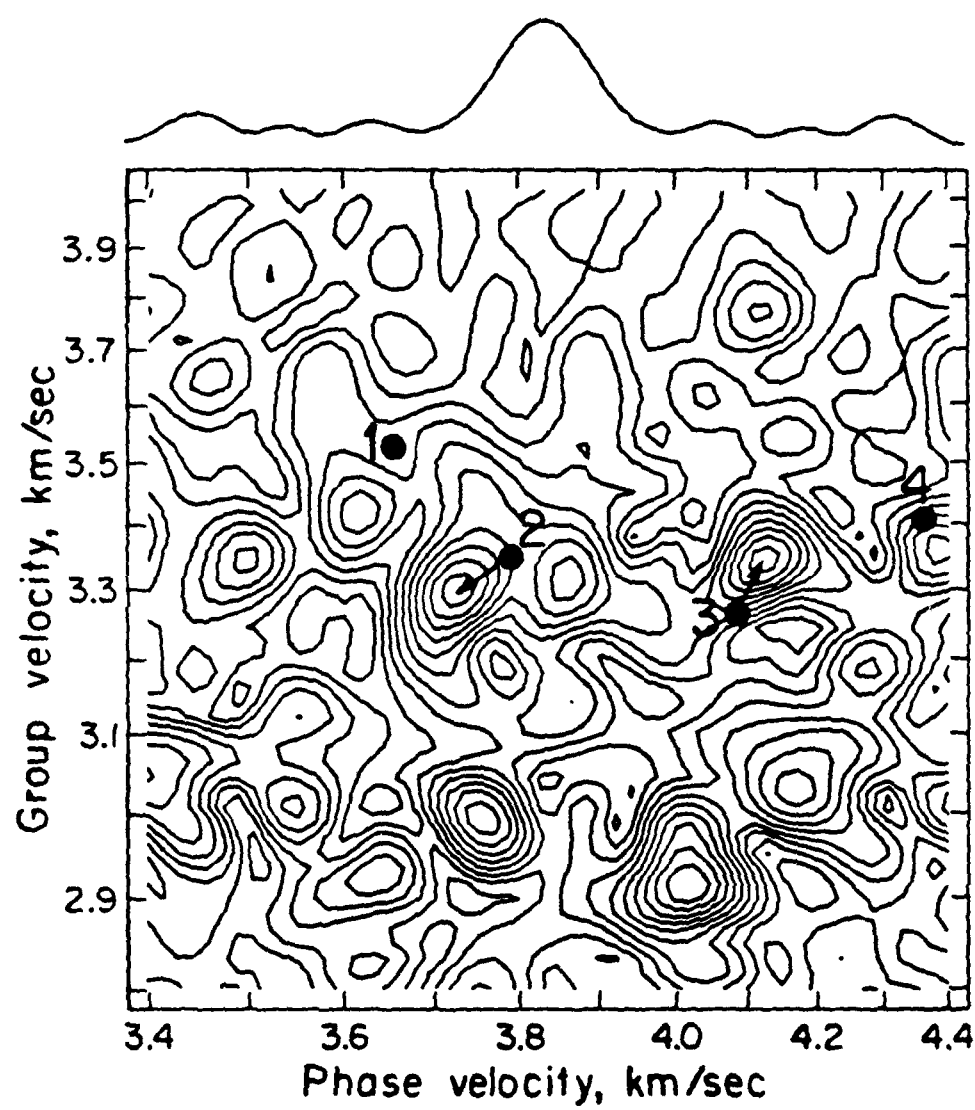


Fig. 10

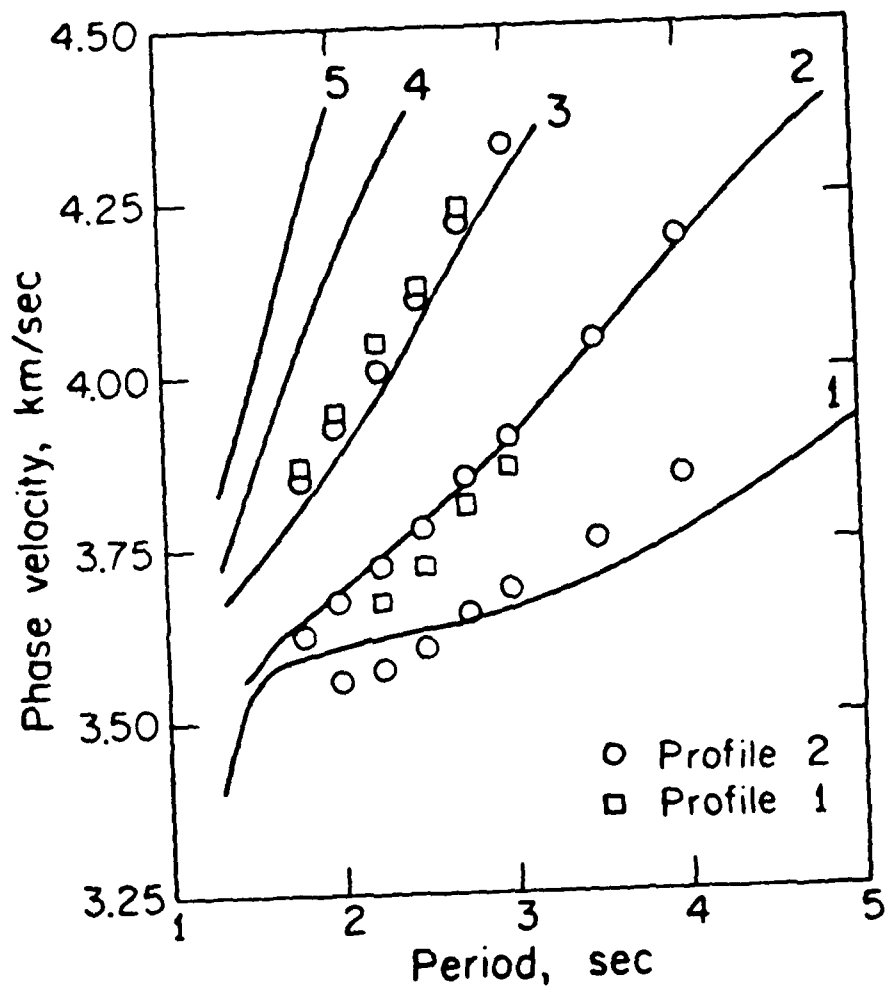


Fig. 11

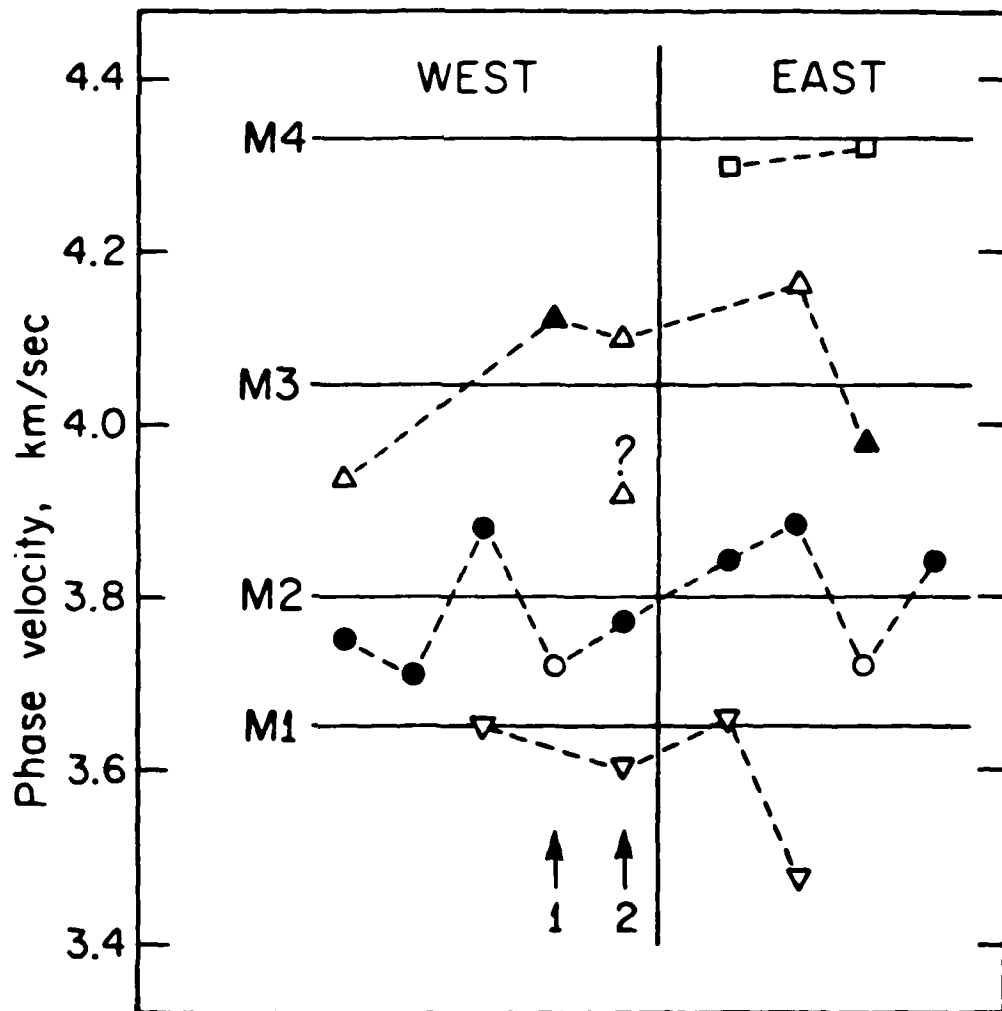


Fig. 12

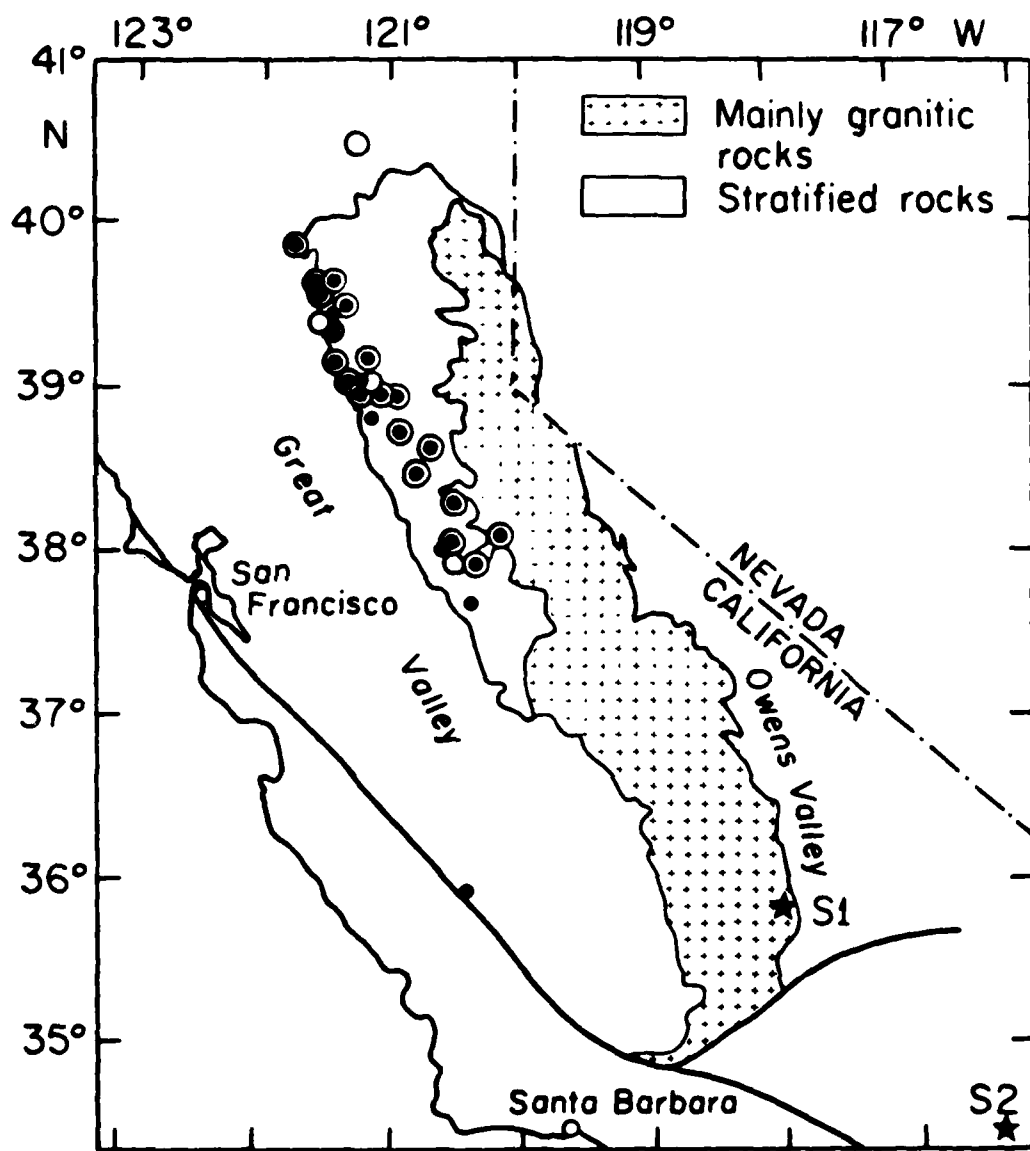


Fig. 13

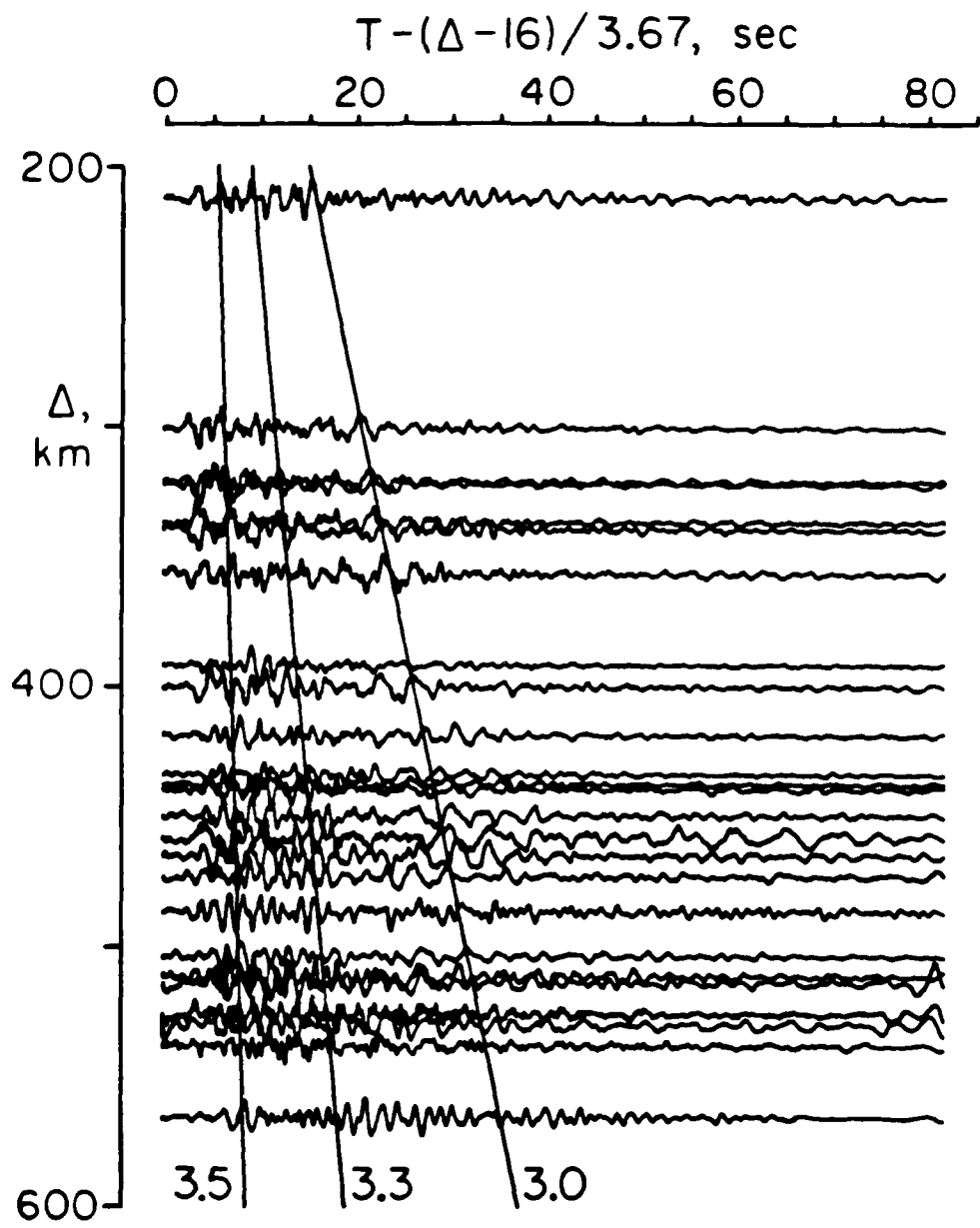


Fig. 14

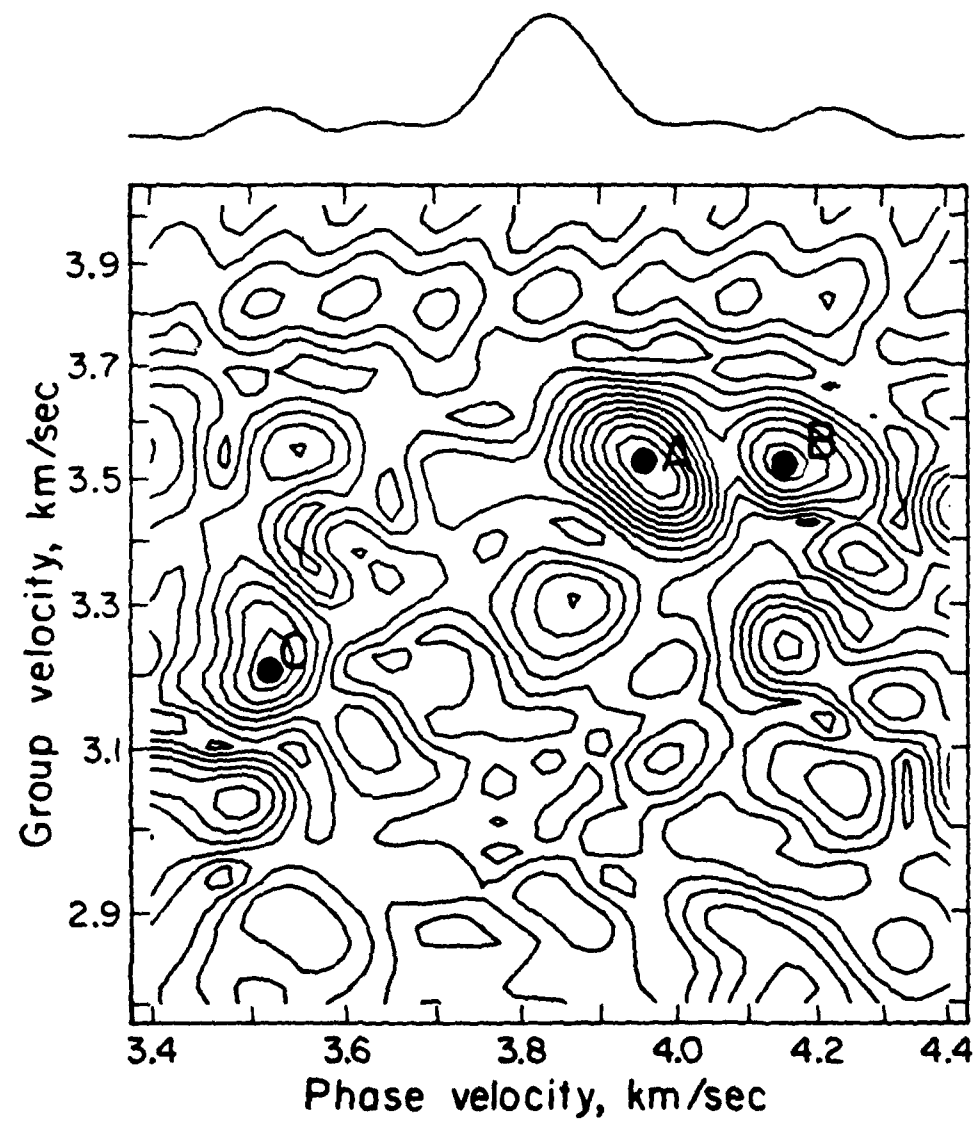


Fig. 15

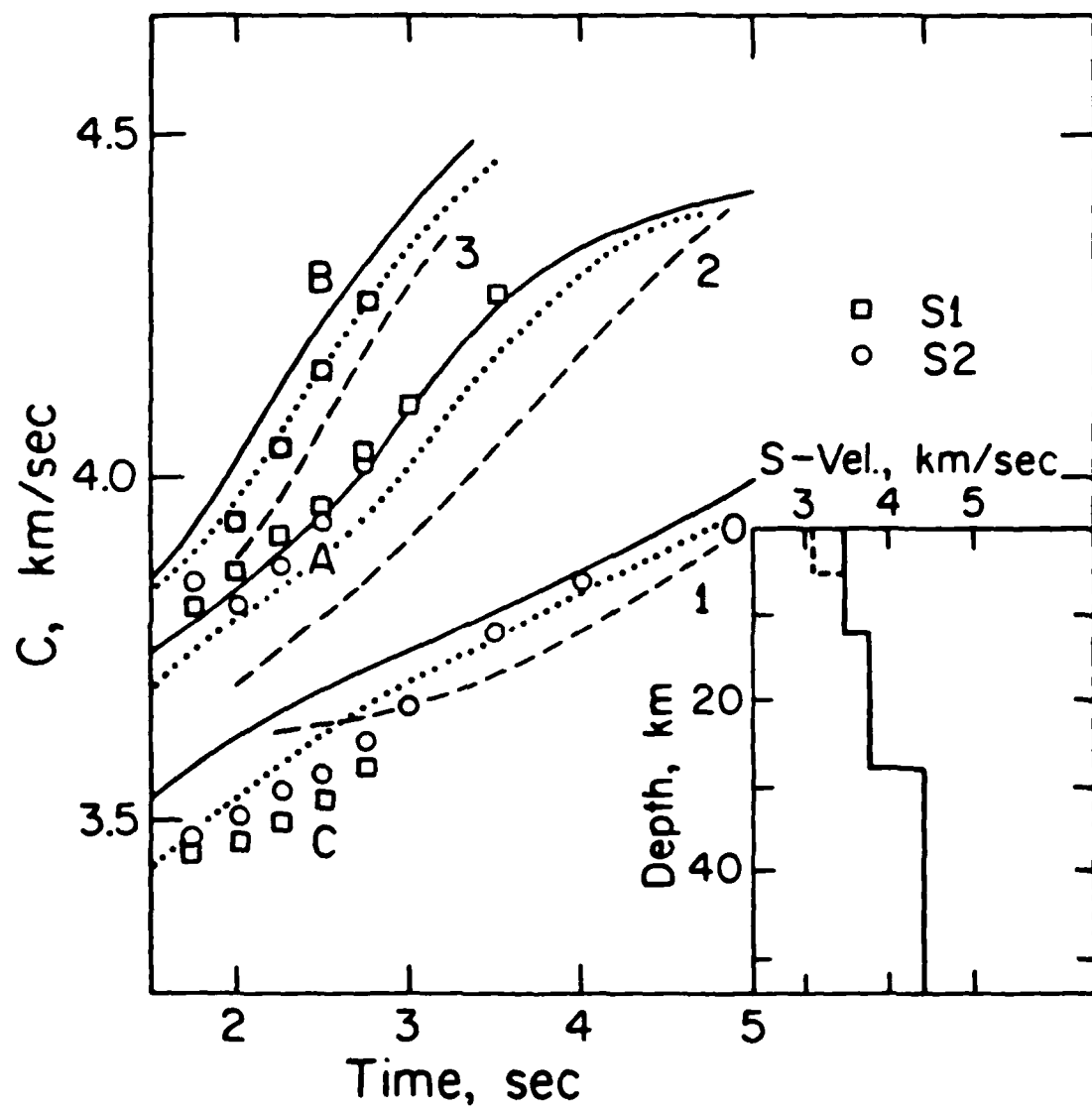


Fig. 16

P-Wave Complexity and Fault Asperities:  
The Borrego Mountain, California, Earthquake of 1968

by

John E. Ebel\*

and

Donald V. Helmberger

(October 9, 1980)

Revised August 19, 1981

Revised September 15, 1981

\*Now at Western Observatory, Department of Geology and Geophysics,  
Boston College, Weston, MA 02193

## ABSTRACT

Results from a synthetic seismogram analysis of the short-period P waves from the Borrego Mountain earthquake of April 9, 1968 ( $M_L = 6.4$ ) are used to model the strong motion recording at El Centro. A short-period-long-period deconvolution analysis of the teleseismic P waves suggested that a two source model would fit the data much better than the single source model presented by Burdick and Mellman (1976). Forward and inverse modeling of the data demonstrated that two sources, each of less than 2 sec duration, the second occurring 2.2 sec after the first and both being at about 8 km depth, best fit the short-period waveforms. From this model long-period synthetics were generated which were found to be quite compatible with the data. This source model was also used to synthesize the strong-motion SH displacement, velocity and acceleration records from El Centro, California. The close match of synthetics and data is used to argue that short-period waveforms contain much information about asperities which play a crucial role in the near-source strong motions from an earthquake. The Borrego Mountain event probably began with the failure of a fault asperity. The evidence for this is the several-hundred-bars stress drops of the two short-period sources and the probable location of these sources in a place where there was almost no aftershock activity or post-seismic creep on the fault.

## INTRODUCTION

Time domain modeling of long-period, far-field body waveforms has proven to be a very effective tool for determining source parameters of earthquakes (Helmberger and Burdick, 1979). The power behind the technique lies in the fact that synthetic seismogram methods can correctly account for free surface effects along with near-source and near-receiver reverberations which can complicate far-field seismograms, especially those from shallow-focus events (Langston and Helmberger, 1975; Langston, 1978). While time domain studies of long-period waveforms of moderately large, shallow-focus earthquakes have become quite popular, only a few investigators have attempted to model shorter period recordings (such as WWSSN short-period records) of events of comparable size (Bache *et al.*, 1980; Cipar, 1980; Hartzell, 1980). The reason for this is simple; long-period seismograms contain much less detailed information about the fault time history and the seismic structure along the source to receiver travel path than short-period records and consequently are much easier to model. However, the short-period records are of interest precisely because they contain a more detailed look at the earthquake source process. Thus, in-depth modeling of short-period body-wave data is a useful step toward understanding seismic sources.

The Borrego Mountain, California earthquake of April 9, 1968 ( $M_L = 6.4$ ; see Figure 1) is particularly well-suited for a short-period body wave study because it is an event for which there have been time domain studies of both the long-period body waves (Burdick and Mellman, 1976)

and the strong-motion data (Heaton, 1977; Heaton and Helmberger, 1977). In addition, the surface rupture for the event was mapped in detail (Clark, 1972; Burford, 1972), aftershock locations and focal mechanisms have been determined (Allen and Nordquist, 1972; Hamilton, 1972) and a seismic crustal structure for the source has been found (Hamilton, 1970). This wealth of information simplifies the task of modeling the short-period body waves because it provides constraints upon the types of models which can be deemed acceptable. The philosophy used in this study was to try to find a source model for the teleseismic short-period data which was consistent with both the far-field long-period and strong motion recordings of the event from El Centro, California.

#### THE DATA SET

The short-period P waves recorded at all of the stations located between  $30^{\circ}$  and  $90^{\circ}$  from the source are shown in Figure 2, and information on the station locations relative to the source region are given in Table 1. At first glance the waveforms appear rather complicated. The background noise on most of the records obscures the first arrival sufficiently that the initial polarities cannot be read with any certainty, and at some stations (particularly in South America) there are many seconds of high amplitude ringing after the first arrival which may be indicative of contamination from the local receiver structures. At other stations (especially those in eastern North America and some in Europe) the seismograms are characterized by a few seconds of high amplitude arrivals followed by a low amplitude coda.

Even with these major differences in the waveforms for stations at different directions from the epicenter there is much coherence in the waveforms between stations at similar azimuths. In particular, the waveforms recorded at stations to the southeast of the source region (NNA, ARE, PEL, CAR and TRN) are very similar for the first ten seconds or so. This is likewise true of stations to the north (NOR, GDH, ESK, KTG, KBS, KEV, KON, UME and NUR) and stations to the northeast (STU, VAL, SCP, GEO and even NAT which lies somewhat southeast of the source). The similarity of the waveforms at these different stations is strong evidence that the recorded signals are dominated by information from the near-source region.

The first step taken in analyzing the data was to check the compatibility of the short-period and long-period records. This was done by using the simultaneous deconvolution procedure outlined by Burdick (1977). The technique involves passing the data through a Gaussian filter, dividing instrument and Futterman attenuation operators from the long-period and short-period records from a station separately, and then adding together the spectra of the two deconvolved ground motions from the different frequency bands. The information in the crossband of .125 Hz to .5 Hz where the responses of the two instruments overlap is averaged and the total response is then transformed to the time domain to get the broad-band ground motion. As a check on the stability of the procedure, the responses of the different instruments are reconvolved with the attenuation operator and the deconvolved ground motion and the results are compared to the original, filtered

seismograms. If there is a mismatch in the relative timing or the relative amplitudes of the two records, if the signal-to-noise ratio is poor or if there are inaccuracies in the digitization of the records, the deconvolved traces may not match the initial, filtered traces very well. In these cases the amplitudes and timing of the data can be redetermined and the deconvolutions recomputed.

Simultaneous deconvolutions for the eight stations which had the best recordings on both long-period and short-period seismograms are shown in Figure 3 along with the filtered original and the deconvolved traces. A  $t^*$  of 1.0 and a width of 1.0 seconds at the half-maximum amplitude were used in the attenuation operator and the Gaussian filter respectively. The quality of the deconvolutions ranges from very good at ARE and MAT to very poor at STU even after the timing and amplitudes of the original records had been checked and rechecked. The problems with the quality of the results notwithstanding, there appear to some similarities among all of the deconvolutions. At all of the stations the largest arrival occurs several seconds after the beginning of the P wave coda. On many of the waveforms (especially those from which the best deconvolutions were obtained) this largest arrival is made up two distinct pulses, both of which have the same polarity. The total duration of these two pulses is between 2 and 5 seconds at most of the stations. Based upon their analysis of the long-period P waves Burdick and Mellman (1976) have identified this arrival as the sP phase from the source region. The double-arrival nature of the sP phase evident in the simultaneous deconvolutions probably also had its origins in the

near-source region. It was not due to receiver reverberations because it appears at different stations with undoubtedly dissimilar receiver crustal structures. This means that it must have been caused by either near-source reverberations or by two distant seismic sources which took place within a couple of seconds of each other.

A number of unusual features of the data set are obvious from the simultaneous deconvolutions. One is that the time difference between the arrival time of the sP pulse and the initial P phase is about 2 seconds greater at MAT than at any other station with the possible exception of COL. Since source directivity affects the shape of the time functions of different phases much more than their relative arrival times, the similarity of the sP phase at MAT and ARE (stations at well-separated azimuths) implies that this discrepancy cannot be attributed to source directivity. One possible explanation for this observation is that a laterally-varying near-source surface structure such as a localized deep sedimentary basin northwest of the epicenter could have delayed the sP phase. However, this idea is difficult to reconcile with the fact that the area on the earth's surface where sP for MAT reflected was in the vicinity of Borrego Mountain where the seismic velocities are faster than the local average (Hamilton, 1970). Thus, while this sP arrival time problem has no satisfactory explanation, it does adversely affect the fit of the long-period synthetic to the observation at MAT (the first swing of the Burdick and Mellman (1976) synthetic at MAT is shorter period than that of the observation) as well as the match of the short-period synthetics and

observations in this study.

A second unusual feature of the data is evident in the long-period and short-period records from BOG. The sP arrival on the long-period record from this station is approximately 13 times larger than the amplitude of the direct P wave, while on the short-period record the P and sP phases are about the same size. The reconvolutions of the long-period and short-period data match the initial seismograms closely which means that there was almost no mismatch of information between the waveforms digitized from the two different records. Since the focal mechanism for this event indicates that the P arrival should be nodal at this station, the amplitude of the first arrival on the short-period record appears to be anomalously large. This high frequency, high amplitude P arrival was probably due either to a rotation in the orientation of the fault plane which radiated the initial short-period energy relative to that for the long-period energy or to some sort of diffraction around the southern end of the fault which would occur if the seismic velocities to the west of the fault are higher than those to the east. Hamilton (1970) found some evidence that a velocity contrast does exist across the fault in the Borrego Mountain epicentral region although he does not quantify what this contrast might be or to what depth it may extend. If there is a velocity difference in the basement rock across the fault which affected the apparent short-period radiation pattern, it must be confined to the upper crust since the long-period P and sP radiation do not have anomalous relative amplitudes. On the other hand, if the amplitude discrepancy was caused by different focal

mechanisms at short and long-periods, it should be evident from the modeling of the short-period records. Unfortunately, the short-period observations were not of high enough quality to resolve any short-period-long-period radiation pattern differences. Therefore, a strong argument for the cause of the anomalously high amplitude short-period P wave at BOG cannot be made with the data set at hand.

A third problem in the data set is that there is an unusual pattern of waveforms recorded at SCP and STU. These stations are at similar azimuths from the source region, but STU is more than twice as far away as SCP. The short-period waveforms recorded at these two stations are virtually identical, but the STU long-period record is an upside-down version of that from SCP. While a poor but acceptable deconvolution was found for SCP (one which was very similar to the good deconvolution found by Burdick and Mellman (1976) for WES, a station a few hundred kilometers north of SCP), a satisfactory deconvolution could not be found for STU. The polarities of the short-period instruments at STU and SCP were checked using first arrivals from nuclear tests and nothing unusual was found. Certainly the waveform differences between STU and SCP would not be unexpected if the short-period and long-period radiation had different focal mechanisms. However, the apparent mismatch of the short-period and long-period waveforms recorded at STU casts doubt upon the reliability of the data from that station. Thus it is not possible to ascribe the cause of the differences in the seismograms from SCP and STU to effects located in the source region of the earthquake.

#### SHORT PERIOD MODELING

The short-period body waves from the earthquake were modeled using the time-domain synthetic seismogram method of Langston and Helmberger (1975). Synthetic seismograms for the short-period P waves were generated by computing the response of a layered earth to one or more point sources and convolving it with a trapezoidal time function for each point source, a Futterman (1962) attenuation operator with a  $t^*$  of 1.0 (unless other noted) and a WWSSN short-period instrument response. The parameterization of the time functions was the same as that of Helmberger and Malone (1975) where the rise, top and fall times of the trapezoid are designated as  $\delta t_1$ ,  $\delta t_2$  and  $\delta t_3$  respectively. The time functions for all P and S rays which took off from a particular source were assumed to be identical, and the interaction of the incident arrivals with the near-receiver structure was not included in the models since the receiver structures for the stations used are not known.

The first step taken in analyzing the short-period P records was to generate synthetics using the strike-slip source model found by Burdick and Mellman (1976) from studying the long-period body waves (Table 3). The earth response used for these synthetics was computed using the direct P wave and the surface reflections pP and sP in the crustal model of Hamilton (1970) which is summarized in Table 2. These synthetics are compared to the observed data in Figure 4. It is obvious that while the synthetic waveshapes do not match the observations well at all, there are several aspects of the synthetics which bear some resemblance to the

data. In particular, the ratio of the amplitude of the initial arrival to the highest amplitude swing of the synthetics is approximately that of the data at many of the stations (i.e. ARE, TRN, SCP and KIP). Also, the arrival time of this large pulse with respect to the start of the waveshape on the synthetics appears to be close to that of the data at stations where the first arrival can be isolated from the noise (ARE, SCP, TRN and PEL are examples). The similarities between the synthetics and data suggest that the focal mechanism and source depth found by Burdick and Mellman (1976) are consistent with the short-period observations. The discrepancies between the synthetics and data, in particular the fact that the synthetics lack some of the high frequency nature of the observations, is evidence that the source time function of Burdick and Mellman (1976) is not entirely appropriate at shorter periods.

On all of the synthetics from the Burdick-Mellman model (Figure 3) the large arrival which occurs several seconds into the waveforms is the sP phase, and from the simultaneous deconvolution analysis it was evident that there were two separate pulses which contributed to making up the sP phase. This suggested that more than one source was needed to model the short-period records. Several different sets of synthetics computed with two point sources were found to give a fit which was much better than that from the single point-source model of Burdick and Mellman (1976). With the two-source models the fit of the synthetic P arrival to that of the data at most stations was still not very good, but this is not surprising since the signal-to-noise ratio is generally

poor for this part of the record. However, the similarity of the synthetic sP phase to that of the data was improved for most of the records. The synthetics generally fit the data quite well at stations in Europe (with the exception of STU which was found to be a questionable station in the deconvolution analysis) and eastern North America, but for the South America stations they lacked some of the high frequency characteristics of the data.

#### INVERSION MODELS

An effort was made to improve the fit of the synthetics to the short-period data and to explore the uniqueness of the source models by employing the waveform inversion technique used by Burdick and Mellman (1976) to model the long-period body wave records. The procedure involves computing changes in the source model based upon cross-correlations of the synthetic and observed waveforms at each station. In practice the inversion program was allowed to iterate a number of times on the source model until it could no longer improve the cross-correlations. For the Borrego Mountain data set the only rays used in the inversion process were the same three as those used in the initial forward modeling. The only short-period waveforms that were used were those where the signal-to-background-noise ratio was large and where it was felt that there was the least contamination by receiver reverberations. Since each station was given a weighting, stations with waveforms of questionable quality could be deemphasized in the inversion process so that they did not contribute very much to the final model.

which the program found.

The parameters which were allowed to vary in the inversion runs were the three parts of the trapezoidal time function, the focal mechanism and depth of each of the two sources and the time lag of the second source with respect to the first. The program was first used on a data set of six short-period records (STU, ARE, BOG, KON, ARE and SCP) using the starting model listed in Table 3. The final model from this inversion is given as the short-period inversion model in Table 3 and synthetics for all of the short-period records are shown in Figure 5. A comparison of the cross-correlation values between the final and the starting model reveals that the inversion procedure improved the fit by about 10% at each station. The inversion made only minor alterations in the parameters for the first source, but it made rather substantial changes in the focal mechanism and time function of the second source. The result of these changes was to make the second source have a focal mechanism with the approximate strike of  $193^{\circ}$  but with a time function very different from those of the first source. The inversion program left both sources at depths of about 8 km. Long period synthetics were also computed using this model and they are shown in Figure 6. In general they fit the observations reasonably well.

The inversion process was also performed on a data set which included all the seismograms used in the short-period inversion plus records from 17 long-period stations used by Burdick and Mellman (1976). Once again, focal mechanisms, depths, time functions and relative time of the events were freed in the inversion program, and the starting

model was the same as that used for the inversion of the short period data set. The source models which resulted from the inversion of this data set are given as the simultaneous inversion model in Table 3 and the synthetics are shown in Figures 7 and 8. The cross-correlations were once again improved by about 10% at each station. Here also the inversion program changed the parameters of the second source much more than those of the first and the final models for the two sources are similar to those found from the short-period inversion except for the shape of the time function and the strike of the second source. This simultaneous inversion demonstrates that the two source model which is necessary to fit the short-period data is also quite compatible with the long-period waveforms. The difference in the time functions of the second source found from inverting the two different data sets also gives a good feeling for the resolution of the modeling process. From comparing the models in Table 3, it appears that the methods used here are much more capable of determining the source parameters for the larger, first source than for the smaller, second source. Nevertheless, many parameters of the two sources are well determined from the modeling. The first source was at about 8 km depth, had a duration of about 2.2 seconds and had a strike, dip and rake of  $-43^\circ$ ,  $78^\circ$  and  $178^\circ$  respectively. The second source took place about 2.2 seconds after the first, was only about a third of the amplitude of the first, was located at a depth of about 8.5 km and had a strike, dip and rake of  $-38^\circ$ ,  $68^\circ$  and  $194^\circ$ .

None of the inversion runs on either of the two data sets was able

to resolve the simultaneous waveform problems found at BOG and STU, nor were they able to find a model which satisfactorily fit the waveforms at MAT. In fact, there are noticeable differences between all of the short-period synthetics and data in Figures 5 and 7. While this is not surprising because of the low signal-to-noise ratio for the data set, it does make it difficult to judge how well the synthetics model the data. A better feeling for the quality of the fits can be obtained by considering how well the deconvolved waveforms can be matched. Synthetics which have been computed without either instrument response or attenuation are compared in Figure 9 to the results of the simultaneous deconvolution analysis presented in Figure 3. The model used for the synthetics in Figure 9 was that found from the simultaneous inversion modeling. In general the fit is very good at ARE and NNA, and, except for a somewhat strong synthetic pP phase at BOG and SCP, the synthetics match the data at these stations also. The deconvolved synthetic at MAT was found to match the data best if the synthetic sP phase was aligned with the arrival which was identified as the sP phase in the data, and so this is the way that the comparison at MAT is plotted in Figure 9. Because of this, the first arrivals of the synthetic and observation do not coincide. The fits at COL, STU and NUR are poor, but this is not surprising since good deconvolutions at STU and COL could not be obtained and the signal-to-noise ratio was very low for the data from NUR. The deconvolution synthetics show that, while the theoretical time functions lack some of the details of the data (especially the long-period information), the source model is a reasonable

interpretation of the data.

The inversion modeling was all done assuming that the short-period records could be closely modeled using only the direct P wave and the P and SV free-surface reflections. This assumption was justified by comparing synthetics computed from these three rays with those calculated from a full crustal response. The similarity of the synthetics computed from these two methods is demonstrated in Figure 10. The source parameters used for both synthetics were those found from the simultaneous inversion modeling, and the full crustal response synthetics were calculated using Fuchs (1966) modification of the Thomsen-Haskell layer matrix method with the near-source crustal structure being that reported by Hamilton (1970). The two sets of synthetics are very similar for NAT, KON and SCP. For ARE the amplitudes of the peaks and troughs of the two synthetic waveforms are somewhat different while the phases of the two waveforms are quite similar and in fact match the phase of the observation very closely. From these examples it is evident that the waveforms contain much more information about the earthquake source time history than about the near-source structure and that the direct P wave and the free surface reflections are by far the most important phases for determining the shapes of the synthetic waveforms.

Seismic moments for the earthquake were computed from the simultaneous inversion model by averaging the moments calculated from several of the stations. Values for the short-period and long-period moments computed from the simultaneous inversion model for  $t^* = 1.0$  are

given in Table 1 for those stations where moments were determined. The average moments for all the short-period records are  $5.0 \times 10^{25}$  dyne-cm for a  $t^*$  of 1.0 and  $7.7 \times 10^{25}$  dyne-cm for a  $t^*$  of 1.3. The corresponding average moments for the long-period data (excluding STU where the value was found to be clearly inconsistent with the rest of the data) are  $7.6 \times 10^{25}$  dyne-cm and  $8.8 \times 10^{25}$  dyne-cm respectively. The differences between the short-period and long-period moments must be due to the existence of a very long-period part of the time function which was not found during the modeling process. Since the fault length determined from surface cracking and aftershock locations (Clark, 1972) is much larger than that which was estimated from the long-period body wave modeling (Burdick and Mellman, 1976), the existence of a long-period part of the source time history is quite reasonable.

#### STRONG MOTION MODELING

Data from the earthquake was also recorded on a good set of acceleration and Corder displacement seismograms at El Centro, California, located about 60 km to the south-southeast of the epicenter. The highest acceleration, which was measured on the north-south component of the accelerometer, was  $128 \text{ cm/sec}^2$ , while the maxima on the vertical and east-west components were  $30 \text{ cm/sec}^2$  and  $56 \text{ sec/cm}^2$  respectively. The accelerometer triggered sometime during the arrival of the P-wave train so it did not record the initial arrival of energy. However, the S-wave and some surface waves were well-recorded by the instruments which remained triggered for about 60 sec.

The acceleration records have been integrated into velocity and displacement waveforms, and the horizontal displacement traces were found to match the Carder displacement records quite well, as discussed by Heaton (1977). The north-south record, which is shown in Figure 11, is of particular interest because it represents primarily SH motion. Heaton and Helmberger (1977) have done extensive modeling of the SH displacement record. They determined that the long-period oscillations which characterized most of the later part of the displacement record were due to SH rays trapped in a near surface crustal layer and that they could isolate a source time function by modeling the initial part of the SH wavetrain. The time function from their best model was actually the sum of three different time functions--two triangles of one second duration each located at a depth of 8 km and occurring 2 seconds apart, and a third low amplitude, long-period time function put at 4 km depth and beginning at the same time as the first source. The shape of the time function of Heaton and Helmberger (1977) as it would appear to teleseismic stations is shown in Figure 12 along with that of Burdick and Mellman (1976) and the time history determined from the simultaneous inversion as listed in Table 3. It can be seen that the Heaton and Helmberger (1977) time function and that determined from this study are quite similar, and that the Burdick and Mellman (1976) time function is a smoothed version of the other two.

The success in modeling both the teleseismic short-period P waves and the strong-motion SH ground displacements at El Centro was an inducement to try to understand the north-south velocity and

acceleration records at El Centro. This is not an easy thing to do since the synthetic velocity and acceleration traces are calculated from derivatives of the synthetic displacement record, and small changes in the shape of the displacement record have large effects on the waveshapes and amplitudes of the synthetic velocity and acceleration. On the other hand, the modeling is simplified somewhat since by far the highest amplitude velocity and acceleration arrival is that of the S wave (Heaton and Helmberger, 1977) which is found between about 7 and 10 seconds after the beginning of the record (Figure 11). Attention was restricted to understanding this part of these two records.

Initial modeling of the S wave on the velocity and acceleration records revealed that the waveform is not made up of a single direct arrival from the source as assumed by Heaton and Helmberger (1977) but that there are some important crustal complications involved in it. The differences can be seen in the step function responses shown in Figure 13. The response in Figure 13 (a) is made up of a simple direct arrival plus later reverberations in a near-surface sedimentary basin. The response in Figure 13 (b) shows the response from a source located in a crust with a modification of the crustal structure proposed by Mooney and McMechan (1980) listed in Table 2 (the basin bounces are not included in this response). The latter response, in which only the most significant rays are included, has a strong reflection from the lower crust which occurs a little over a second after the initial arrival. This response was the one used in the calculation of the synthetics.

From the initial modeling it was also found that large initial

source time function needed to be symmetric in shape. The best trapezoidal time function was found to be one with durations of the legs and top of .8 sec and .2 sec respectively. It was necessary to filter this time function in order to make it smoothly differentiable. A symmetric time-domain triangle was used as this filter. It was discovered that the synthetics were quite sensitive to the width of this smoothing filter. Synthetic displacement, velocity and acceleration records for the trapezoidal source smoothed with triangles which have legs of duration ( $\tau$ ) .2 sec, .3 sec and .4 sec are shown in Figure 14. The general shape of the synthetics fit the observations fairly well, but the frequency content and amplitude of the velocity and especially the acceleration records are strongly affected by the choice of the filter duration. Thus a time function which best fits the data could be found by varying the width of this smoothing filter.

The second source, which had been inferred by both the teleseismic short-period P wave and the strong-motion displacement modeling, was added to the model and synthetics were again computed in an effort to understand how it may affect the waveforms. This source was approximated by using the analytic time function of Haskell (1967). This source time history, which is shown together with its displacement, velocity and acceleration time functions in Figure 15, has been used in the description of the source time functions of large explosions. The reason for using it here was twofold: the source could be smoothly differentiated to find accelerations and the accelerations from the source are basically a pulse with a sharp rise followed by a long tail.

The latter was felt to be important because the highest peak on the acceleration record has this one-sided nature. The source is parameterized by one independent constant  $k$  which was varied until the pulse had roughly a 1.2 sec duration. Synthetic accelerograms with two sources where the second source has  $k = 5$  and  $k = 7$  ( $\tau = .3$  for both) and a moment of  $6.4 \times 10^{25}$  dyne-cm are shown in Figure 16 along with plots of the displacement time histories of the second sources. The time separation of the two sources necessary to best fit the data was 1.6 sec. While this is less than the 2.2 sec found from the teleseismic modeling, the peak of the displacement time function with  $k = 5$  occurs about 2.2 sec after the first source. Thus, if the Haskell (1967) time function is thought of as a smoothed version of the teleseismic short-period triangular source, the discrepancy in the timing of the two sources found at El Centro and in the teleseismic short-period body waves is unimportant. It is evident from Figure 16 that the effect of the second source is to add high frequency information to the acceleration record synthesized with just the first source. The velocity and displacement synthetics are almost totally unaffected by the addition of the second source.

One of the most puzzling features of the El Centro records is that the SH pulse shows up much more strongly on the north-south than on the east-west component whereas both components should have similar amplitudes. This could be due to the arrival not following the shortest path from source to receiver or from a rotation of the focal mechanism relative to that found in the modeling process. The former suggestion

is unlikely given what is known about the crustal structure of the Imperial Valley (Mooney and McMechan, 1980), but the latter requires a  $18^{\circ}$  change in the fault strike relative to that given in Table 3 for the inversion models (to a more east-west striking fault). To test how this latter suggestion would affect the far-field waveforms, synthetic long-period and short-period waveforms were computed with the simultaneous inversion model where the source strikes were changed to  $-61^{\circ}$  and  $-54^{\circ}$ . These synthetics are shown in Figure 17. The short-period records do not fit quite as well over all as with the best-fitting models described earlier, but on the other hand the match is not bad. Some stations like NAT and BOG appear improved by the rotation in fault strike (Figure 17a). The long-period fits are noticeably different at many stations, and generally for the worse (Figure 17b). On the basis of the short-period data alone, one could conclude that the strike of the short-period part of the seismic break was rotated by  $18^{\circ}$  relative to the long-period level coupled with the long-period data, although one must regard this hypothesis with uncertainty.

#### DISCUSSION

The results of the strong-motion modeling combined with the analysis of the short-period data strongly indicates that much energy from the earthquake was radiated in two pulses of about 3 seconds total duration. The duration of these pulses is approximately the same at all azimuths for which there is good data, so there is little evidence for directivity in the source. If the rupture is assumed to have initiated

at a single point on the fault and then propagated circularly away with a subsonic rupture velocity, the area which radiated these pulses must have been small compared to the fault size inferred from the aftershocks and surface breakage.

From the source parameters of the earthquake given in Table 3 and using the assumptions just made some of the details of the faulting process can be quantified. Fault areas and stress drops were computed from the formulations of Ebel *et al.* (1978) and Kanamori and Anderson (1975) respectively and are given in Table 4. The faults areas for the short-period and long-period sources are assumed to be circular and that for the entire main shock was approximated from the aftershock distribution (see Figure 18). It is evident from Table 4 that the two sources found from short-period body wave analysis broke only about 15% of the total fault plane. These sources also had very large seismic moments and it is the combination of these two parameters that gives then the high stress drops. A stress drop of 96 bars was determined by Burdick and Mellman (1976) from their study of the long-period body waves, and a still lower stress-drop value of 20 bars for the event was computed from the total fault area given in Table 4 and the surface-wave moment of  $3 \times 10^{26}$  dyne-cm (Burdick, 1977). These stress drop estimates show that while the rupture initiated with two very high stress drop events, the total rupture had a much lower average stress drop.

The location of the region which radiated the two high amplitude pulses may have been the northern end of the fault zone where the epicenter of the event as well as that of the immediate foreshock were

located (Allen and Nordquist, 1972) and where the largest surface displacements were measured (Clark, 1972; Figure 19). The reason for this is that the first arrivals on the teleseismic records as well as the initial SH pulse at El Centro are dominated by these strong arrivals. As the initial motions at the Caltech network stations put the hypocenter near the northern end of the fault (Figure 1), the first arrivals at the teleseismic stations probably also came from this source region. The distribution of aftershocks projected on the fault determined by Hamilton (1972) which is reproduced in Figure 17 has an interesting feature. At the northern end of the fault trace there is a gap of about 6 km where there were almost no aftershocks. The size of this gap (which may have been outlined in Figure 17) is approximately the same size as that which radiated the high amplitude body wave pulses. The surface faulting on the northern segment of the fault breakage did not have any noticeable aftercreep on it while the central and southern parts underwent significant post-seismic displacements (Clark, 1972; Burford, 1972; Figure 18). Burford (1972) notes that the basement under the northern part of the surface faulting is covered by a thin layer of sediments, while the basement under the central and southern traces lies under several hundred meters to several kilometers of sedimentary rock. He argues that the aftercreep may have been a delayed response of the sediments to the initial coseismic displacement of the basements rock. However, since the aftercreep died away at the same time that the aftershock activity dropped to a very low level (Burford, 1972), it may reflect the existence of post-seismic

movements in the basement rock.

The high stress-drop beginning of the Borrego Mountain earthquake and the small source area for the initial fault break suggest that this event began with the failure of an asperity. Asperities, or regions of locally high breaking strength on a fault, have been proposed by Kanamori (1977) to explain the multiple rupture of some earthquakes. Rudnicki and Kanamori (1980) have shown that a small, strong asperity on a fault could fail with a very high stress drop and that the crack would then propagate into an area with a much lower breaking strength. The stress drop averaged over the entire fault area would be much lower than that of the asperity. The analysis of the Borrego Mountain event indicates that the time history of the stress drop follows that described by Rudnicki and Kanamori (1980) for an asperity-controlled earthquake. The asperity in the Borrego Mountain fault zone was about 6 km in diameter and located at the northern end of the fault; the rest of the fault breakage was probably some sort of readjustment to the initial break. The existence of aftercreep on the central and southern parts of the fault zone suggest that not all of this readjustment managed to take place at the time of the main shock. The asperity possibly even had a substantially different strike than the surface breakage.

The question immediately arises from the above discussion as to whether or not there is any tectonic reason for the existence of an asperity on the northern end of the fault. Since this fault is part of the San Jacinto fault zone which has undergone at least 24 km of

displacement (Sharp, 1972), it is possible that the bedrock is different on the two sides of the fault. At the surface the part of the fault where the maximum coseismic displacement took place is in a zone where Tertiary and Quaternary sedimentary rock on the east abut a part of Borrego Mountain which is made up of crystalline rock on the west (Sharp, 1972). This place is the only location along the 1968 rupture where on the surface there was anything but sedimentary rock in contact across the fault. If there is a contrast of the basement rock across the fault in this area, then the results of this study indicate that this contrast may locally cause the fault zone to have a very high breaking strength. The size and the stress drop of the asperity would indicate a fracture strength of about  $4 \times 10^{10}$  erg/cm<sup>2</sup>, which is even larger than the high value that Aki (1979) calculated for the 1966 Parkfield earthquake. While the surface geology may not be representative of the structure at depth along the fault zone, it can be said that in this case the location of the asperity correlates with a change in surface geology along the fault zone.

Finally, probably the most important result obtained from this study is the documentation of the role played by asperities in peak intensities. In particular, the high acceleration observed at El Centro appears to be caused by a rather small section of fault which had very little to do with the over all faulting dimension. A similar conclusion can be drawn from a study of the San Fernando strong motions (see Heaton and Helmberger, 1980). Thus, simulation techniques that distribute the high frequency energy release uniformly along the proposed faulting

surface may need some adjustments as in Wiggins *et al.* (1978) or Hadley and Helmberger (1980). Unfortunately, predicting where asperities will occur for a given fault zone may be very difficult unless they can be recognized by geological features or surmised by seismic data.

#### CONCLUSIONS

The short-period teleseismic P waves from the 1968 Borrego Mountain earthquake have been studied and source models have been found which fit not only those records but the teleseismic long-period body waveforms and the strong motion SH record at El Centro as well. From the deconvolutions and the forward and inversion modeling of the waveforms it was found that the source radiation came in two pulses separated by about 2.2 seconds. The sources for each of these pulses were located at about 8 km depth and had similar focal mechanisms, but the second was only about a third the amplitude of the first. The duration of the time function for the first source is fairly well constrained at about 2.1 seconds while there is less resolution on that of the second source. The moment at short periods is 12% to 33% less than that calculated from the long-period data and is 80% to 85% less than that from the surface waves.

There were some problems with the short-period data set. The signal-to-noise ratio is poor on many records and at some stations there is an apparent mismatch of information between the short-period and long-period records. There is also some evidence for either laterally varying structure in the source region or for different focal mechanisms

at short and long periods. Even so, it was demonstrated that the short-period waveforms contain much detailed information on the source time history of the earthquake and in particular on the near-source strong ground motions.

The two sources found in the short-period analysis were determined to have small source areas and large stress drops. However, the average stress drop for the event was much lower indicating that the earthquake began with the failure of a strong asperity at the northern part of the fault. This asperity was located in an area where there were almost no aftershocks, and it lay beneath the place where there is a contrast in rock type across the fault.

#### ACKNOWLEDGEMENTS

Special thanks must be made to several people for their assistance with this study. Gladys Engen ran much of the analysis on the strong-motion data and was responsible for finding the fits to the acceleration record. George Mellman kindly provided his inversion program and made up for the lack of written comments in the program with oral instructions about its inner workings. Dave Boore and Allen Olsen reviewed the manuscript and their comments prompted some unexpected improvements in the analysis. Joe Galvan and Laszlo Lenes helped prepare the figures. This research was supported by the National Science Foundation under grant No. PFR-7921769 and also Advanced Research Projects Agency of the Department of Defense and was monitored by the Air Force Office of Scientific Research under Contract No. F49620-77-C-0022. Contribution No. 3523, Division of Geological and Planetary Sciences, California Institute of Technology, Pasadena, California 91125.

## REFERENCES

Allen, C. R., and J. M. Nordquist, (1972). Foreshock, main shock and larger aftershocks of the Borrego Mountain earthquake, U. S. Geological Survey Professional Paper 787, 16-23.

Bache, T. C., D. G. Lambert and T. G. Barker, (1980). A source model for the March 28, 1975 Pocatello Valley earthquake from time-domain modeling of teleseismic P waves, Bull. Seism. Soc. Am., 70, 405-418.

Burdick, L. J., (1977). Broad-band seismic studies of body waves. Ph. D. thesis, Calif. Inst. of Tech.

Burdick, L. J., and G. R. Mellman, (1976). Inversion of the body waves of the Borrego Mountain earthquake to the source mechanism, Bull. Seism. Soc. Am., 66, 1485-1499.

Burford, R. O., (1972). Continued slip on the Coyote Creek fault after the Borrego Mountain earthquake, U. S. Geological Survey Professional Paper 787, 105-111.

Cipar, J. C., (1980). Broad-band time domain modeling of earthquakes from Fruili, Italy, submitted to Bull. Seism. Soc. Am.

Clark, M. M., (1972). Surface rupture along the Coyote Creek fault, U. S. Geological Survey Professional Paper 787, 55-86.

Ebel, J. E., L. J. Burdick and G. S. Stewart, (1978). Source mechanism of the August 7, 1966 El Golfo earthquake, Bull. Seism. Soc. Am., 68, 1281-1292.

Fuchs, K., (1966). The transfer function for P waves for a system consisting of a point source in a layered medium, Bull. Seism. Soc. Am., 56, 75-108.

Futterman, W. I., (1962). Dispersive body waves, J. Geophys. Res., 67, 5279-5291.

Hadley, D. and D. V. Helmberger (1980). Physical basis for the shape of the attenuation relationship, Bull. Seism. Soc. Am., in press.

Hamilton, R. M., (1970). Time-term analysis of explosion data from the vicinity of the Borrego Mountain, California, earthquake of 9 April 1968, Bull. Seism. Soc. Am., 60, 367-381.

Hamilton, R. M., (1972). Aftershocks of the Borrego Mountain earthquake from April 12 to June 12, 1968, U. S. Geological Survey Professional Paper 787, 31-54.

Hartzell, S., (1980). Faulting process of the May 17, 1976 Gazli, U.S.S.R. earthquake, Bull. Seism. Soc. Am., 70, 1715-1736.

Haskell, N. A., (1967). Analytic approximation for the elastic radiation from a contained underground explosion, J. Geophys. Res., 72, 2583-2587.

Heaton, T. H., (1977). Generalized ray models of strong ground motion, Ph. D. thesis, Calif. Inst. Tech.

Heaton, T. H., and D. V. Helmberger, (1977). A study of the strong ground motion of the Borrego Mountain, California, earthquake, Bull. Seism. Soc. Am., 67, 315-330.

Heaton, T. H. and D. V. Helmberger, (1979). Generalized ray models of the San Fernando earthquake, Bull. Seism. Soc. Am., 69, 1311-1341.

Helmberger, D. V. and L. J. Burdick, (1979). Synthetic seismograms. Ann. Rev. Earth Planet. Sci., 7, 417-442.

Helmberger, D. V. and S. D. Malone, (1975). Modeling local earthquakes as shear dislocations in a layered half space. J. Geophys. Res., 80, 4881-4888.

Kanamori, H., (1977). Use of seismic radiation to infer source parameters, Proceedings of Conference IV: Fault mechanics and its relation to earthquake prediction, U. S. Geological Survey open-file report #78-380, 283-318.

Kanamori, H. and D. L. Anderson, (1975). Theoretical basis of some empirical relations in seismology, Bull. Seism. Soc. Am., 65, 1073-1095.

Langston, C. A., (1978). Moments, corner frequencies and the free surface, J. Geophys. Res., 83, 3422-3426.

Langston, C. A. and D. V. Helmberger, (1975). A procedure for modeling shallow dislocation sources, Geophys. J. R. astr. Soc., 42, 117-130.

Mooney, W. D., and G. A. McMechan, (1980). Synthetic seismogram modeling of the laterally-varying structure in the central Imperial Valley, in The Imperial Valley earthquake of October 15, 1979: U. S. Geological Survey Professional Paper, in press.

Rudnicki, J. W. and H. Kanamori, (1980). Effects of fault interaction on moment, stress drop and strain energy release, J. Geophys. Res., in press.

Sharp, R. V., (1972). Tectonic setting of the Salton trough, U. S. Geological Survey Professional Paper 787, 3-15.

U. S. Coast and Geodetic Survey, Seismological Field Survey and California Institute of Technology, Earthquake Engineering Research Laboratory, (1968). Strong motion instrumental data on the Borrego Mountain earthquake of 9 April, 1968. No. 119.

Wiggins, R. A., G. A. Frazier, J. Sweet and R. Apsel, (1978). Modeling strong motions from major earthquakes, Proceedings of the Second International Conference on Microzonation, NSF, Vol. II, 693-699.

TABLE 1

Station	Distance	Azimuth	Moment ( $t^* = 1.0$ )	
			( $\times 10^{25}$ dyne-cm)	Short Period      Long Period
ARE	65°	132°	6.67	6.39
BEC	43°	76°		
BHP	42°	117°		
BOG	48°	117°	6.44	9.97
CAR	50°	105°		
COL	37°	338°	2.47	9.04
KEV	76°	14°	2.61	10.54
KIP	39°	263°		
KON	77°	25°	3.85	
LPB	67°	129°		
MAT	82°	308°	5.66	7.66
NAT	83°	100°	6.76	9.22
NNA	59°	133°	3.77	5.75
NUR	81°	18°	3.93	11.43
OGD	32°	64°		
PEL	79°	142°		
SCP	31°	65°	5.02	6.87
SEO	82°	308°		
STU	85°	33°	8.10	33.54
TRN	55°	101°		4.30
WES	36°	62°		5.43

TABLE 2

P velocity (km/sec)	S velocity (km/sec)	Density (g/cm <sup>3</sup> )	Thickness (km)
Hamilton (1970)			
2.5	1.6	1.4	0.4
5.1	3.0	2.3	2.5
6.0	3.5	2.7	11.1
7.1	4.2	3.2	11.0
7.9	4.6	3.6	--
Mooney and McMechan (1980)			
--	1.35	1.7	1.4
--	1.98	2.2	1.4
--	2.59	2.5	1.4
--	3.09	2.6	1.0
--	3.28	2.65	1.9
--	3.3	2.67	1.9
--	3.33	2.69	1.9
--	3.36	2.7	1.85
--	3.59	2.78	0.1
--	3.81	2.84	0.95
--	4.16	2.9	10.0

TABLE 3

	Mechanism		Time			Depth	Delay
	strike dip rake	$\delta t_1$	Function	$\delta t_2$	$\delta t_3$	amp	time
			(sec)				(sec)
Burdick-Mellman Model	-45° 81° 178°	.36	0.0	.45	1.0	8.0	--
Starting Model							
Source 1	-45° 80° 180°	0.3	1.0	0.3	1.0	8.0	0.0
Source 2	-30° 80° 180°	0.3	1.0	0.3	1.0	8.0	2.0
Short Period Inversion Model							
Source 1	-43° 78° 178°	.89	.82	.76	1.0	8.2	0.0
Source 2	-30° 63° 193°	.31	.64	.73	.34	9.0	2.3
Simultaneous Inversion Model							
Source 1	-43° 78° 178°	.54	.89	.75	1.0	7.3	0.0
Source 2	-38° 68° 197°	.05	.05	1.2	.35	8.4	2.2

For all models the second source was located 5.4 km southeast of the first.

TABLE 4

Event	Characteristic Fault Dimensions (km)	Fault Area (km <sup>2</sup> )	Seismic Moment b-Body Wave s-Surface Wave (dyne-cm)	Stress Drop (bars)
Source 1	7.7 (diameter)	47	$6.4 \times 10^{25}$ b	436
Source 2	4.0 (diameter)	13	$0.9 \times 10^{25}$ b	366
Total Fault	12 x 30	360	$3.0 \times 10^{26}$ s	20

Figure 1. Map of the focal region of the Borrego Mountain earthquake in Southern California from Burdick and Mellman (1976). The aftershocks from the earthquake generally lay in segment AE, while the surface faulting was confined to segment BD (BC delineates the northern fault break and CD the central and southern breaks). The location, moment ( $M_0$ ) and depth (h) of each of the three sources determined by Burdick and Mellman (1976) are also shown.

Figure 2. Short-period P waveforms recorded at 26 WWSSN stations. Note the coherence of the first several seconds of the waveforms from stations at similar azimuths. The star denotes the location of the earthquake.

Figure 3. Simultaneous long-period-short-period deconvolutions of the P waveforms from 8 stations. For each station a filtered version of the original data (light trace) is plotted above the reconvolved waveforms (heavy trace). The amplitudes of the waveforms are arbitrary.

Figure 4. Synthetic short-period P waveforms computed from the Burdick and Mellman (1976) strike-slip source model compared to the data. The closed circles in the focal mechanism represent compressional arrivals, while the open circles are dilatational arrivals. The amplitudes of the waveforms in this and all of the following figures are arbitrary unless otherwise noted.

Figure 5. Short-period synthetics from the short-period inversion model compared to the data.

Figure 6. Long-period synthetics from the short-period inversion model compared to the data.

Figure 7. Short-period synthetics from the simultaneous inversion model compared to the data.

Figure 8. Long-period synthetics from the simultaneous inversion model compared to the data.

Figure 9. Comparison of synthetics computed from the simultaneous inversion model without instrument or attenuation and the deconvolved observations. The synthetic at MAT was time shifted by about 2 seconds so the sP phases of the datum and synthetic are matched. The alignment of the synthetic waveforms at COL, STU and NUR with the data is somewhat arbitrary since the traces have very different shapes.

Figure 10. Comparison of the data (top trace; light line) with synthetics computed from just P, pP and sP (middle trace; heavy line) and with synthetics computed from the full response of the near-source crustal structure (bottom trace; heavy line) at ARE, KON, NAT and SCP.

Figure 11. Corrected acceleration, velocity and displacement records from the north-south component of the strong ground motion recorded at El Centro, California (from U. S. Coast and Geodetic Survey et al., 1968).

Figure 12. Comparison of the time functions for the Borrego Mountain earthquake determined from the long-period body waves (top), short-period body waves (center) and strong motion data (bottom). The time scale at the bottom is in seconds.

Figure 13. Step function responses for initial SH arrivals from (a) the study of Heaton and Helmberger (1977) and (b) the crustal model of

Mooney and McMechan (1980) as computed in this study. Peak amplitudes from a unit point source are given in each case.

Figure 14. Synthetic displacement, velocity and acceleration records (lower three lines) for the first source are compared to the data (top line) from the north-south El Centro strong ground motion record. Peak amplitudes for each trace are shown with the units at the bottom of each column. The duration of the legs of the triangle filter  $\tau$  are also given.

Figure 15. Description of the Haskell (1967) source. The peak amplitude of each waveform is given above the trace.

Figure 16. Synthetic accelerations (lower traces) computed from the two-source model are compared to the observed north-south acceleration record from El Centro (top trace). Also plotted on the left are the time functions for the second source computed from the Haskell (1967) formulation and the shape of the second source (the triangles) found from the simultaneous inversion. The triangles have been shifted .6 sec relative to the beginning of the Haskell (1967) source. Peak amplitudes of the accelerograms in  $\text{cm/sec}^2$  are given next to the traces, as are the peak amplitudes (in arbitrary units) of the Haskell (1967) time functions.

Figure 17a. Short-period data (left column), simultaneous inversion model synthetics (center column) and synthetics of the simultaneous inversion model with the fault strikes rotated by  $18^\circ$  (right column). Representative stations at different azimuths are shown.

Figure 17b. Long-period data (left column), simultaneous inversion model synthetics (center column) and synthetics of the simultaneous inversion model with the fault strikes rotated by  $18^{\circ}$  (right column).

Figure 18. Plot of aftershock locations with depth on a plane parallel to the surface faulting and perpendicular to the surface faulting from Hamilton (1972) (A, A', A'' and B, B' are shown in Figure 1). The arrow in the lower figure denotes the location of the surface faulting. The rectangular box in the upper figure shows the approximate fault area which probably participated in the main shock, and the outlined region under the northern part of the surface break shows the possible location of the asperity on the fault.

Figure 19. Graph of the surface faulting of the Borrego Mountain earthquake from Clark (1972). Point A' is referenced to Figure 1 and the abscissa is scaled in km.

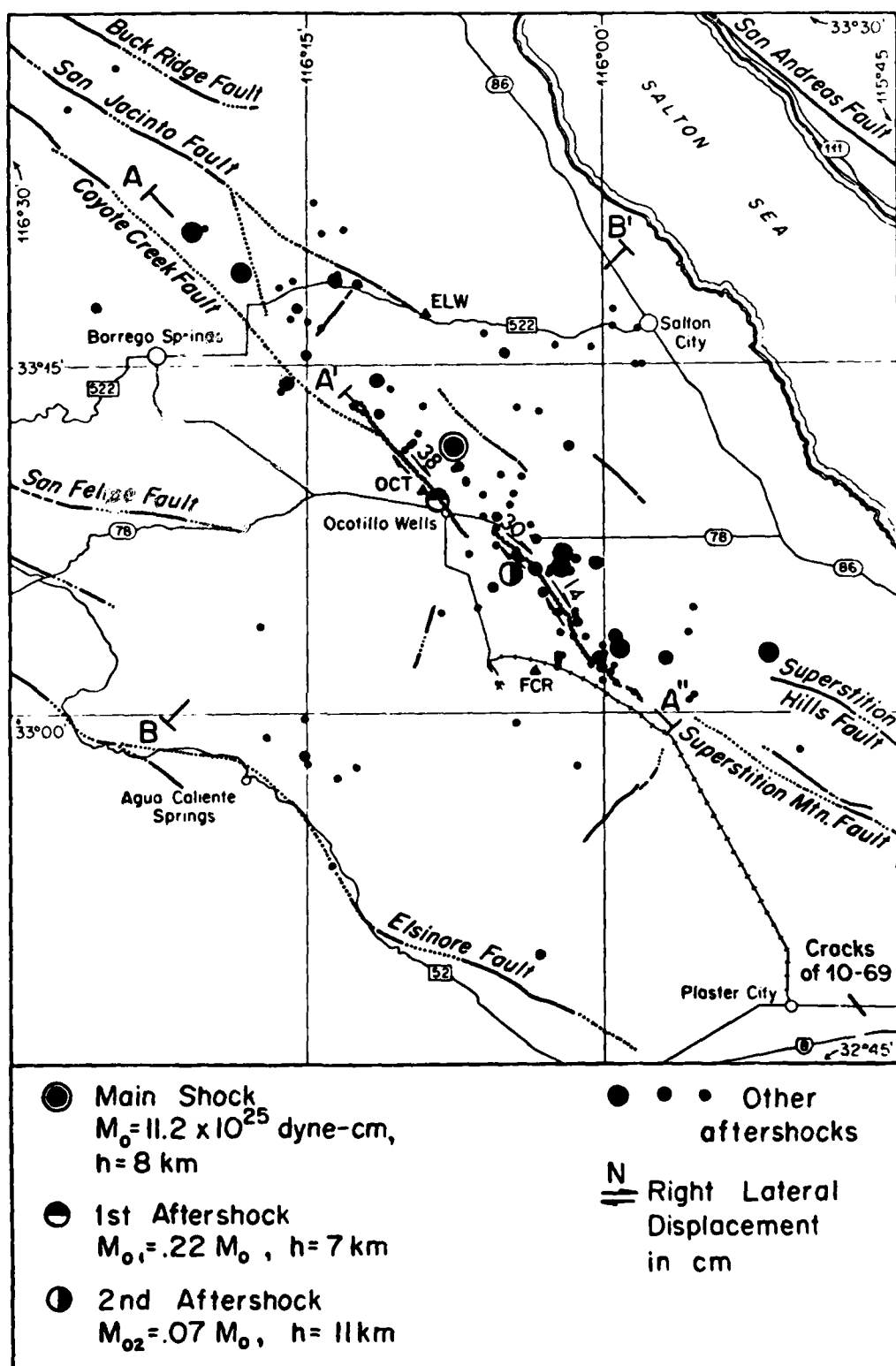


Fig. 1

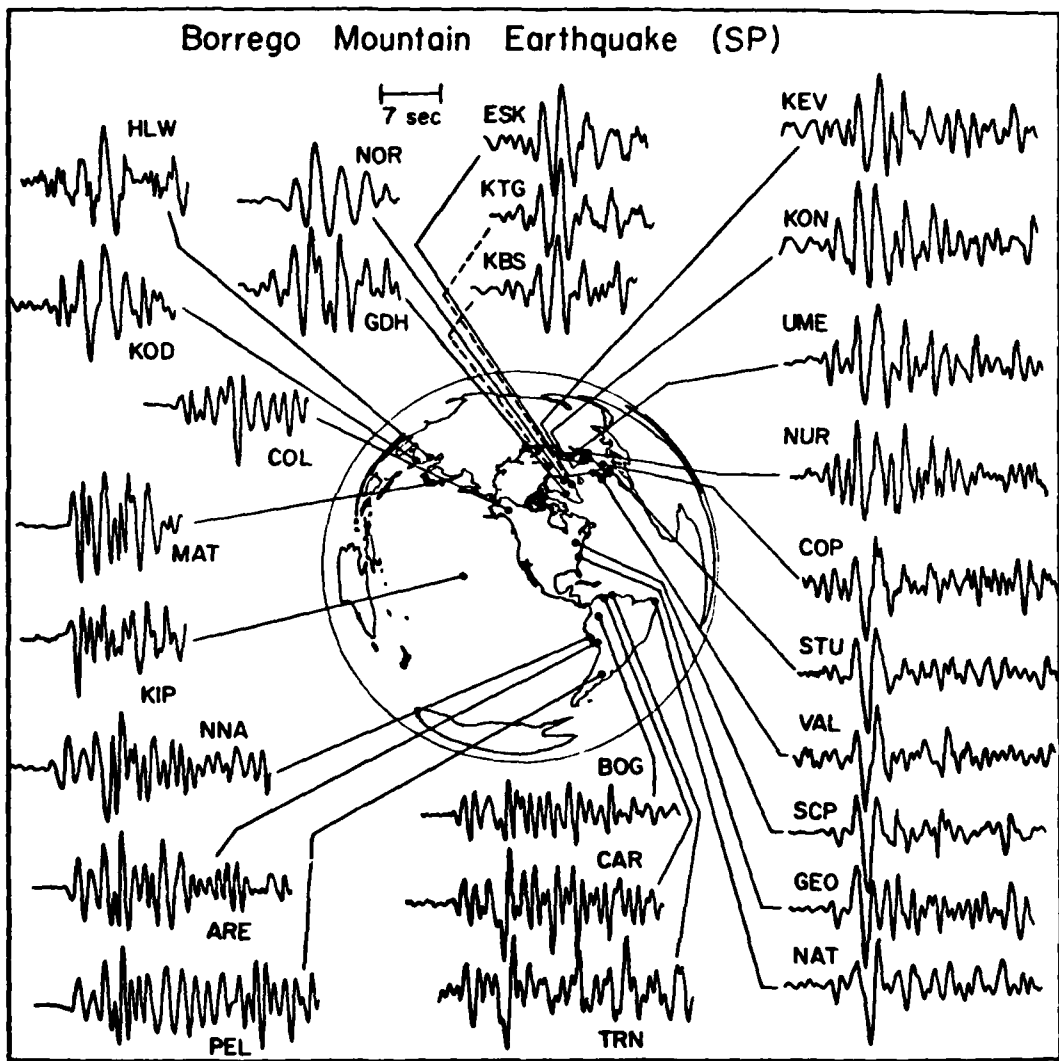


Fig. 2

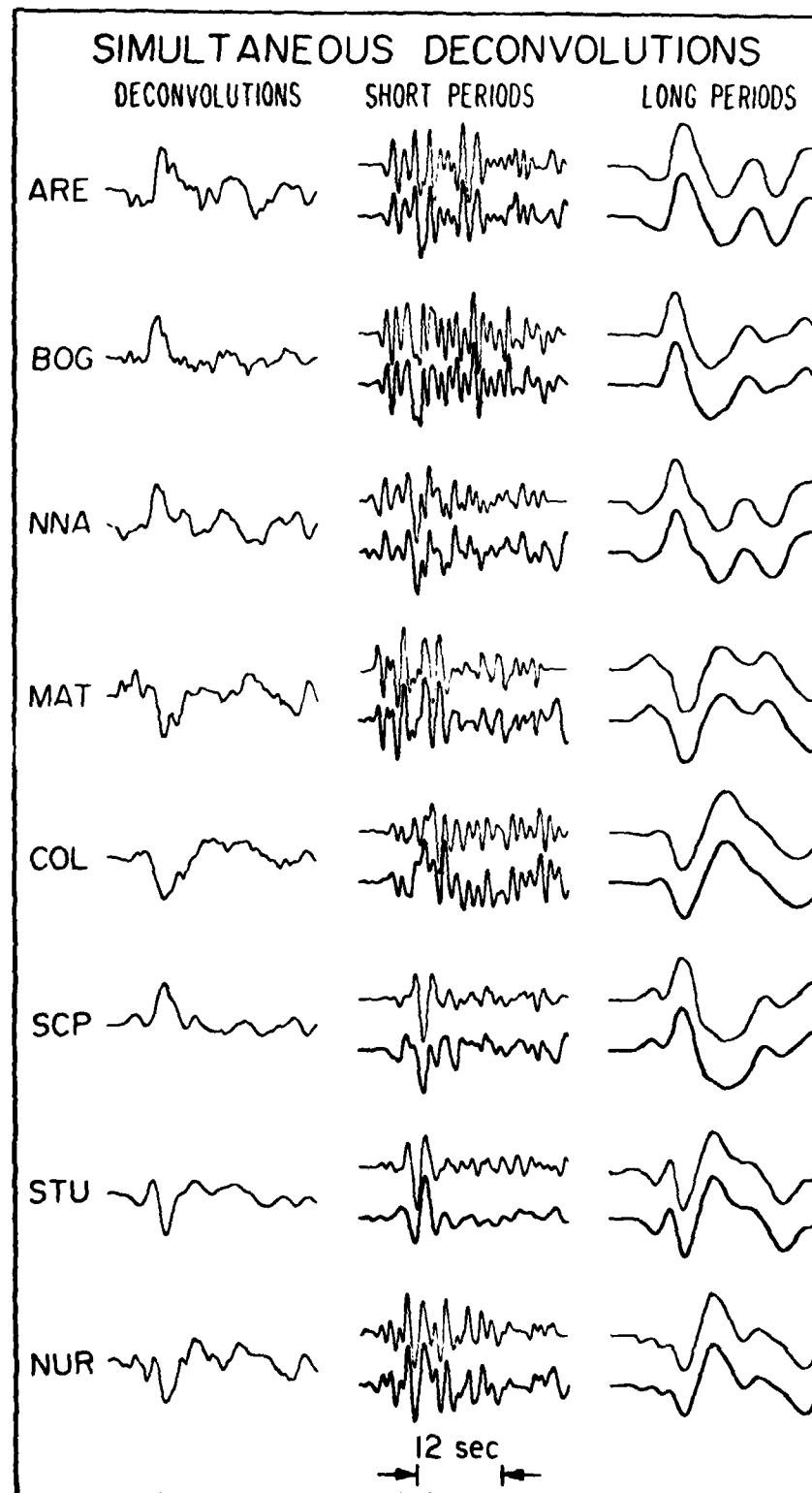


Fig. 3

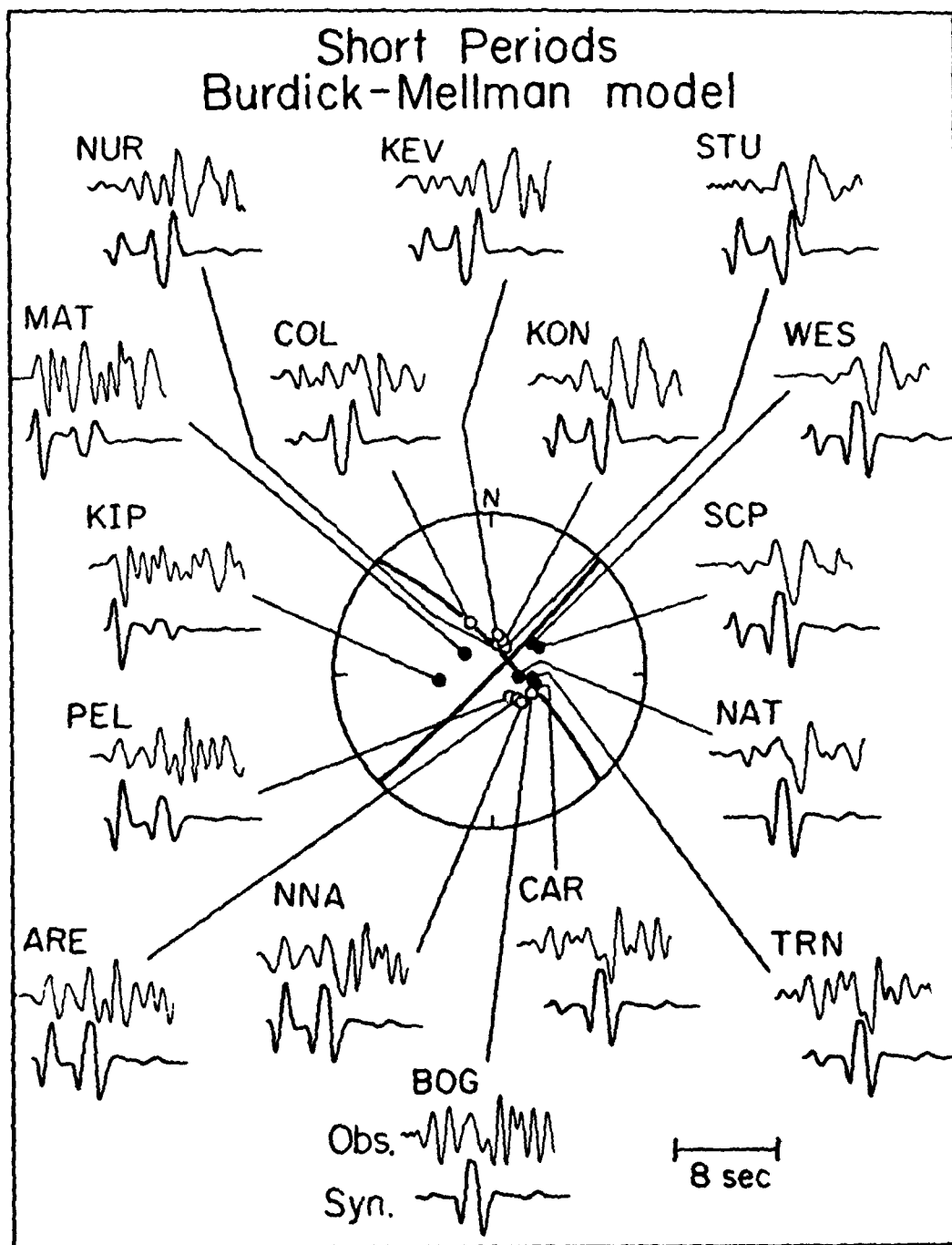


Fig. 4

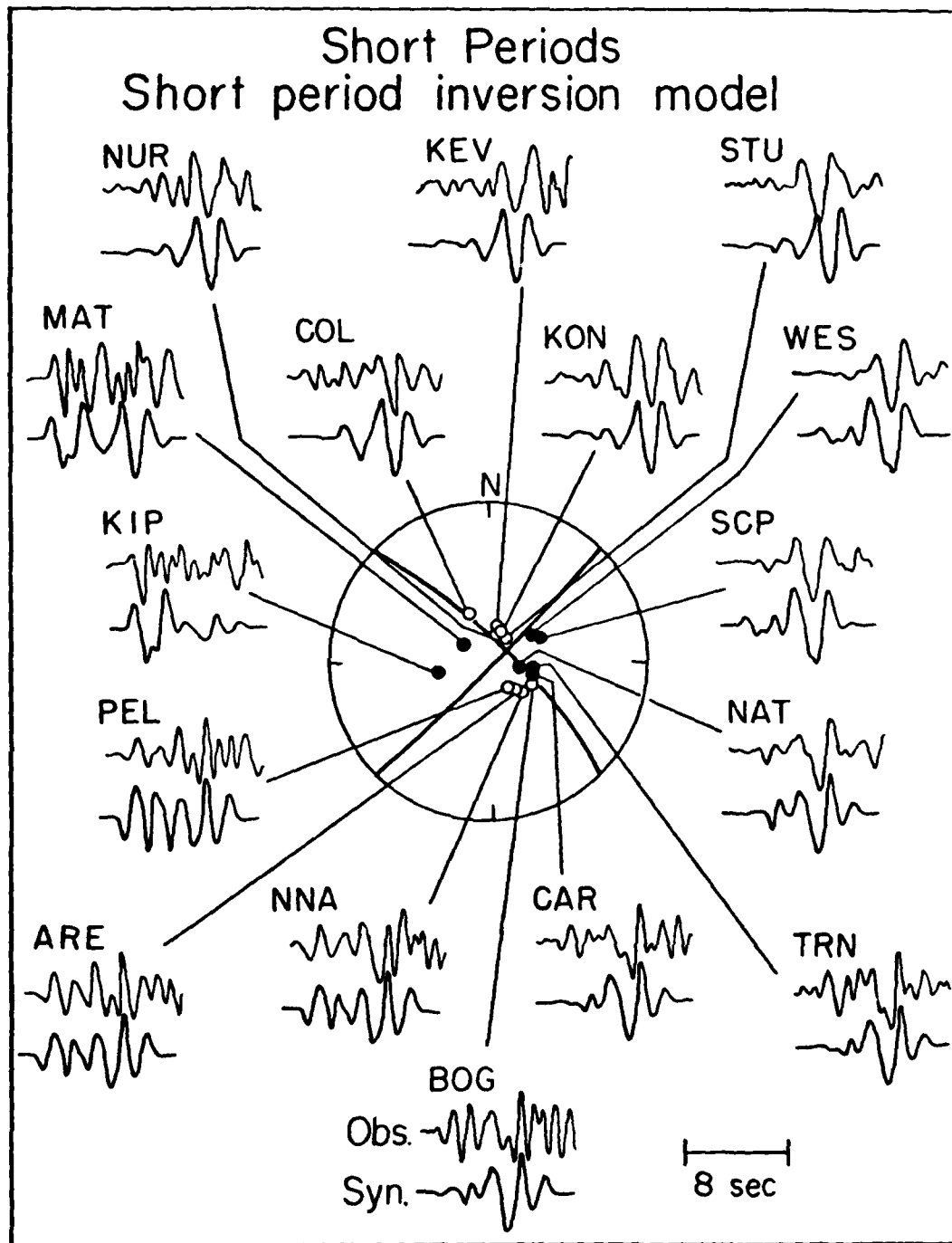


Fig. 5

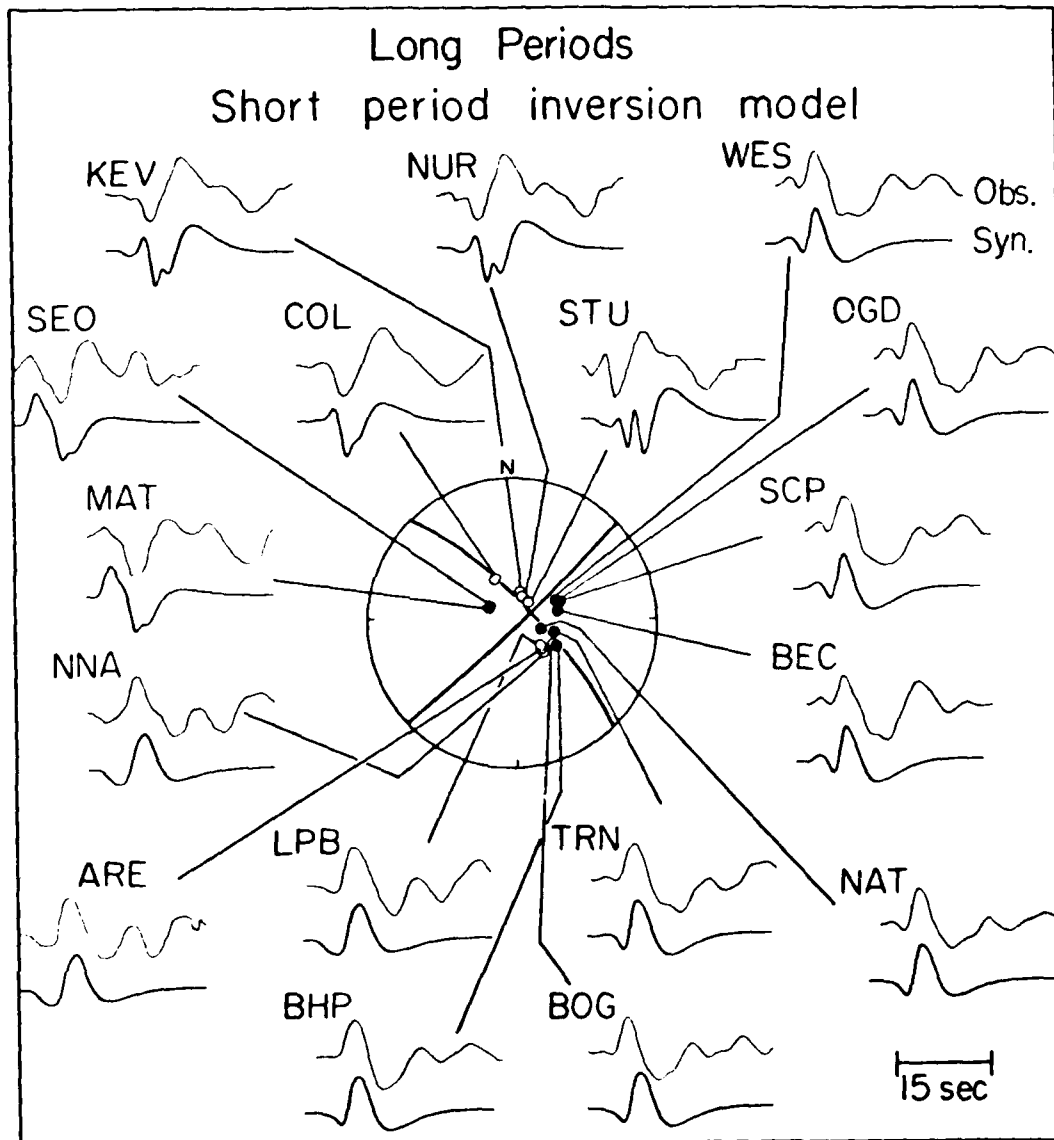


Fig. 6

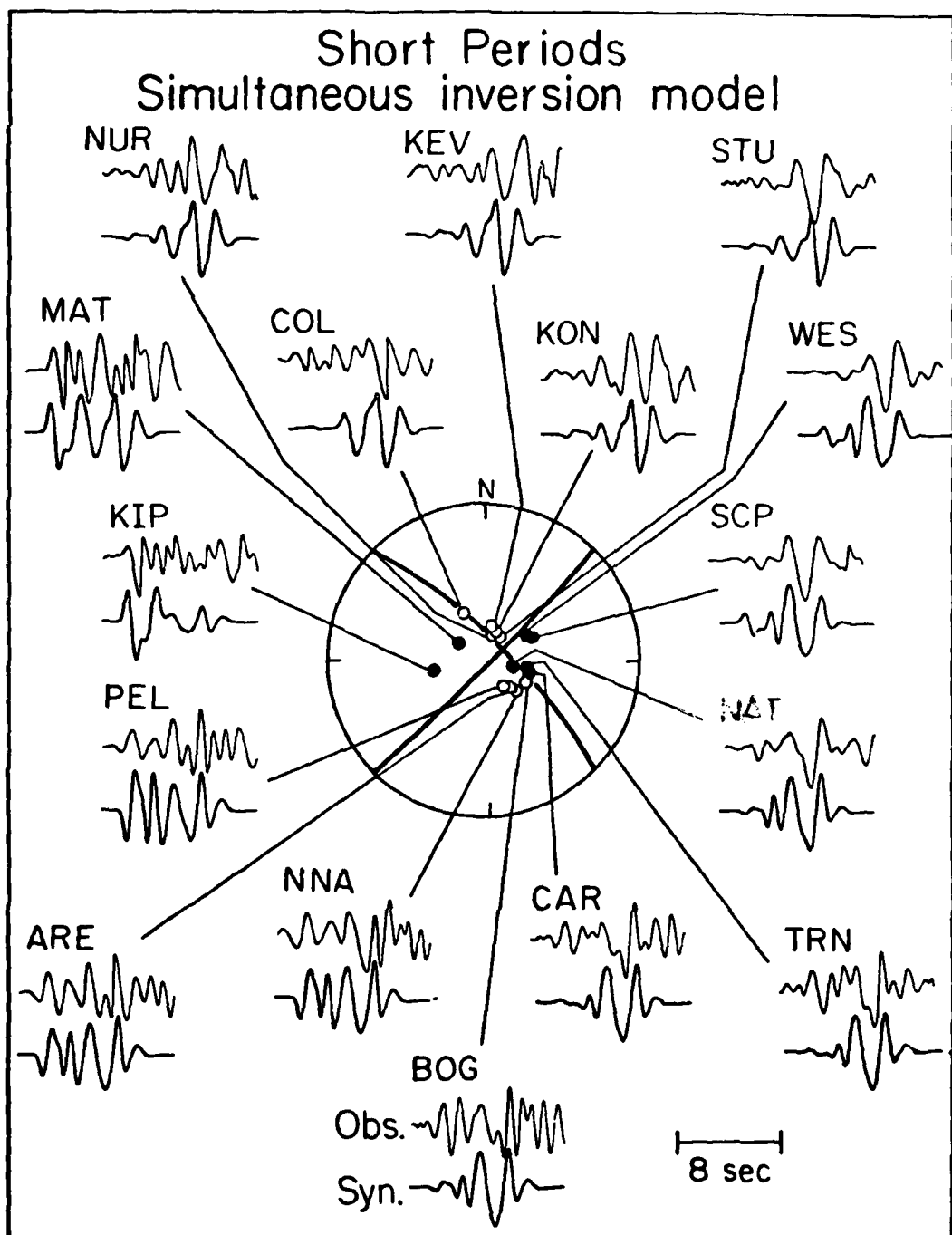


Fig. 7

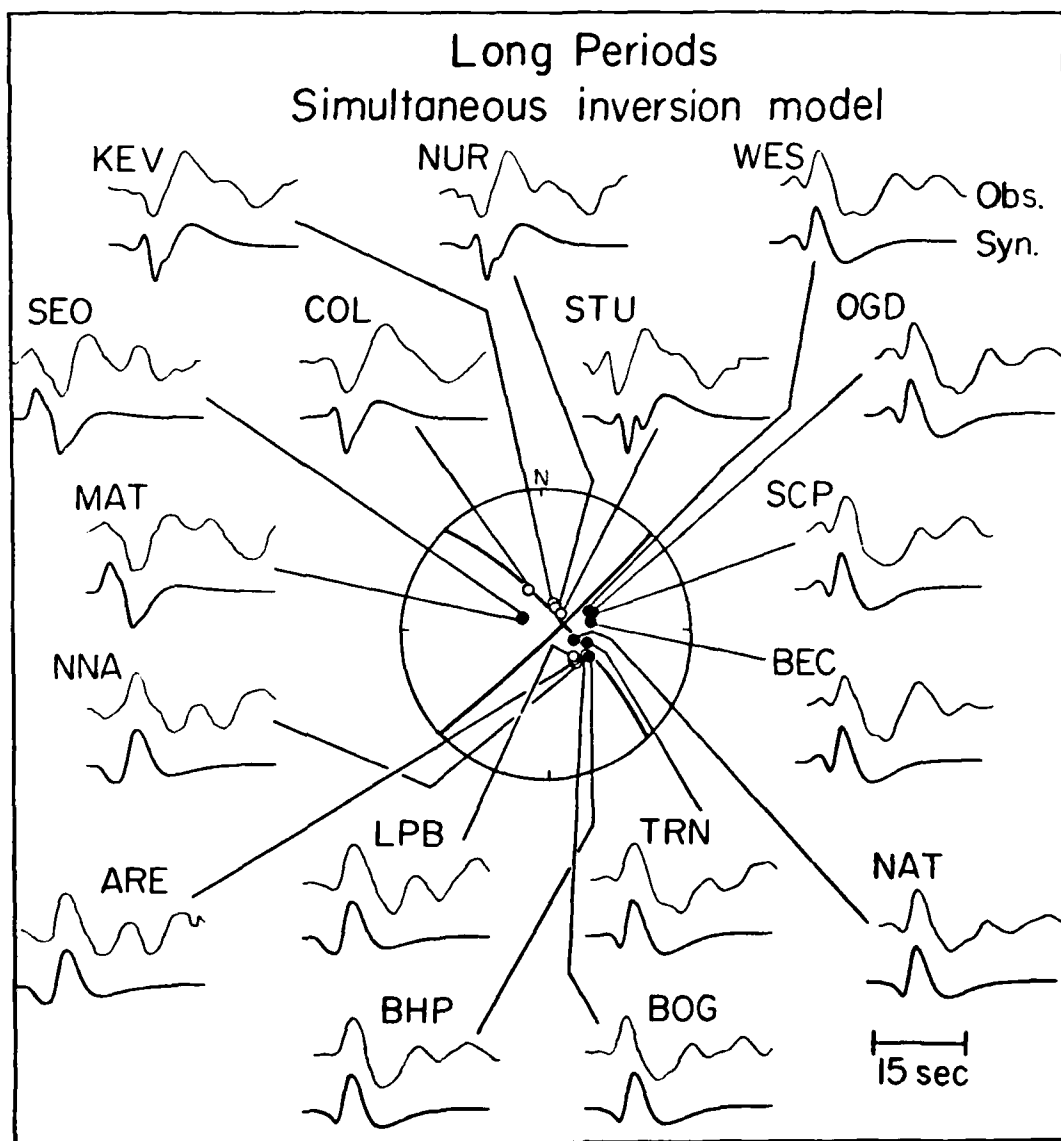


Fig. 8

DECONVOLUTIONS  
SIMULTANEOUS INVERSION MODEL

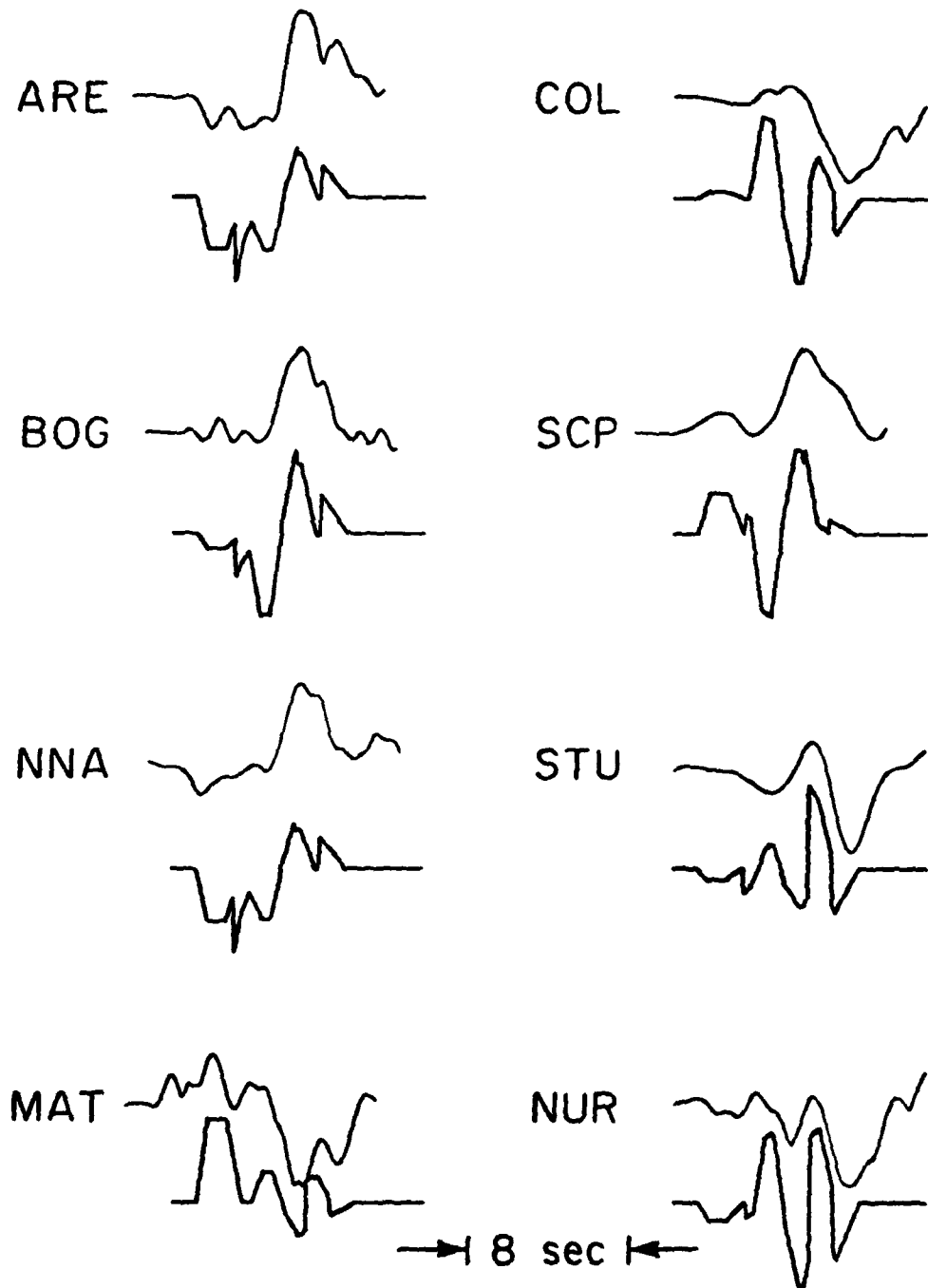


Fig. 9

SHORT PERIODS  
SYNTHETICS WITH & WITHOUT  
NEAR SOURCE STRUCTURE

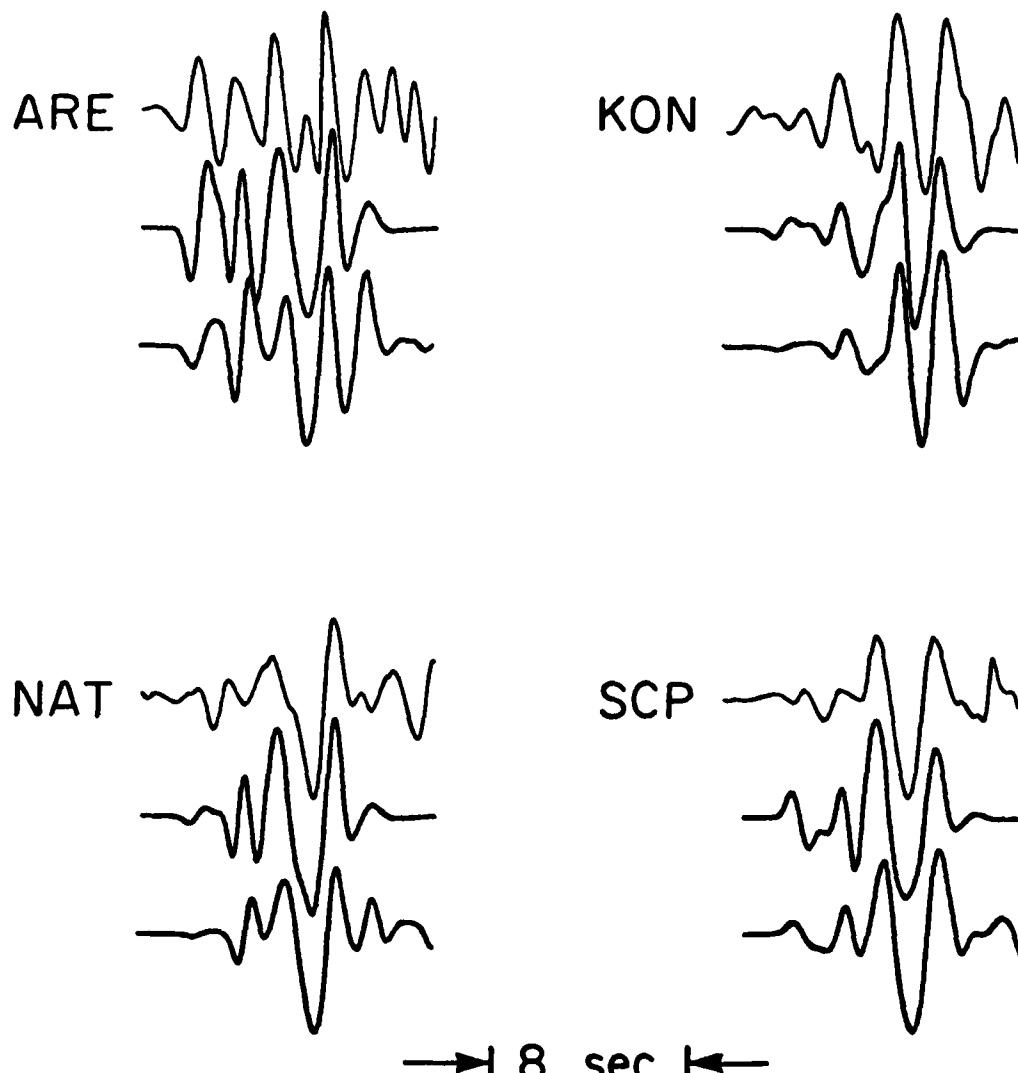


Fig. 10

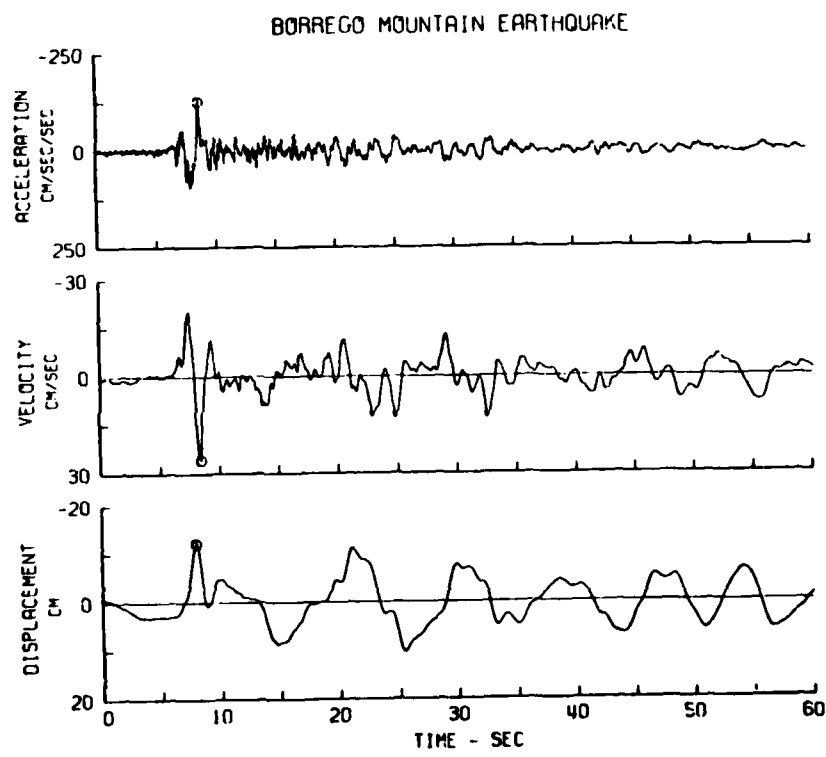
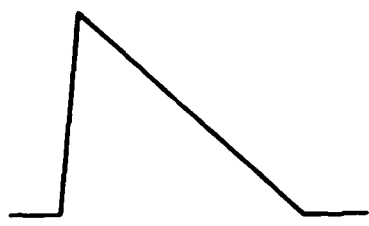


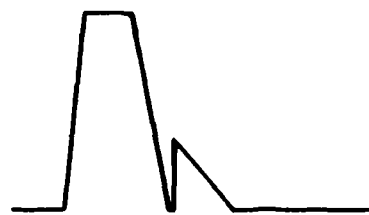
Fig. 11

## TIME FUNCTIONS

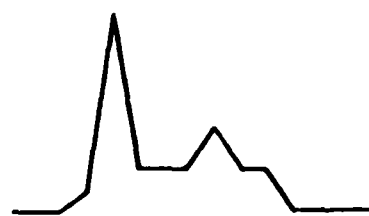
LONG PERIOD  
(BURDICK &  
MELLMAN, 1976)



SHORT PERIOD  
(THIS STUDY)



STRONG MOTION  
(HEATON &  
HELMBERGER, 1977)



0 1 2 3 4 5 6

Fig. 12

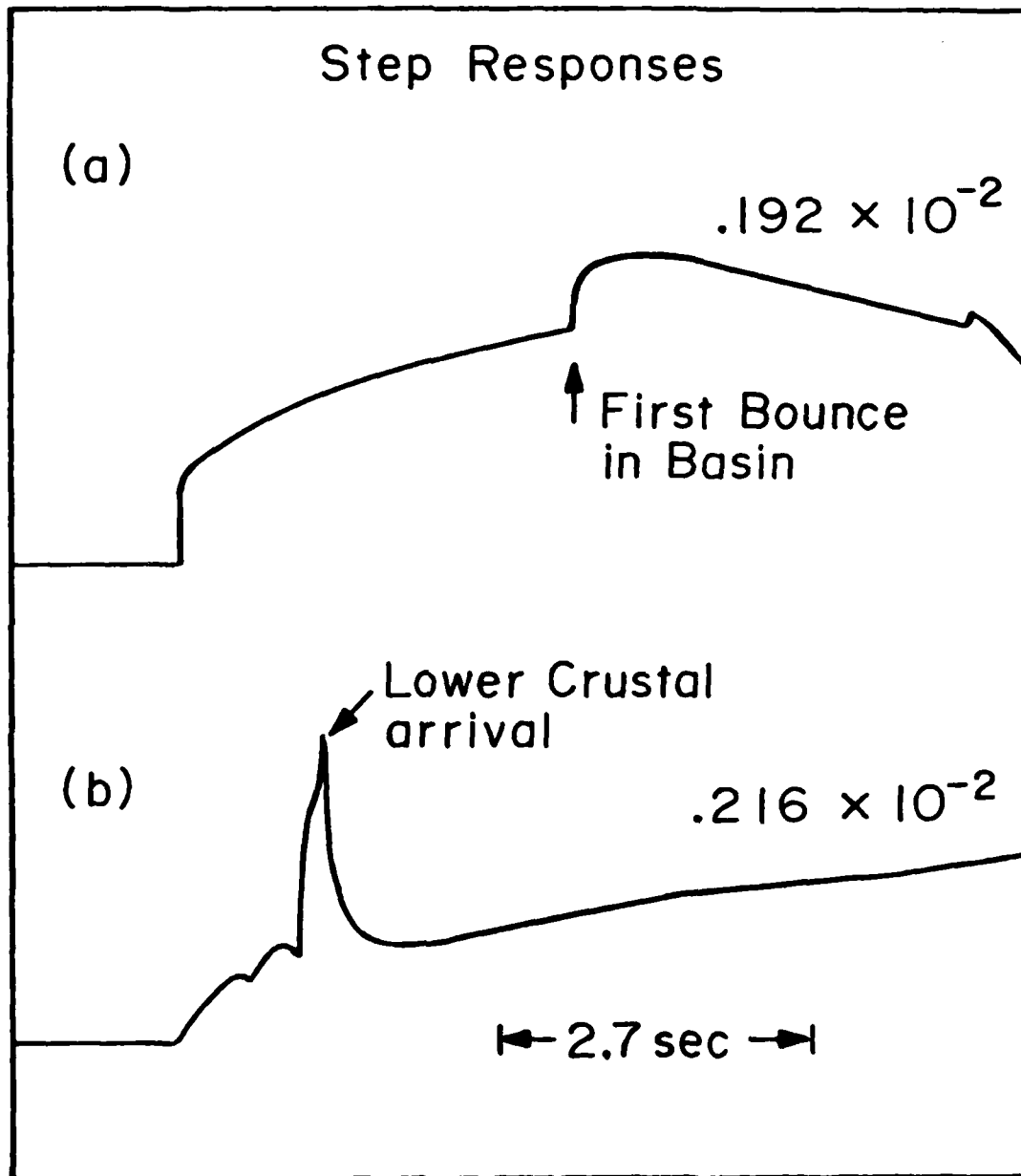


Fig. 13

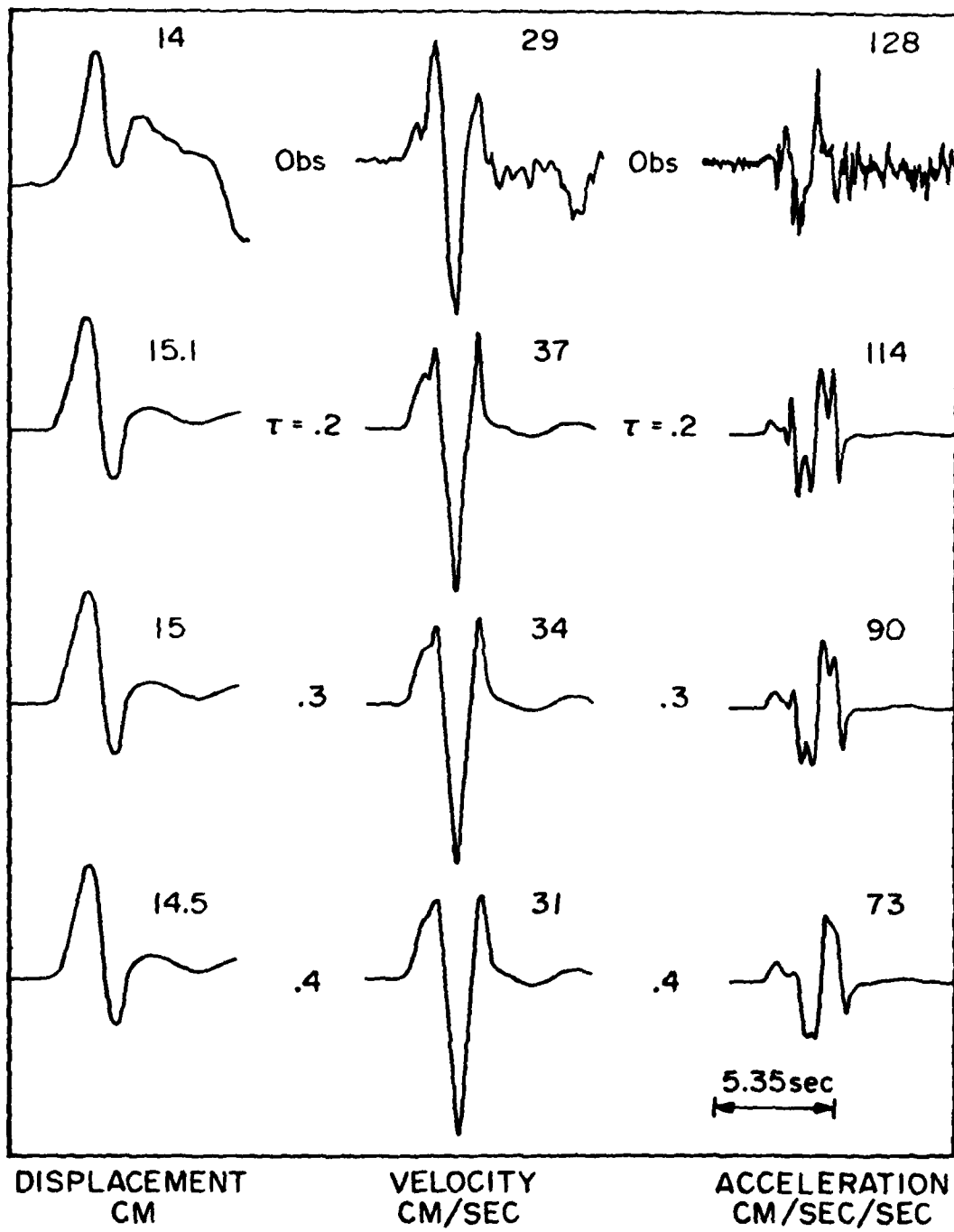


Fig. 14

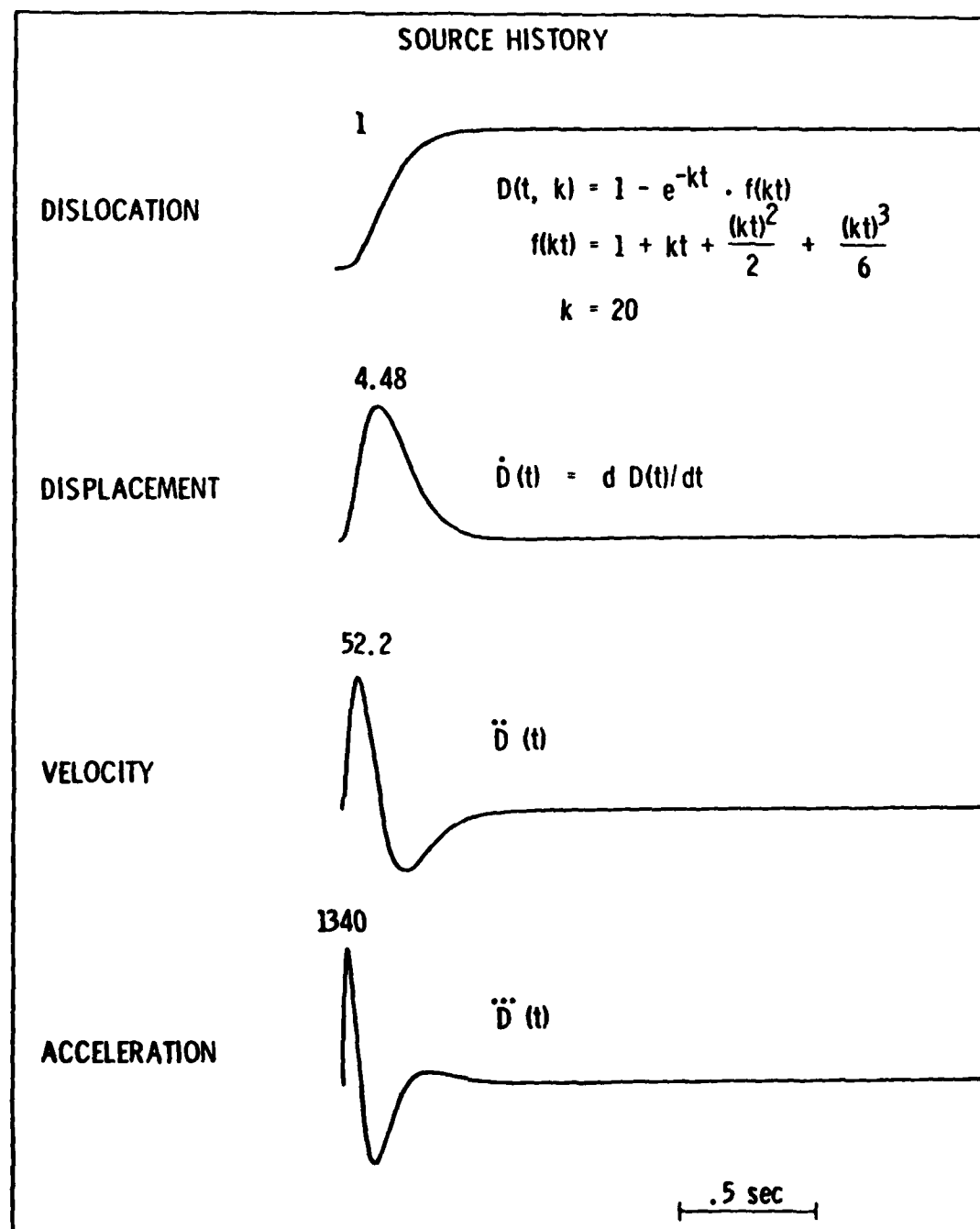


Fig. 15

## Accelerations

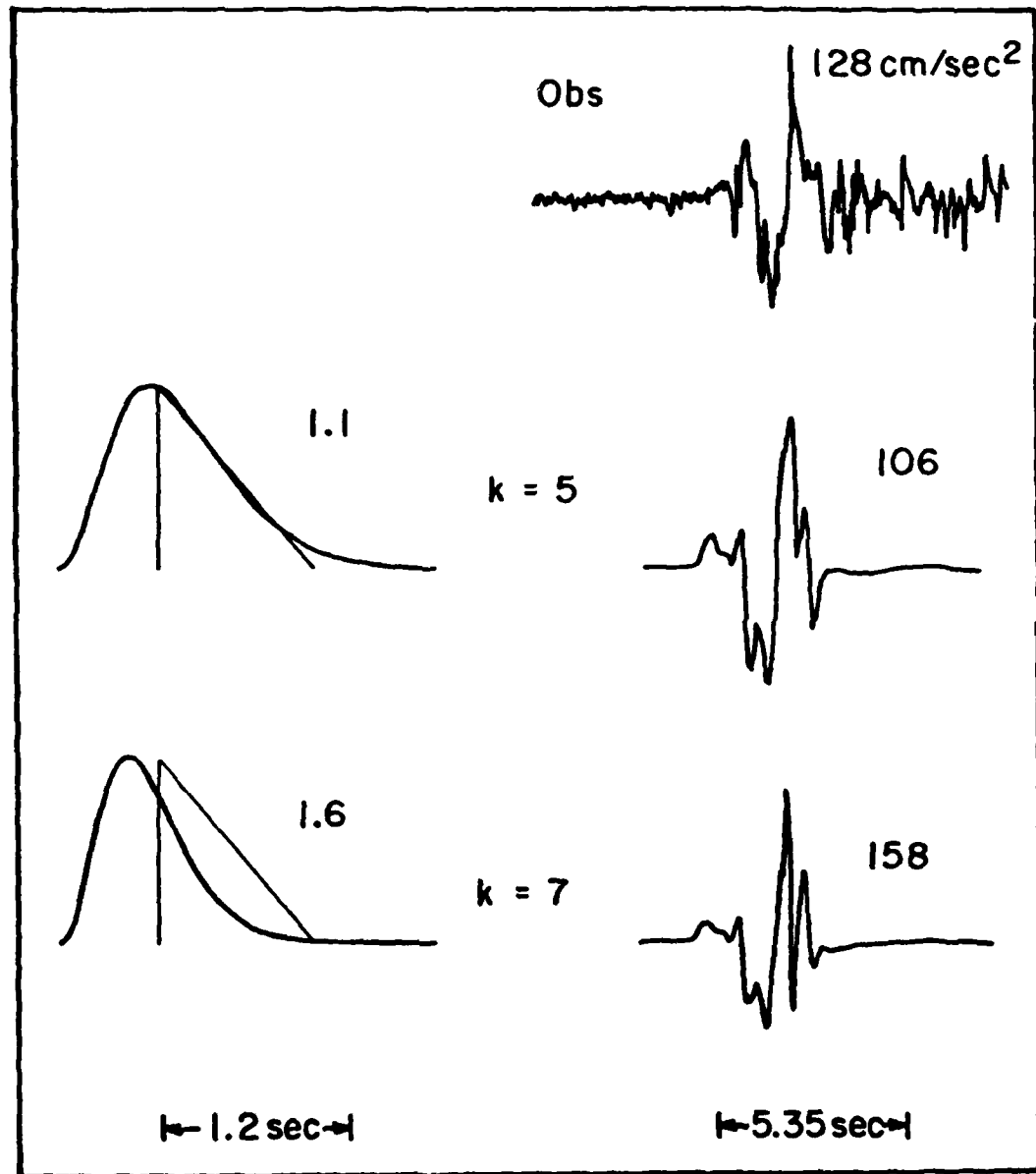


Fig. 16

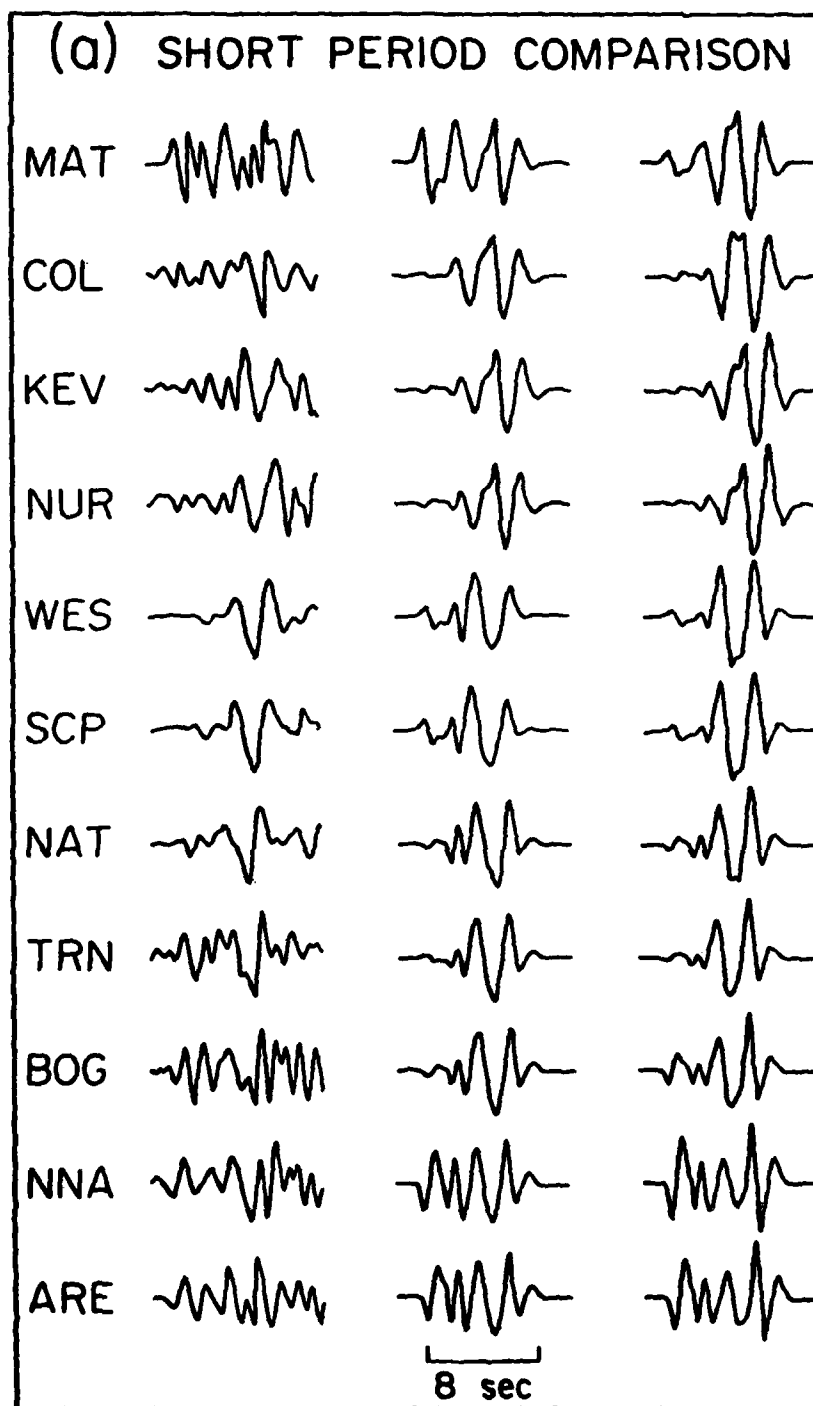


Fig. 17a

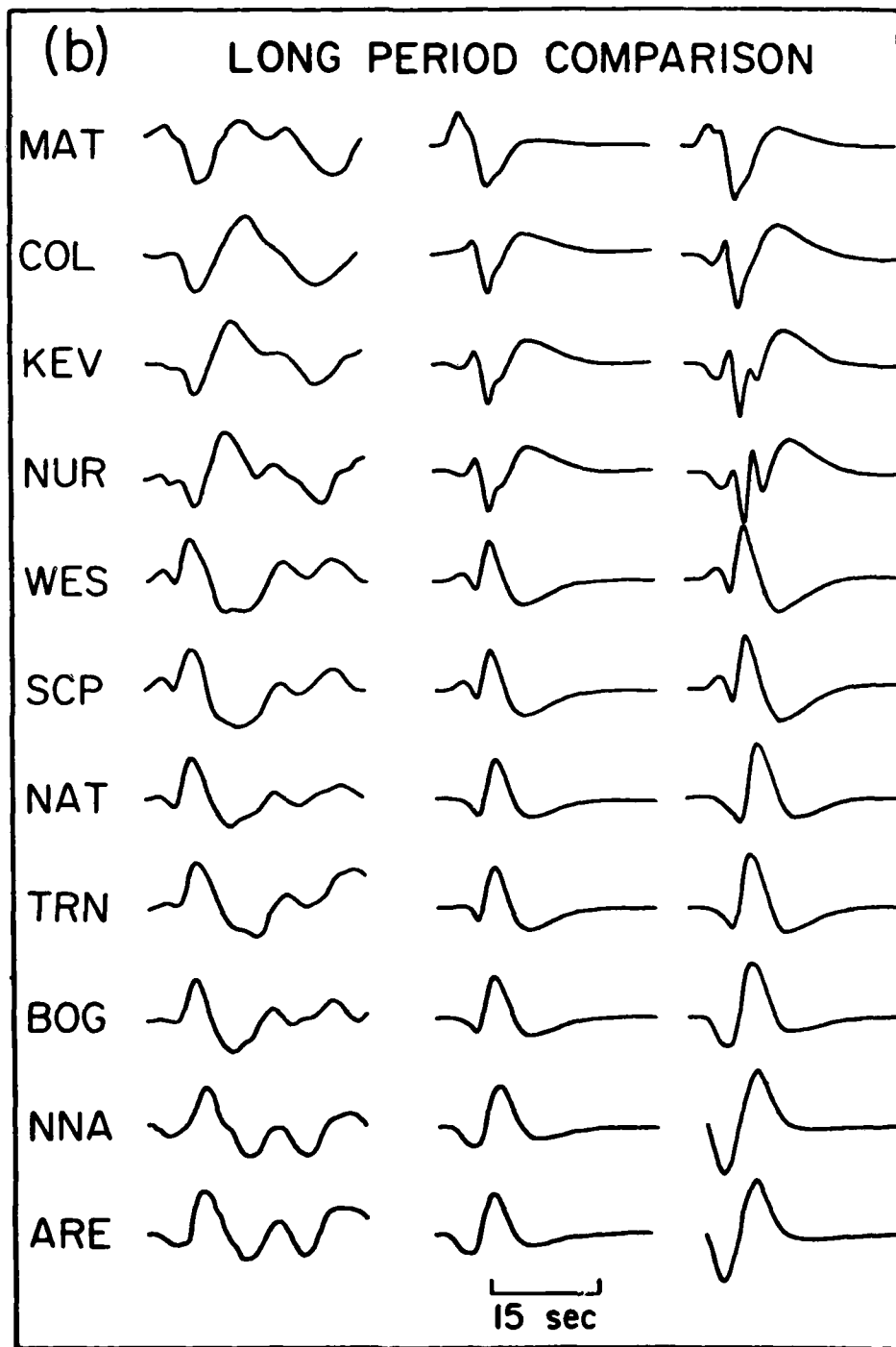


Fig. 17b

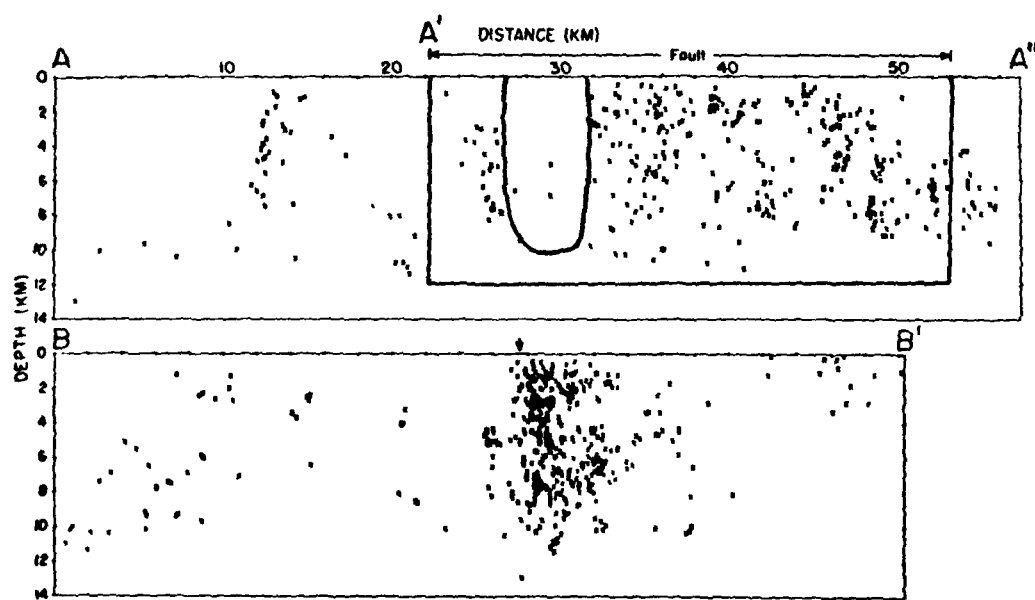


Fig. 18

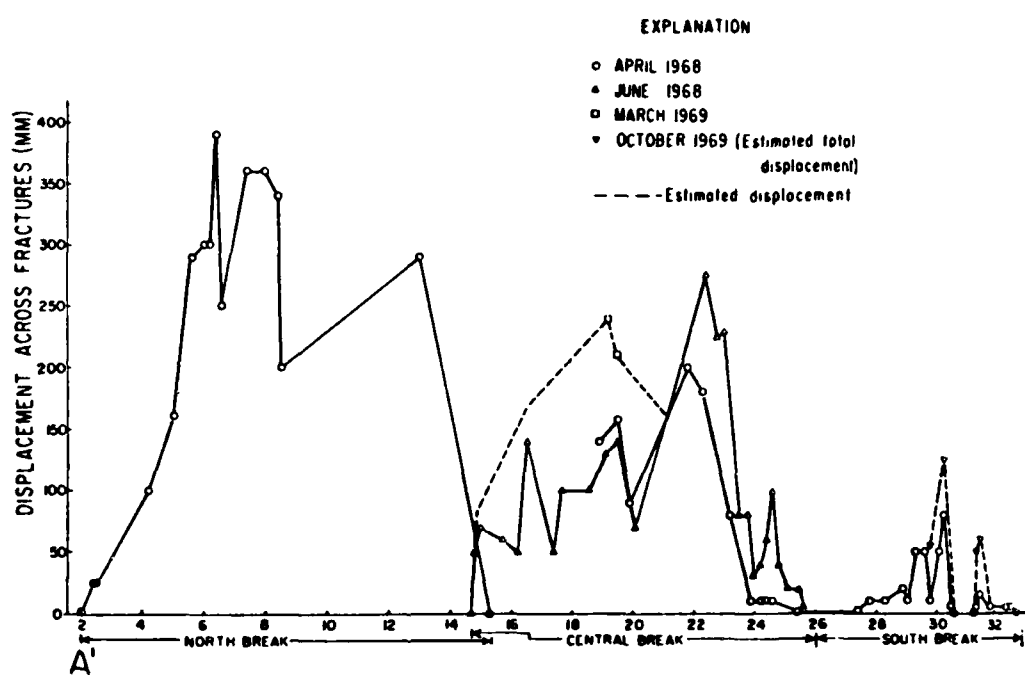


Fig. 19